Mohamed Boudiaf University - M'sila

FACULTY OF TECHNOLOGY

DEPARTMENT OF ELECTRICAL ENGINEERING

Serial number……..…

Registration number……..……

Thesis

Presented for graduation from

LMD DOCTORATE

Major : Electrical Engineering

Specialty : Electrical Controls

THEME

Fault tolerant control based nonlinear approach for motor system

Presented by

ZEGHLACHE Ayyoub

Defended on : 14/02/2024

In front of the jury composed of :

Last Name & First Name	Grade	Establishment	Quality
KHODJA Djalal-eddine	**Professor**	Univ. of **M'sila**	President
MEKKI Hemza	**MCA**	Univ. of **M'sila**	Advisor
DJERIOUI Ali	**MCA**	Univ. of **M'sila**	Co- Advisor
BOUGUERRA Abderrahmen	**Professor**	Univ. of **M'sila**	Examiner
BENHADOUGA Seddik	**Professor**	Univ. of **Bordj Bou Arreridj**	Examiner
SAOUDI Kamel	**Professor**	Univ. of **Bouira**	Examiner

Academic year : 2023/2024

Acknowledgements

Praise be to the Almighty God who has given me faith, courage, and patience to carry out this work.

I want to express my deep gratitude to my supervisor Dr. Hemza Mekki from m'sila university, for the confidence he has placed in me, through his presence always with me, by his direction, his modesty, his advice, and constructive remarks for the good progress of this work.

I thank Dr. Ali Djerioui from m'sila university for having co-supervised me, for his orientation, availability, listening, and patience during the realization of this job.

I would like to thank everyone who helps me to improve my work. and who gave me any remark that helped me to perfect this manuscript.

I express my deep gratitude to my parents, my brother, my sister, and my whole family for their encouragement and prayers that allowed me to achieve this modest job. I am very grateful for the confidence they have placed in me.

Finally, I express my gratitude to all those who have contributed in one way or another to the development of this work.

O Allah, send your blessings on your noble messenger, his family, and companions, and bless us in our life.

Dedication

I dedicate this work to my parents:

May they find here the testimony of my deep gratitude and acknowledgment

To my brother, my sister, and my family who give love and liveliness.

To all those who have helped me - directly or indirectly - and those who shared with me the emotional moments during the accomplishment of this work and who warmly supported and encouraged throughout my journey.

To all my friends who have always encouraged me, and to whom I wish more success.

Thanks!

Ayyoub ZEGHLACHE

Abstract

This thesis focuses on designing a Fault Tolerant Control (FTC) approach for motor systems. Electrical motors, widely used in industrial applications, are prone to faults that compromise efficiency and reliability. The study explores FTC principles and analyzes faults in motors, particularly addressing challenges in Permanent Magnet Synchronous Motors (PMSMs). It proposes a novel FTC strategy, combining sliding mode control (SMC) with nonlinear observers such as fuzzy extended state observer (FESO) and nonlinear extended state observer (NESO). The aim is to ensure robust PMSM operation amidst disturbances and faults, as confirmed by simulation results demonstrating enhanced stability and control performance.

Key words: *Fault-Tolerant Control, Permanent Magnet Synchronous Motors, Sliding Mode Control, Fuzzy Extended State Observer, Nonlinear Extended State Observer.*

ملخص

تركز هذه الرسالة على تصميم نهج للتحكم المتسامح مع الأعطال لأنظمة المحركات. المحركات الكهربائية، المستخدمة على نطاق واسع في التطبيقات الصناعية، عرضة للعديد من الأعطال التي قد تؤثر على كفاءتها وموثوقيتها. تستكشف الدراسة مبادئ التحكم المتسامح مع الأعطال وتحليل الأعطال في المحركات، مع التركيز بشكل خاص على التحديات المتعلقة بالمحركات المتزامنة بالمغناطيس الدائم. تقترح الدراسة استراتيجية جديدة للتحكم المتسامح مع الأعطال، تدمج بين تقنية التحكم بوضع الانزلاق مع مراقبين غير خطيين مثل المراقب الضبابي ذو الحالة الموسعة والمراقب غير الخطي ذو الحالة الموسعة. الهدف هو ضمان تشغيل قوي للمحركات المتزامنة بالمغناطيس الدائم في وجود الاضطرابات والأعطال، كما يتم تأكيد ذلك من خلال نتائج المحاكاة التي تظهر استقرارًا محسّنًا وأداء تحكم محسّنًا.

كلمات مفتاحية: التحكم المتسامح مع الأعطال، المحركات المتزامنة بالمغناطيس الدائم، التحكم بواسطة وضع الانزلاق، المراقب الضبابي ذو الحالة الموسعة، المراقب غير الخطي ذو الحالة الموسعة.

Résumé

Cette thèse se concentre sur la conception d'une approche de Commande Tolérante aux Défauts (FTC) pour les systèmes moteurs. Les moteurs électriques, largement utilisés dans l'industrie, sont sujets à diverses fautes compromettant leur efficacité et fiabilité. L'étude explore les principes du FTC et analyse les fautes dans les moteurs, mettant particulièrement l'accent sur les défis liés aux Moteurs Synchrones à Aimants Permanents (MSAP). Elle propose une nouvelle stratégie de FTC, combinant le contrôle par mode glissant (SMC) avec des observateurs non linéaires tels qu'un observateur flou à état étendu (FESO) et un observateur non linéaire à état étendu (NESO). L'objectif est d'assurer un fonctionnement robuste des MSAP en présence de perturbations et de fautes, comme confirmé par des résultats de simulation démontrant une stabilité accrue et des performances de contrôle améliorées.

Mots clés : *Commande Tolérante aux Défauts, Moteurs Synchrones à Aimants Permanents, Contrôle par Mode Glissant, Observateur Flou à État Étendu, Observateur Non Linéaire à État Étendu.*

Contents

List of Figures

List of Tables

List of Abbreviations

FTC:	Fault-Tolerant Control
PMSM:	Permanent Magnet Synchronous Motor
SPMSM:	Surface Permanent Magnet Synchronous Motor
PMSMs:	Permanent Magnet Synchronous Motors
FOC:	Field-Oriented Control
PI:	Proportional-Integral
SMC:	Sliding Mode Control
TSMC:	Traditional Sliding Mode Control
SOSMC:	Second-Order Sliding Mode Control
IT2FLC:	Interval Type 2 Fuzzy Logic Controller
ESO:	Extended State Observer
FESO:	Fuzzy Extended State Observer
NESO:	Nonlinear Extended State Observer
MTO:	maximizing torque output
MCL:	Minimizing Copper Loss
OCF:	Open-Circuit Fault
OCFs:	Open-Circuit Faults
HTF:	Hyperbolic Tangent Function
THD:	Total Harmonic Distortion
FFT:	Fast Fourier Transform
EMF:	Electromotive Force
MMF:	Magnetomotive Force
VSI:	Voltage Source Inverter
VSIs:	Voltage Source Inverters
PWM:	Pulse Width Modulation
CPWM:	Carrier-based PWM
SVPWM:	Space Vector Pulse Width Modulation

General introduction

Permanent Magnet Synchronous Motors (PMSMs) are widely used in various applications that require high performance, reliability, and fault tolerance [1]. These motors have the advantages of a compact design, reduced weight, and high efficiency compared to other types of electric motors [2, 3, 4]. Multi-phase PMSMs are especially suitable for the transportation and aerospace industries, where these attributes are essential for ensuring safe and reliable operation [1, 5].

However, controlling multi-phase PMSMs is challenging, especially under open-circuit faults (OCFs), which can cause asymmetry and nonlinearity in motor dynamics. These faults typically arise from a disrupted or disconnected wire in the motor windings [6]. These effects can result in undesirable torque ripples, degrading the performance and efficiency of the motor. Therefore, detecting and promptly responding to such faults is paramount for ensuring continued motor performance and implementing a fault-tolerant control (FTC) strategy. One of the most common methods for detecting OCFs is to monitor the motor currents using associated current sensors [7].

Although conventional linear controllers, such as the proportional-integral (PI) controller, are widely used for field-oriented control (FOC) of PMSMs, they may not be able to cope with the complexity and nonlinearity of the motor under faults. Surprisingly, there is a lack of research on nonlinear control methods and compensation techniques for multi-phase PMSMs under OCFs. This lack of investigation motivates the need for further research and development in this crucial area of study. Therefore, the main objective of this thesis is to propose and implement nonlinear controllers for PMSMs under faults, with the aim of reducing torque ripples and improving motor performance.

Chapter 1 of this thesis serves as a foundational exploration into the realm of FTC and the analysis of faults in electrical motors. FTC is a critical discipline within control engineering that seeks to maintain the desired performance and stability of a system even in the presence of faults. Given the widespread use of electrical motors in industrial applications, understanding and addressing faults such as stator winding faults, rotor faults, bearing faults,

and eccentricity faults becomes paramount. The chapter introduces key concepts such as the classification of faults in control systems, Motor Current Signature Analysis (MCSA), and the fault frequency spectrum in AC Induction Motor and AC Synchronous Motor.

Chapter 2 explores the fundamental principles of modeling and FOC of PMSMs. It commences by establishing the general mathematical models for n-phase PMSMs, encompassing both 3-phase and 5-phase PMSM models. Subsequently, it introduces a generalized FOC strategy based on PI controllers applicable to n-phase PMSMs. This strategy incorporates all odd harmonics of electromotive force (EMF) components along with the fundamental harmonic to achieve enhanced torque performance. The chapter then explores two pulse-width modulation (PWM) strategies for n-phase voltage source inverters (VSIs), each offering advantages and limitations. Finally, the chapter concludes by presenting simulation results that demonstrate the effectiveness of FOC with 3rd harmonic current injection for 5-phase PMSMs. These results exemplify the performance improvements and torque enhancement achieved through FOC.

Chapter 3 delves into the specific challenges of the PMSM system using FOC and introduces anti-disturbance sliding-mode control, with a focus on second-order sliding mode control (SOSMC). This chapter explores the advantages of SOSMC in mitigating chattering, a common issue in traditional sliding-mode control (SMC). Through simulation tests and experimental validations on a surface permanent magnet synchronous motor (SPMSM), the chapter demonstrates SOSMC's effectiveness in suppressing disturbances and achieving robust control performance.

Next, chapter 4 addresses the persistent challenges associated with unexpected shutdowns and malfunctions in 3-phase PMSMs, specifically related to demagnetization and short-circuit faults. This chapter proposes a novel FTC strategy that combines SOSMC with a fuzzy extended state observer (FESO) featuring an interval type 2 fuzzy logic controller (IT2FLC) [8]. The objective is to ensure the robust operation of PMSMs in the face of demagnetization faults and short-circuit faults. The chapter provides a comprehensive exploration of the proposed FTC strategy, including the 3-phase PMSM model under the influence of faults and simulation results.

In Chapter 5, the focus shifts to the fault-tolerant control of 5-phase PMSMs. Despite their inherent robustness, 5-phase PMSMs are susceptible to OCFs that can impact their performance. This chapter explores the application of SMC with a nonlinear extended state observer (NESO) to handle the complexity and nonlinearity of 5-phase PMSMs during OCFs. The combination of NESO and SMC is proposed as an effective strategy to address external

disturbances and enhance fault tolerance. The chapter concludes with an analysis of the results and implications of this work.

Collectively, these chapters contribute to the overarching goal of enhancing the fault tolerance and control performance of electric motors, particularly PMSMs, in various applications. The proposed strategies and methodologies aim to ensure the robust and reliable operation of motor systems in the presence of faults, ultimately advancing the field of control engineering and electrical motor applications.

Chapter 1

Introduction of FTC and Electrical Motor Fault Analysis

1.1 Introduction

Fault Tolerant Control (FTC) is a branch of control engineering that aims to maintain the desired performance and stability of a system in the presence of faults. Faults are abnormal events that affect the system's components or parameters and cause deviations from the normal operation. Electrical motors are widely used in various industrial applications and are prone to different types of faults, such as stator winding faults, rotor faults, bearing faults, and eccentricity faults. These faults can degrade the motor's efficiency, reliability, and lifespan, and may even lead to catastrophic failures. Therefore, it is important to detect and diagnose these faults as early as possible and to apply appropriate control strategies to mitigate their effects. This chapter provides an overview of the concepts and principles related to FTC and the analysis of electrical motor faults. It covers the following topics:

- Definition and classification of faults in control systems
- Motor Current Signature Analysis as a method for identifying faults in electrical motors
- Fault frequency spectrum in AC Induction Motor and AC Synchronous Motor

The chapter serves as an introduction to the fundamental concepts and techniques used in FTC and the analysis of electrical motor faults. It provides a foundation for further exploration and understanding of these topics in the subsequent chapters.

1.2 What is a Fault?

A fault in a control system is a deviation from the nominal situation of its structure or parameters. It can vary from performance degradation to total failure. It's different from system uncertainties and external disturbances, which can be filtered out or handled with a robust design. Unlike faults, require remedial actions to be taken.

1.2.1 Fault Types

Within the context of system dynamics, a fault is characterized as any deviation or malfunction within a system that leads to fluctuations in its behavior. These deviations can manifest in three distinct types: system fault, actuator fault, or sensor fault.

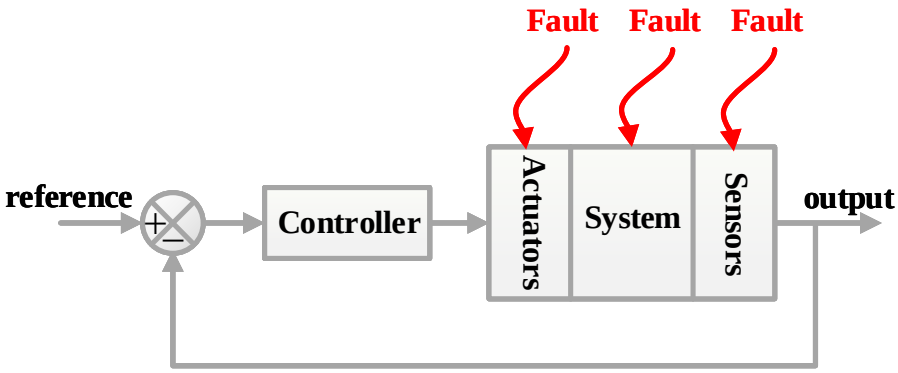

Figure 1.1: Types of faults in the control system.

1.2.1.1 System fault

This type of fault originates from the plant itself. Oftentimes, faults that do not belong to the actuator or sensor fault categories are arbitrarily classified in this category. However, a system fault results from the breakage or alteration of a component of the system, reducing the ability of the system to perform a task. In practice, this means considering a modification of the characteristics of the system itself (such as faults within an electric motor itself, like rust on bearings, damaged stator windings, or broken rotor bars).

1.2.1.2 Actuator fault

This type of fault acts at the operational level and degrades the input signal of the system. It represents a total failure or partial fault of an actuator that acts on the system. An example of a total failure of an actuator is when it becomes "stuck" in a position, making it impossible to control the system through that actuator. Partial actuator faults are those where actuators react similarly to the nominal operating mode but with some degradation in their action on the system, such as loss of power in a motor or leakage in a cylinder.

1.2.1.3 Sensor fault

Sensor fault degrades the accuracy of a system's representation of its physical state. In the case of partial sensor fault, the signal deviates somewhat from the actual value of the measured variable. This deviation may manifest as a reduction in the displayed value or the introduction of bias or noise, hindering precise readings. Conversely, total sensor fault results in values that bear no connection to the measured quantity.

1.2.2 Classification of Faults Based on Severity

Faults can be classified into three main categories based on their severity:

1.2.2.1 Permanent faults:

These types of faults are characterized by sudden changes in physical parameters or system structures that happen more quickly than the nominal dynamic process. Detecting such abrupt changes is usually a challenge for most fault detection algorithms, as they are difficult to track based on residuals. According to Reference [9], severe vibrations, metal flakes separating, and short circuits are the three types of permanent faults that can occur.

1.2.2.2 Drift-like faults:

These kinds of faults can go unnoticed by detection systems due to their small effects on residuals. They are caused by sensor/actuator inaccuracy or partial failure and often take a long time to manifest as slowly evolving faults.

1.2.2.3 Intermittent faults:

This category of fault is characterized by malfunctions that occur at irregular intervals and can be caused by various factors such as improper electrical connections to sensors and

actuators. As the complexity of the system increases, the likelihood of intermittent faults occurring also increases. Most detection algorithms find it challenging to detect intermittent faults due to their inconsistent nature. Figure 1.2 gives an overview of the different types of faults.

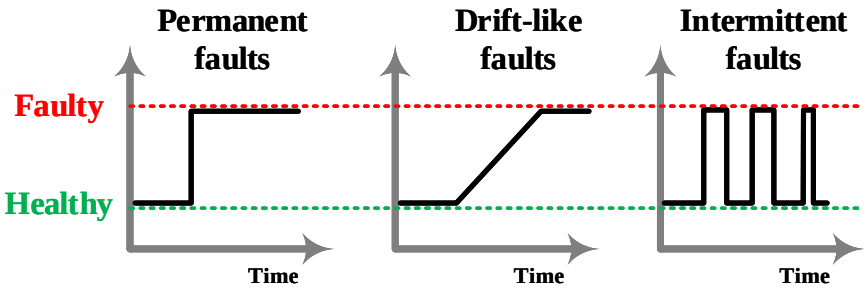

Figure 1.2: Classification of faults based on severity.

1.3 What is FTC?

Fault-tolerant control is a term used to describe a control system that is capable of recovering its original functionality during a fault event while maintaining the same or an acceptable level of performance. Such a control system can automatically compensate for faults and failures in the system components, ensuring system stability and desired overall performance. The concept of Fault-tolerant control (FTC) system has been widely discussed by researchers over the last two decades, leading to significant scientific progress in this field [10, 11, 12, 13, 14, 15, 16, 17, 18, 19, 20, 21, 22].

1.3.1 Classification of FTC systems

FTC systems can be classified into two main types: active and passive [13, 23, 24]. The main difference between them is that active FTC systems use an FDI system to detect and identify the faults and then use a supervisory system to adjust the control structure and parameters to mitigate the fault effects [25]. On the other hand, passive FTC systems do not rely on fault information but rather use a robust controller that can handle a predefined range of faults in the system [26, 27]. Figure 1.3 shows the basic classification of FTC techniques.

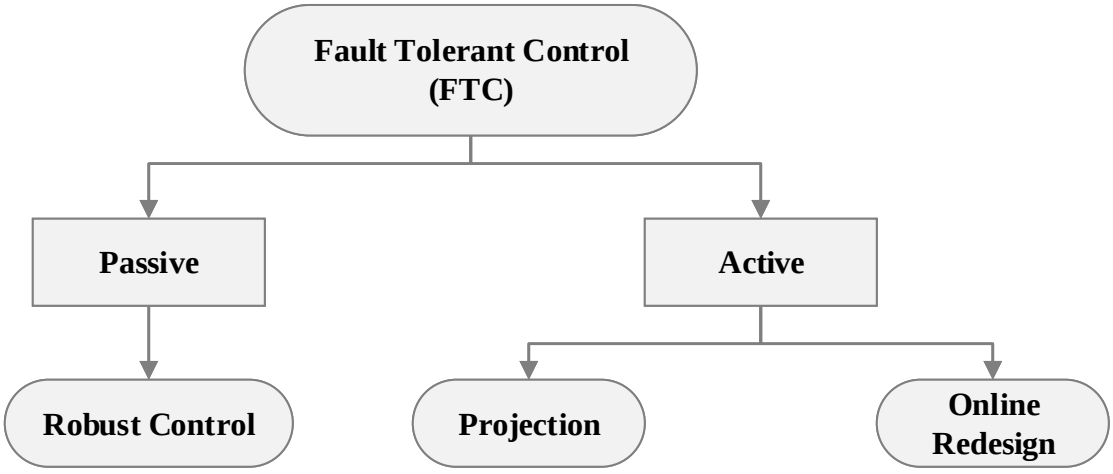

Figure 1.3: Classification of FTC systems.

1.3.1.1 Passive FTC

Passive FTC systems are designed to incorporate redundancy directly into their control design and function without relying on fault information [28, 29]. A variety of approaches have been employed, ranging from sliding mode control (SMC) [30, 31, 32] to H_∞ [33, 34, 35], Lyapunov-based control [36], fuzzy logic control [37, 38], control allocation [39, 40, 41] and Linear Quadratic control [41]. These techniques are preferred for their simplicity in design and application, minimal delay between fault occurrence and low computational load, and accommodation [27, 28, 42].

In a passive FTC system, the controller remains unchanged even in the event of a fault. Both the structure and parameters of the controller are configured to enable the system to withstand a range of faults without requiring active adjustments [23]*. This method relies on robust control techniques, ensuring that the closed-loop system remains insensitive to specific faults by employing constant parameters for the controller, as depicted in Figure 1.4. A predefined list of potential malfunctions, including fundamental design faults and all failure modes, along with system operating conditions considered normal at the design stage, is assumed to be known beforehand [15]. When a failure occurs, the controller must maintain system stability with an acceptable level of performance degradation. Notably, this approach requires neither fault detection schemes nor control law reconfiguration, making it computationally efficient and appealing. While these techniques are generally straightforward to implement, their practical application remains somewhat limited.

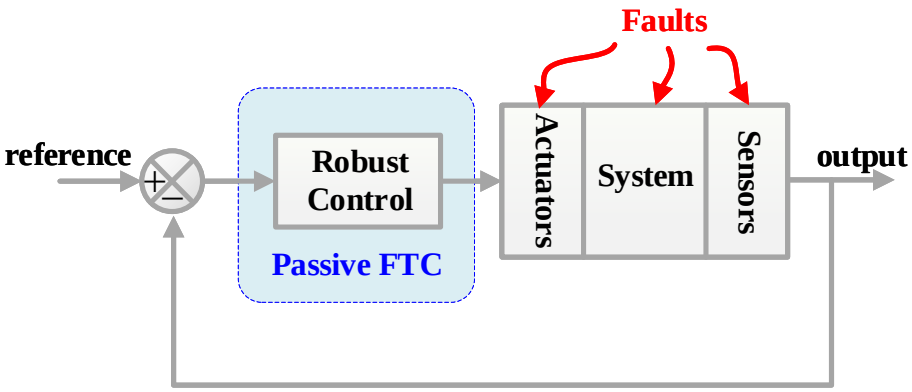

Figure 1.4: Schematic diagram for passive FTC systems.

Passive FTC methods have certain limitations that need to be considered. These limitations include:

- Assumption of System Stability: Passive FTC methods rely on the assumption that the system will maintain its asymptotic stability in the closed loop, even under certain fault or failure scenarios. However, this assumption may not be sufficient to prevent system breakdowns when faced with unexpected or multiple faults.

- Dependence on Hardware Redundancy: While redundant hardware can enhance a system's reliability, it can also increase the product's cost, weight, and size. It is not feasible to apply redundancy to the entire system due to space and weight constraints. Redundancy is crucial for key components, but not for the entire system.

- Conservative Approach: Passive FTC design requires a concurrent consideration of both normal and fault conditions. This leads to a more conservative approach compared to active FTC design. Passive FTC systems prioritize system robustness across all scenarios at the cost of optimal performance in individual situations. This means that even under normal conditions, the controller's settling time is extended to ensure the system's stability in the presence of a fault.

In the subsequent chapters, our focus will shift towards the exploration of active FTC strategies. For further insights into passive FTC, readers are encouraged to refer to the references [10, 18, 36].

1.3.1.2 Active FTC

Active FTC techniques are generally preferred over passive methods owing to their superior performance and capability to effectively manage a wide range of faults while responding in a unique manner to each one. Active FTC approaches function by reconfiguring the control law to ensure system stability and performance during faults. A design for an active FTC usually consists of three main stages: Detection, Supervision, and Control, which necessitate a Fault Detection and Diagnosis (FDD) technique and a control law reconfiguration approach to handle unanticipated faults. A typical active FTC system comprises a FDD block, a reconfiguration mechanism, and a reconfigurable controller, as illustrated in Figure 1.5.

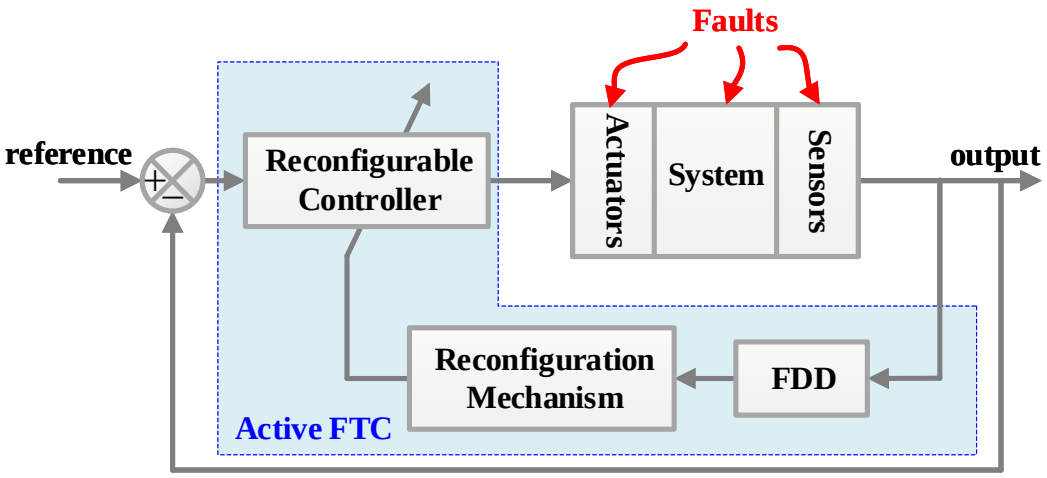

Figure 1.5: Schematic diagram for active FTC systems.

In fact, the FDD block is an important component of an active FTC system, as it provides critical fault information necessary for activating the reconfiguration mechanism as quickly as possible. There are two main types of active strategies: projection-based approach and online redesign approach [43].

- The projection-based approach to FTC involves pre-designing controllers to account for all possible faults or failures that may occur within a system. The projected controller will only become active when a specific fault occurs, for which it is specifically designed. Once a fault is identified, an appropriate control law is selected from a set of pre-estimated and predefined options [44, 45]. The projection method then identifies and transitions to the control law that is most suitable for the existing fault condition. The

FTC-based projection method requires a switching mechanism to transition between the two control strategies. Figure 1.6 illustrates these FTC-based projection techniques.

- The online redesign approach presents a highly promising solution for enhancing fault-tolerant systems. It does not require switching between different controllers when a fault occurs, instead generating a new controller online that can meet control objectives [46]. This method uses the behavioral theory perspective of trajectories, unlike the projection-based approach that relies on two nested controllers. Therefore, the online redesign based approach can compute a new controller based only on the real-time trajectories of the system without needing any prior information about the plant model.

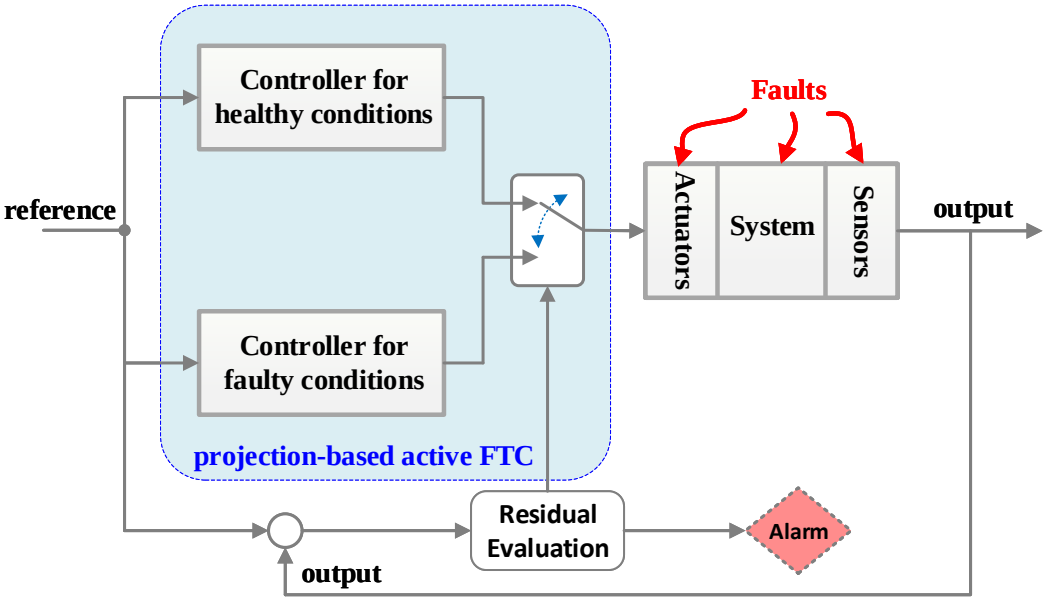

Figure 1.6: Schematic diagram for projection-based active FTC systems.

1.4 Types of Electrical Motors

The stator is an important part of an electric motor that generates a rotating magnetic field by passing current through coils or windings. The design of the stator determines the number and orientation of the poles of the magnetic field. For example, a two-pole three-phase motor has a north-south (N-S) configuration. When a rotor (a magnet) is placed inside the stator, it experiences torque that makes it spin. Notably, the rotational speed of the rotor aligns

with the frequency of the stator's supplied current, classifying this motor as a permanent magnet synchronous motor. Various types of electrical motors fall into categories such as:

- AC induction motor
- AC synchronous motor
- DC motor

It is essential to highlight that AC motors, whether synchronous or induction, share the same stator and can be powered by single-phase, 3-phase, or multi-phase current.

1.5 Faults in Electrical Motor

Electric motors play a pivotal role in industrial applications, accounting for approximately 65% of the electricity consumed in this sector [47]. Given their significance, understanding the primary causes of motor failure is crucial for maintaining operational efficiency. Research based on a survey conducted by the IEEE-Industry Applications Society [48] identified common fault mechanisms in high voltage motors, as illustrated in Figure 1.7.

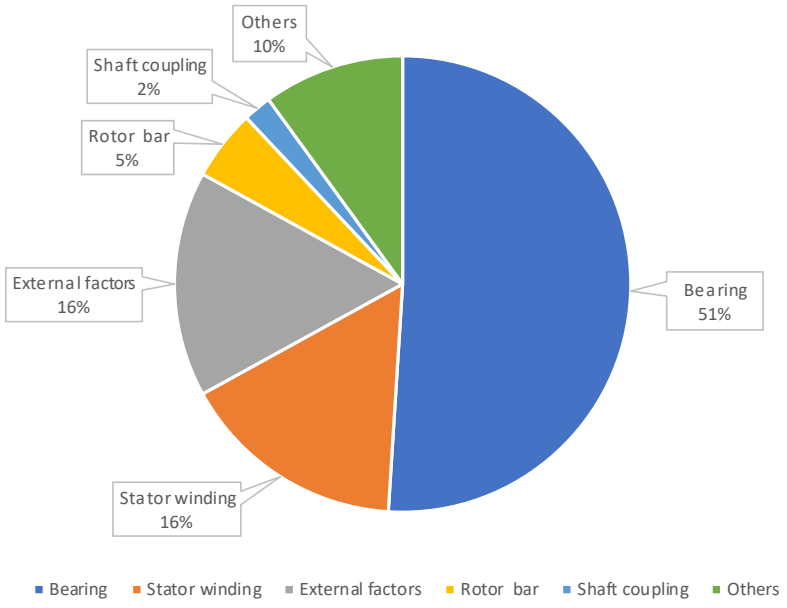

Figure 1.7: Distribution of Failed Components.

One of the leading causes of motor failure, accounting for 51%, is attributed to bearing issues [48]. These failures arise from various factors, including insufficient lubrication,

excessive greasing, misalignment, shaft overload, vibration, and overheating. Insufficient lubrication can lead to bearing seizure, while excessive greasing may cause damage to seals and accumulation of dirt, resulting in overheating and premature failure. Misalignment, often due to incorrect installation or machine wear, can lead to a range of issues, from bearing failure to damage in housing and rotors. Overloading, both in terms of shaft and thermal stress, can also lead to bearing failure, as can extreme vibrations caused by factors like electromagnetic interference, mechanical imbalance, rubbing parts, and resonance. As illustrated in Figure 1.8, a bearing in an electric motor subjected to excessively high vibration levels exhibits a rusty discoloration, indicative of fretting [49].

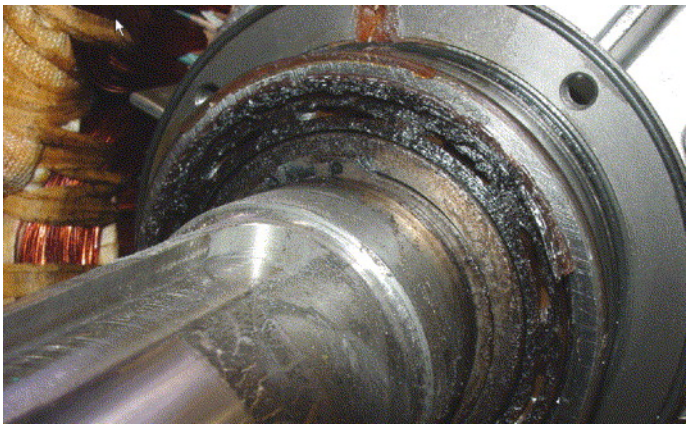

Figure 1.8: Excessive vibration causes rust on electric motor bearings.

Stator winding issues account for 16% of motor failures [48]. Overheating and overloading are the primary culprits, with overstarting being a major contributor to overheating. This process, where the motor draws several times its rated current during startup, places significant thermal stress on the windings, potentially leading to failure. Overloading can also result in extreme heat buildup in the stator windings, further exacerbating the risk of failure. Figure 1.9 illustrates the specific damages incurred by stator windings as a consequence of overload [50].

External conditions contribute to 16% of motor failures, with factors such as motor operating temperature, humidity, contamination, and ambient temperatures playing significant roles. Broken fans, clogged vents, and blocked cooling fins can all contribute to excessive heat buildup, while harsh environmental conditions, high humidity, and contamination can lead to moisture ingress and damage. Ambient temperatures, too, affect motor performance, often necessitating derating for high temperatures and specialized materials for low temperatures.

Rotor bar issues, accounting for 5% of motor failures, primarily result from excessive starting frequency, overloading, and under voltage. High starting frequencies can lead to

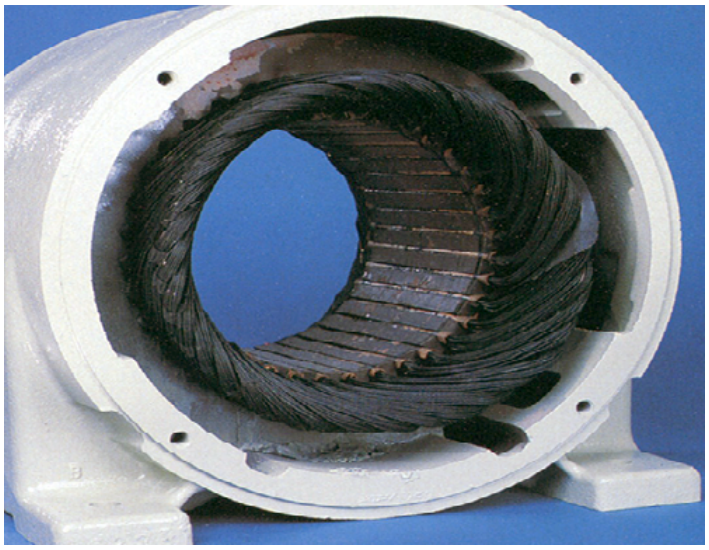

Figure 1.9: Stator winding damaged due to overload.

rotor bar breakage due to the accompanying excessive current, causing temperature rise in the motor. Overloading can result in various mechanical faults, from seized bearings to foreign objects causing disruptions. Under voltage, particularly when coupled with a constant load, can lead to increased running currents, overheating, reduced efficiency, and eventual failure. A visual representation of rotor bar faults is provided in Figure 1.10, where the bar was interrupted by drilling holes into the rotor near the end rings [51].

Figure 1.10: Broken Rotor Bar.

Shaft coupling failures, though less common at 2%, can still significantly impact motor performance. Misalignment and improper installation are the primary causes, necessitating early detection and corrective action.

Finally, air-gap eccentricity between the stator and rotor can lead to unbalanced forces, potentially damaging the motor (see Figure 1.11). Two types of eccentricities, static and

dynamic, have distinct causes ranging from core ovality and misalignment to bearing wear and mechanical resonance. Addressing these various fault mechanisms is critical to enhancing motor reliability and longevity in industrial applications.

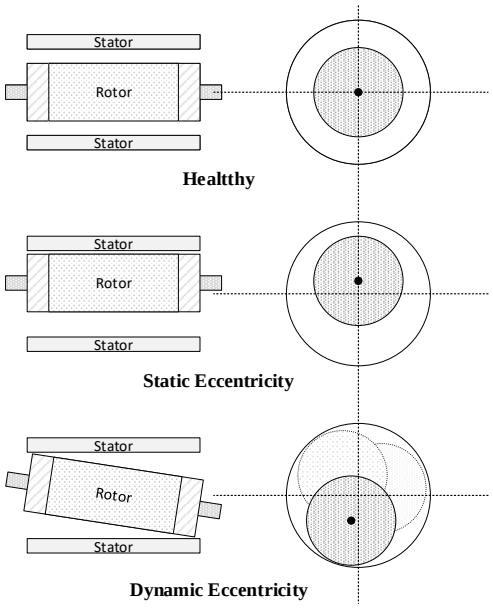

Figure 1.11: Different types of rotor eccentricities.

1.6 MCSA to Detect the Electrical Motor Faults

In most systems and machines, the driving unit is an electrical motor. Therefore, it is crucial to identify any faults in the motor beforehand to avoid unnecessary downtime. Motor current signature analysis (MCSA) is a reliable method to detect faults in the electrical motor, such as broken rotor bars, short-circuits, rotor eccentricity, and bearing faults.

1.6.1 AC Induction Motor Fault Frequency Spectrum

1.6.1.1 Broken Rotor Bar Frequency:

Rotor bar fault will give rise to unbalanced torque, lead to modulation in the current waveform, and produce sidebands in the current spectrum. Current signature analysis is used to detect particular components of the current spectrum directly related to rotor asymmetries.

The frequencies of the spectral components due to broken bar are given by [52]:

$$F_{brb} = F_s \left[k \left(\frac{1-s}{n_p} \right) \pm s \right] \tag{1.1}$$

where F_{brb} and F_s represent the broken rotor bar and supply frequency, respectively; k is a positive integer representing the harmonic index; s is slip; n_p is pole pair of the motor.

1.6.1.2 Short-circuits Frequency:

Isolation failures are typically identified by short circuits in stator coils, and the frequency components of the fault sideband for short circuits can be determined as [53]:

$$F_{st} = F_s \left[\frac{k}{n_p}(1-s) \pm v \right] \tag{1.2}$$

where F_{st} is short-circuit frequency; F_s is supply frequency; k is a positive integer; v is an odd positive integer; s is slip; n_p is pole pair of the motor.

1.6.1.3 Rotor Eccentricity Frequency:

The fault sideband components for rotor eccentricity frequencies can be determined as [54]:

$$F_e = F_s \left[(kR \pm n_d) \frac{(1-s)}{n_p} \pm v \right] \tag{1.3}$$

where F_e is dominant frequency in the current spectrum due to eccentricity; F_s is supply frequency; k is a positive integer; v is an odd positive integer; R is number of rotors; n_d is dynamic eccentricity value ($n_d = 0$ for statically eccentric rotor); s is slip; n_p is pole pair of the motor.

1.6.1.4 Bearing Fault Frequency:

The characteristic fault frequencies for ball bearings are based on ball diameter, pitch diameter, and ball contact angle shown in Figure 1.12. The bearing fault frequency can be written as [55, 56]:

$$F_{bf} = F_s \pm nF_m \tag{1.4}$$

where F_{bf} is bearing fault frequencies in the current spectrum; F_s is supply frequency; n is integer; F_m is bearing frequencies (inner race defect, outer race defect and ball spin). As stated by [56], the bearing frequencies vary according to the type of defect are presented as follows:

- The ball defect frequency: $f_b = \frac{PD}{BD} f_{rm} \left[1 - \left(\frac{BD}{PD} \cos\beta\right)^2\right]$
- The outer race frequency: $f_o = \frac{n}{2} f_{rm} \left[1 - \frac{BD}{PD} \cos\beta\right]$
- The inner race frequency: $f_i = \frac{n}{2} f_{rm} \left[1 + \frac{BD}{PD} \cos\beta\right]$

where f_{rm} is the mechanical rotor frequency; n is the number of bearing balls; β is the contact angle of the balls on the races; PD is the bearing pitch diameter; BD is the ball diameter.

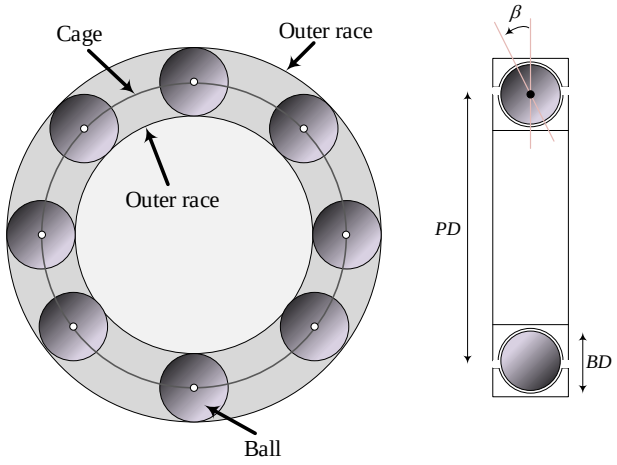

Figure 1.12: Ball bearing dimensions.

1.6.2 AC Synchronous Motor Fault Frequency Spectrum

The majority of electrical and magnetic faults in AC synchronous motors exhibit the same specific harmonics in motor current signature analysis. The fault frequencies for different fault types can be expressed as follows [57]:

$$F_{fault} = \left[1 \pm \frac{k}{n_p}\right] F_s \tag{1.5}$$

where k is an integer constant number; F_s is supply frequency; n_p is pole pair of the motor. As indicated in (1.5), unlike AC induction motors, the fault frequency spectrum remains independent of slip.

1.6.3 Current Measurement and Signal Analysis

Accurately performing motor current signature analysis (MCSA) requires the measurement of the current waveform. Using an ammeter for this purpose is inadequate, as it only provides

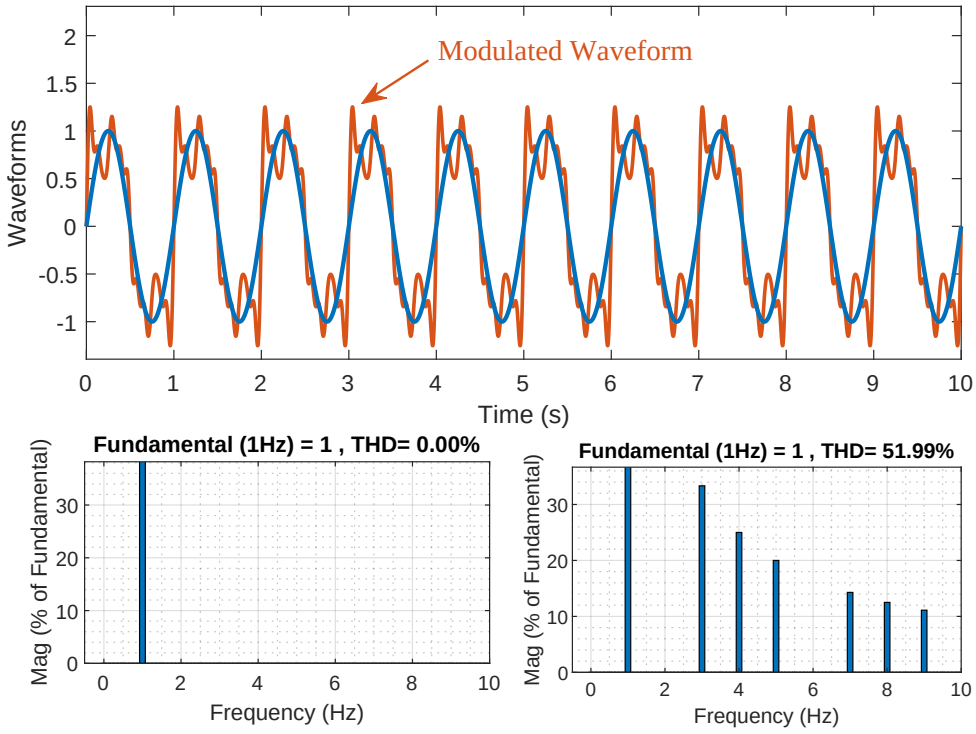

Figure 1.13: Comparison of sine wave and modulated waveform.

the root mean square (RMS) value, which is insufficient for MCSA. MCSA relies on the detailed current waveform, which cannot be accurately captured using an ammeter. Figure 1.13 shows that two waveforms can possess similar statistical parameters yet exhibit different frequency spectrum content. This difference in frequency content may indicate the presence of faults in the motor if the modulated waveform represents the motor's current. The current measurement can be:

- Current Transformer.
- Rogowski Coil.
- Hall Effect Sensor.

After measuring the current waveform, it is analyzed to identify the specific frequency spectrum that indicates the presence of faults in the motors. The signal analysis can be performed using either of the following methods:

- Data Acquisition Unit and a PC.
- Stand alone FFT analyzer.

1.6.4 Theory of MCSA

In this theory of MCSA section, we will explore the rationale behind concentrating on the analysis of the current waveform for the purpose of identifying faults in motors. For instance, when examining a three-phase motor and taking into account the three oscillating torques resulting from torsional vibration, each characterized by a distinct frequency, the torque equation can be expressed as follows:

$$T = T_0 + T_1 \cos\left(2\pi F_1 t + \phi_1\right) + T_2 \cos\left(2\pi F_2 t + \phi_2\right) + T_3 \cos\left(2\pi F_3 t + \phi_3\right) \tag{1.6}$$

where T_0 is the average torque, representative of the healthy motor. T_1, T_2, and T_3 are the oscillating torques due to torsional vibrations that indicate the faults. F_1, F_2, and F_3 are the frequencies produced by the faults.

The stator current is included in two components, the direct component (I_{sd}) for generating magnet field and the quadrature component (I_{sq}) for producing torque. Due to faults, these components will have oscillating components as shown by the following equations:

$$I_{sd} = I_{sd_0} + A_{d_1} \sin\left(2\pi F_1 t + \phi_{d_1}\right) + A_{d_2} \sin\left(2\pi F_2 t + \phi_{d_2}\right) + A_{d_3} \sin\left(2\pi F_3 t + \phi_{d_3}\right) \tag{1.7}$$

$$I_{sq} = I_{sq_0} + A_{q_1} \cos\left(2\pi F_1 t + \phi_{q_1}\right) + A_{q_2} \cos\left(2\pi F_2 t + \phi_{q_2}\right) + A_{q_3} \cos\left(2\pi F_3 t + \phi_{q_3}\right) \tag{1.8}$$

By using inverse park transformation, the current in a-phase will be:

$$I_{sa} = I_{sd} \sin\left(2\pi F_s t\right) + I_{sq} \cos\left(2\pi F_s t\right) \tag{1.9}$$

Assuming $\phi_{d_1} \approx \phi_{q_1}$; $\phi_{d_2} \approx \phi_{q_2}$ and $\phi_{d_3} \approx \phi_{q_3}$ the above equation yields to:

$$\begin{aligned} I_{sa} = {} & I_0 \sin\left(2\pi F_s t + \phi_0\right) \\ & + \left(\frac{A_{q_1} + A_{d_1}}{2}\right) \cos\left(2\pi \left(F_s - F_1\right) t - \phi_{d_1}\right) + \left(\frac{A_{q_1} - A_{d_1}}{2}\right) \cos\left(2\pi \left(F_s + F_1\right) t + \phi_{d_1}\right) \\ & + \left(\frac{A_{q_2} + A_{d_2}}{2}\right) \cos\left(2\pi \left(F_s - F_2\right) t - \phi_{d_2}\right) + \left(\frac{A_{q_2} - A_{d_2}}{2}\right) \cos\left(2\pi \left(F_s + F_2\right) t + \phi_{d_2}\right) \\ & + \left(\frac{A_{q_3} + A_{d_3}}{2}\right) \cos\left(2\pi \left(F_s - F_3\right) t - \phi_{d_3}\right) + \left(\frac{A_{q_3} - A_{d_3}}{2}\right) \cos\left(2\pi \left(F_s + F_3\right) t + \phi_{d_3}\right) \end{aligned}$$

where $I_0 = \sqrt{I_{sq_0}^2 + I_{sd_0}^2}$ and $\phi_0 = \tan^{-1}\left(I_{sq_0}/I_{sd_0}\right)$; Sidebands of components of torsional vibration (F_1, F_2 and F_3) across supply line frequency (F_s) . I_0 is the amplitude of the supply frequency; $\left(A_{q_{123}} + A_{d_{123}}\right)/2$ and $\left(A_{q_{123}} - A_{d_{123}}\right)/2$ are amplitudes of the lower and higher sidebands due to the fault, respectively.

The a-phase current for multi sidebands components is obtained as:

$$\begin{aligned} I_{sa} &= I_0 \sin\left(2\pi F_s t + \phi_0\right) \\ &+ \sum_{i=1}^{n} \left(\frac{A_{q_i} + A_{d_i}}{2}\right) \cos\left(2\pi \left(F_s - F_i\right) t - \phi_i\right) \\ &+ \sum_{i=1}^{n} \left(\frac{A_{q_i} - A_{d_i}}{2}\right) \cos\left(2\pi \left(F_s + F_i\right) t + \phi_i\right) \end{aligned} \tag{1.10}$$

where n represents the number of harmonics produced by the faults.

1.7 Conclusion

This chapter has presented the basic concepts and methods of Fault-Tolerant Control (FTC) for electrical motor fault analysis. It has shown how current waveform analysis can be used to detect and diagnose faults in AC motors and how FTC can be classified into passive and active approaches. Passive FTC does not require any fault detection or control reconfiguration, while active FTC involves adjusting the control law to maintain system stability and performance under faults. The chapter has also introduced the fault frequency spectrum for different types of faults in AC motors. The next chapters will focus on the design and implementation of control to deal with disturbances and faults effectively.

Chapter 2

Modelling and FOC of PMSM System

2.1 Introduction

The PMSM system has garnered significant research attention due to the twofold advantages of its rotor design and multiphase stator windings [58]. The rotors in PMSM system are naturally designed with permanent magnets, offering several benefits, such as the absence of losses caused by eddy currents in the magnetic structure. Additionally, as more phases are added to the stator winding, more current can be injected by harmonics, providing more degrees of freedom to enhance electromagnetic torque density [58].

The goal of implementing a field-oriented control (FOC) strategy in the motor system is to concurrently minimize production costs and improve performance [59]. The fundamental concept behind FOC design is to achieve torque control for AC motors comparable to that of DC motors [60]. Several methods based on FOC are currently employed to optimize electromagnetic torque, ensuring motor performance is sustained even under overloading conditions through harmonic injection into the current references [61, 62, 63, 64, 65].

This chapter delves into the modeling and field-oriented control of the PMSM system. It begins by introducing the general mathematical models of n-phase PMSMs, including both 3-phase and 5-phase PMSM models. Next, it presents a general FOC strategy based on PI controllers applicable to n-phase PMSMs. This strategy considers all odd harmonics of EMF components along with the fundamental harmonic to achieve high torque.

The chapter then explores various Pulse Width Modulation (PWM) strategies for n-phase Voltage Source Inverters (VSIs), which are essential for generating the required voltage waveforms to drive the n-phase PMSM. Carrier-based PWM (CPWM) and Space Vector PWM (SVPWM) are two primary PWM techniques, each with its own advantages and disadvan-

tages. The chapter discusses the implementation and characteristics of both methods.

Finally, the chapter concludes with a presentation of simulation results that demonstrate the effectiveness of the FOC with 3rd harmonic current injection for 5-phase PMSMs. These results showcase the improved performance and torque enhancement achieved through FOC and appropriate PWM techniques.

2.2 Model of the *n*-phase PMSM

The design of the n-phase PMSM is based on symmetry, ensuring an equal spatial displacement of $\alpha = 2\pi/n$ between each phase. The general n-phase PMSM model is simplified by focusing on the star-connected multiphase motor without a neutral conductor for odd phase numbers, eliminating the need to consider the homopolar current. Other factors, such as core losses, cogging, magnetic saturation, and the effect of temperature on the permanent magnet flux density, are also neglected for simplicity in the model.

The electrical voltage equation for the n-phase PMSM, where n represents the number of phases supplying power to the motor, can be expressed in the original frame as follows:

$$v_{s,n} = R_{s,n} i_{s,n} + \frac{d}{dt}(L_{s,n} i_{s,n} + \phi_{fm,n}) \tag{2.1}$$

where $v_{s,n}$ is the $n \times 1$ vector of the stator voltage, $i_{s,n}$ is the $n \times 1$ vector of the stator current. $R_{s,n}$ represents the $n \times n$ matrix characterizing stator resistance, structured as a diagonal matrix with each element denoting the resistance of its corresponding phase and the remaining elements set to zero. $L_{s,n}$ is the $n \times n$ matrix signifying stator inductance, structured with a diagonal where each element represents the self-inductance of its respective phase, and off-diagonal elements denoting mutual inductance between phases. $\phi_{fm,n}$ is the $n \times 1$ vector of the flux-linkage produced by the permanent magnet and can be represented in the original frame as follows:

$$\boldsymbol{\phi}_{fm,n} = \begin{bmatrix} \phi_{fm1} \\ \vdots \\ \phi_{fmn} \end{bmatrix} = \sum_{h=1,3,5,\ldots} \phi_{fh} \begin{bmatrix} \cos\left(h(\theta - \frac{2\pi\cdot(i)}{n})\right) \\ \vdots \\ \cos\left(h(\theta - \frac{2\pi\cdot(n-1)}{n})\right) \end{bmatrix} \tag{2.2}$$

where h is an odd positive integer ($h = 1, 3, 5, ...$), indicating the harmonic order, and i is an integer from 0 to $n-1$ ($i = 0, 1, \ldots, n-1$), θ represents the electrical angle. The magnetic flux of the h-order harmonic components in the back-EMF is denoted by ϕ_{fh}.

The generation of electromagnetic torque in an n-phase PMSM is determined through the derivative of magnetic co-energy with respect to the electrical angle (θ). The torque equation

in the original frame is articulated as:

$$T_e = \frac{dW_{co}}{d\theta} = n_p \left(\frac{1}{2} i_{s,n}^T \frac{dL_{s,n}}{d\theta} i_{s,n} + i_{s,n}^T \frac{d\phi_{fm,n}}{d\theta} \right) \tag{2.3}$$

where W_{co} denotes the magnetic co-energy and n_p represents the number of pole pairs. When the inductance matrix ($L_{s,n}$) remains constant relative to the electrical angle (θ), indicating a non-salient pole rotor, the torque expression simplifies as follows:

$$\begin{aligned} T_e &= i_{s,n}^T \underbrace{\frac{d\phi_{fm,n}}{dt}}_{\text{Back EMF}} \frac{dt}{d\theta} n_p \\ &= i_{s,n}^T \frac{e_{s,n}}{\Omega} \\ &= \frac{1}{\Omega} \sum_{i=1}^{n} i_{sk} e_{sk} \end{aligned} \tag{2.4}$$

where Ω is the mechanical speed. $e_{s,n}$ is the $n \times 1$ vector that denotes the back-EMF produced by the rotor magnet and can be expressed within the original frame in the following manner:

$$\boldsymbol{e}_{s,n} = \begin{bmatrix} e_{s1} \\ \vdots \\ e_{sn} \end{bmatrix} = - \sum_{h=1,3,5,\ldots} h n_p \Omega \phi_{fh} \begin{bmatrix} \sin\left(h(\theta - \frac{2\pi \cdot (i)}{n})\right) \\ \vdots \\ \sin\left(h(\theta - \frac{2\pi \cdot (n-1)}{n})\right) \end{bmatrix} \tag{2.5}$$

where h is an odd positive integer ($h = 1, 3, 5, ...$), indicating the harmonic order, and i is an integer from 0 to $n-1$ ($i = 0, 1, \ldots, n-1$).

The zero-sequence components are negligible because there is no homopolar current in the star-connected n-phase PMSM without a neutral conductor. Therefore, the transformation from the original frame to the stationary frame by the Clarke transformation matrix can be expressed as follows [59]:

$$\begin{bmatrix} X_{x_1} \\ X_{y_1} \\ X_{x_2} \\ X_{y_2} \\ \vdots \\ X_{x_k} \\ X_{y_k} \end{bmatrix} = \frac{2}{n} \begin{bmatrix} 1 & \cos\alpha & \cos 2\alpha & \cos 3\alpha & \cdots & \cos 3\alpha & \cos 2\alpha & \cos\alpha \\ 0 & \sin\alpha & \sin 2\alpha & \sin 3\alpha & \cdots & -\sin 3\alpha & -\sin 2\alpha & -\sin\alpha \\ 1 & \cos 2\alpha & \cos 4\alpha & \cos 6\alpha & \cdots & \cos 6\alpha & \cos 4\alpha & \cos 2\alpha \\ 0 & \sin 2\alpha & \sin 4\alpha & \sin 6\alpha & \cdots & -\sin 6\alpha & -\sin 4\alpha & -\sin 2\alpha \\ \vdots & \vdots & \vdots & \vdots & \cdots & \vdots & \vdots & \vdots \\ 1 & \cos k\alpha & \cos 2k\alpha & \cos 3k\alpha & \cdots & \cos 3k\alpha & \cos 2k\alpha & \cos k\alpha \\ 0 & \sin k\alpha & \sin 2k\alpha & \sin 3k\alpha & \cdots & -\sin 3k\alpha & -\sin 2k\alpha & -\sin k\alpha \end{bmatrix} \begin{bmatrix} X_1 \\ \vdots \\ X_n \end{bmatrix} \tag{2.6}$$

where X signifies the considered motor variables, such as voltage, current, or flux. k represents the number of orthogonal planes in which the corresponding harmonic is mapped, and

it can be calculated by [66]:

$$k = \frac{n-1}{2} \tag{2.7}$$

The harmonic distribution rule for each plane is provided as follows [66]:

$x_1 - y_1$ plane: $h = ni \pm 1$ harmonics (where i is even; $i = 0, 2, 4, \ldots$)

$x_2 - y_2$ plane: $h = ni \pm 2$ harmonics (where i is odd; $i = 1, 3, 5, \ldots$)

$\vdots$

$x_k - y_k$ plane: $h = ni \pm k$ harmonics (where i is odd when k is even, and i is even when k is odd)

Clearly, the $x_1 - y_1$ plane corresponds to the fundamental harmonic and is commonly known as the $\alpha - \beta$ plane.

The transformation from the stationary frame to the dq rotational frame is achieved by utilizing a Park transformation matrix that depends on the number of orthogonal planes (k). This transformation is expressed through a series of block-diagonal matrices, varying the electrical angle by h^{th} order harmonics, as follows [58]:

$$\begin{bmatrix} \cdots \\ X_{dh} \\ X_{qh} \\ \cdots \end{bmatrix} = \begin{bmatrix} \cdots & \cdots & \cdots & \cdots \\ \cdots & \cos(h\theta) & \sin(h\theta) & \cdots \\ \cdots & -\sin(h\theta) & \cos(h\theta) & \cdots \\ \cdots & \cdots & \cdots & \cdots \end{bmatrix} \begin{bmatrix} \cdots \\ X_{xk} \\ X_{yk} \\ \cdots \end{bmatrix} \tag{2.8}$$

By applying transformations (2.6) and (2.8) to the original frame model, the dq-frame model of an n-phase PMSM is obtained. The stator voltage equations for the h^{th} harmonic are as follows:

$$\begin{cases} v_{dh} = R_s i_{dh} + \dfrac{d\phi_{dh}}{dt} - h n_p \Omega \phi_{qh} \\ v_{qh} = R_s i_{qh} + \dfrac{d\phi_{qh}}{dt} + h n_p \Omega \phi_{dh} \end{cases} \tag{2.9}$$

The stator flux equations for the h^{th} harmonic are as follows:

$$\begin{cases} \phi_{dh} = L_{dh} i_{dh} + \phi_{fh} \\ \phi_{qh} = L_{qh} i_{qh} \end{cases} \tag{2.10}$$

where v_{dh}, v_{qh}, i_{dh}, i_{qh}, L_{dh}, and L_{qh} are the voltage, current, and inductance in the dq_h-frame influenced by the h^{th} harmonic, respectively.

The electromagnetic torque for the h^{th} harmonic is as follows:

$$T_{eh} = \frac{n}{2} n_p \left[h\phi_{fh} i_{qh} + h(L_{dh} - L_{qh}) i_{dh} i_{qh} \right] \tag{2.11}$$

The total electromagnetic torque produced by the n-phase PMSM is as follows:

$$T_e = \sum_{h=1,3,5,\ldots} T_{eh} \tag{2.12}$$

where v_{dh}, v_{qh}, i_{dh}, i_{qh}, L_{dh}, and L_{qh} represent the voltage, current, and inductance in the dq_h-frame influenced by the h^{th} harmonic, respectively. Additionally, ϕ_{fh} denotes the amplitude of the h^{th} harmonic of permanent magnet flux linkage, and R_s represents the stator resistance.

2.2.1 3-phase PMSM Modelling

Considering $n = 3$, we have $k = 1$, resulting in the presence of only the $x_1 - y_1$ plane ($\alpha - \beta$ plane). In the 3-phase PMSM, this plane predominantly comprises the fundamental harmonic along with the impaired harmonics 5, 7, and 11 (where $h = 3i \pm 1$; $i = 0, 2, 4, ...$). Figure 2.1 depicts the equivalent stator structure of star-connected windings for a 3-phase symmetrical PMSM, in which each phase shifts to another with $\alpha = 2\pi/3$.

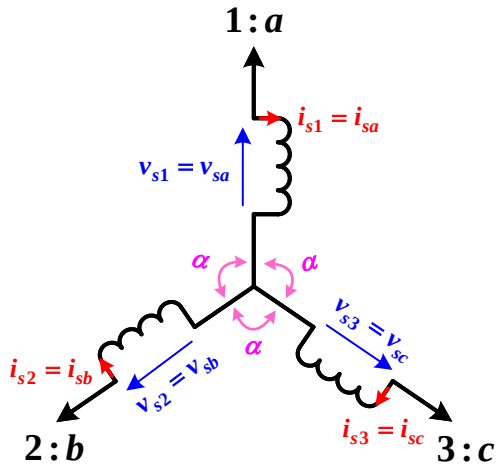

Figure 2.1: Star-connected windings of a 3-phase PMSM stator.

According to (2.1), the stator voltage equation for the 3-phase PMSM in the original frame (abc-frame) is as follows:

$$v_s = R_s i_s + \frac{d}{dt}(L_s i_s + \phi_{fm}) \tag{2.13}$$

where $v_s = [v_{sa}, v_{sb}, v_{sc}]^T$ represents the stator voltage vector, and $i_s = [i_{sa}, i_{sb}, i_{sc}]^T$ represents the stator current vector. R_s represents the 3×3 matrix that corresponds to the diagonal stator resistances. L_s represents the 3×3 matrix that corresponds to the diagonal elements representing self-inductance and off-diagonal elements denoting mutual inductance between phases. ϕ_{fm} is the 3×1 vector representing the flux linkage, and it can be expressed as follows when only the fundamental harmonic of the flux (ϕ_{f1}) is considered:

$$\phi_{fm} = \begin{bmatrix} \phi_{fma} \\ \phi_{fmb} \\ \phi_{fmc} \end{bmatrix} = \phi_{f1} \begin{bmatrix} \cos(\theta) \\ \cos\left(\theta - \frac{2\pi}{3}\right) \\ \cos\left(\theta - \frac{4\pi}{3}\right) \end{bmatrix} \tag{2.14}$$

Based on (2.4), the torque equation in the *abc*-frame is expressed as follows:

$$T_e = \frac{1}{\Omega}(i_{sa}e_{sa} + i_{sb}e_{sb} + i_{sc}e_{sc}) \tag{2.15}$$

The back-EMF for each phase is given by:

$$\begin{bmatrix} e_{sa} \\ e_{sb} \\ e_{sc} \end{bmatrix} = -n_p\Omega\phi_{f1} \begin{bmatrix} \sin(\theta) \\ \sin\left(\theta - \frac{2\pi}{3}\right) \\ \sin\left(\theta - \frac{4\pi}{3}\right) \end{bmatrix} \tag{2.16}$$

Since only the fundamental harmonic is considered in a single plane, the x_1y_1-frame is denoted as the $\alpha\beta$-frame, and the d_1q_1-frame is denoted as the dq-frame. Using (2.6) and (2.8) for a 3-phase PMSM, the transformation from the *abc*-frame to the $\alpha\beta$-frame and the transformation from the $\alpha\beta$-frame to the dq-frame can be expressed as follows, respectively:

$$\begin{bmatrix} X_\alpha \\ X_\beta \end{bmatrix} = \frac{2}{3} \begin{bmatrix} 1 & \cos\alpha & \cos\alpha \\ 0 & \sin\alpha & -\sin\alpha \end{bmatrix} \begin{bmatrix} X_a \\ X_b \\ X_c \end{bmatrix} \tag{2.17}$$

$$\begin{bmatrix} X_d \\ X_q \end{bmatrix} = \begin{bmatrix} \cos(\theta) & \sin(\theta) \\ -\sin(\theta) & \cos(\theta) \end{bmatrix} \begin{bmatrix} X_\alpha \\ X_\beta \end{bmatrix} \tag{2.18}$$

According to (2.9), (2.10), and (2.12), the model for a 3-phase PMSM in the dq-frame is given by:

$$\begin{cases} v_d = R_s i_d + \frac{d\phi_d}{dt} - n_p\Omega\phi_q \\ v_q = R_s i_q + \frac{d\phi_q}{dt} + n_p\Omega\phi_d \end{cases} \tag{2.19}$$

$$\begin{cases} \phi_d = L_d i_d + \phi_{f1} \\ \phi_q = L_q i_q \end{cases} \tag{2.20}$$

$$T_e = \frac{3}{2} n_p \left[\phi_{f1} i_q + (L_d - L_q)\, i_d i_q\right] \tag{2.21}$$

2.2.2 5-phase PMSM Modelling

Considering $n = 5$, we have $k = 2$, indicating the presence of two planes: the $x_1 - y_1$ plane and the $x_2 - y_2$ plane. The $x_1 - y_1$ plane encompasses the fundamental harmonic and multiples of the form $h = 5i \pm 1$, where i is an even integer. On the other hand, the $x_2 - y_2$ plane encompasses the third harmonic and multiples of the form $h = 5i \pm 2$, where i is an odd integer. Figure 2.2 illustrates the equivalent stator structure of star-connected windings for a 5-phase symmetrical PMSM, where each phase shifts to another with $\alpha = 2\pi/5$. Only the fundamental and third-harmonic components are considered to enhance model simplicity.

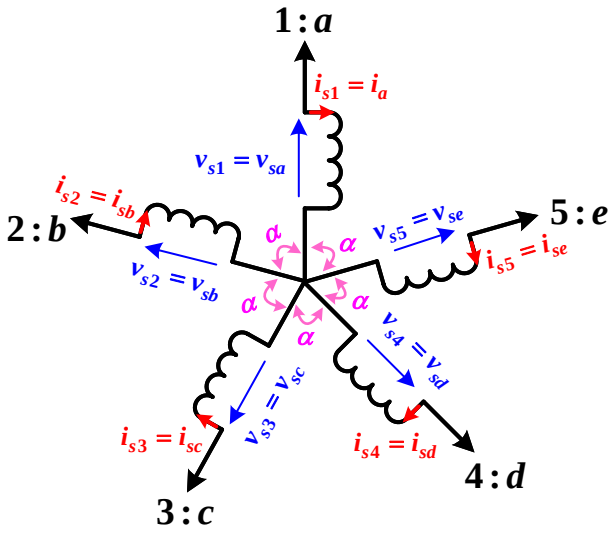

Figure 2.2: Star-connected windings of a 5-phase PMSM stator.

According to (2.1), the stator voltage equation for the 5-phase PMSM in the original frame (*abcde*-frame) is as follows:

$$v_s = R_s i_s + \frac{d}{dt}(L_s i_s + \phi_{fm}) \tag{2.22}$$

where $v_s = [v_{sa}, v_{sb}, v_{sc}, v_{sd}, v_{se}]^T$ represents the stator voltage vector, and the stator current vector is represented as $i_s = [i_{sa}, i_{sb}, i_{sc}, i_{sd}, i_{se}]^T$. R_s represents the 5×5 matrix that corresponds to the diagonal stator resistances. L_s represents the 5×5 matrix that corresponds to the diagonal elements representing self-inductance and off-diagonal elements denoting mutual inductance between phases. ϕ_{fm} is the 5×1 vector representing the flux linkage, and it can be expressed as follows when only the fundamental harmonic and third-harmonic components

of the flux (ϕ_{f1},ϕ_{f3}) are considered:

$$\phi_{fm} = \begin{bmatrix} \phi_{fma} \\ \phi_{fmb} \\ \phi_{fmc} \\ \phi_{fmd} \\ \phi_{fme} \end{bmatrix} = \phi_{f1} \begin{bmatrix} \cos(\theta) \\ \cos\left(\theta - \frac{2\pi}{5}\right) \\ \cos\left(\theta - \frac{4\pi}{5}\right) \\ \cos\left(\theta - \frac{6\pi}{5}\right) \\ \cos\left(\theta - \frac{8\pi}{5}\right) \end{bmatrix} + \phi_{f3} \begin{bmatrix} \cos(3\theta) \\ \cos\left(3\theta - \frac{6\pi}{5}\right) \\ \cos\left(3\theta - \frac{12\pi}{5}\right) \\ \cos\left(3\theta - \frac{18\pi}{5}\right) \\ \cos\left(3\theta - \frac{24\pi}{5}\right) \end{bmatrix} \tag{2.23}$$

Based on (2.4), the torque equation in the *abcde*-frame is expressed as follows:

$$T_e = \frac{1}{\Omega}(i_{sa}e_{sa} + i_{sb}e_{sb} + i_{sc}e_{sc} + i_{sd}e_{sd} + i_{se}e_{se}) \tag{2.24}$$

The back-EMF for each phase is given by:

$$\begin{bmatrix} e_{sa} \\ e_{sb} \\ e_{sc} \\ e_{sd} \\ e_{se} \end{bmatrix} = -n_p\Omega\phi_{f1} \begin{bmatrix} \sin(\theta) \\ \sin\left(\theta - \frac{2\pi}{5}\right) \\ \sin\left(\theta - \frac{4\pi}{5}\right) \\ \sin\left(\theta - \frac{6\pi}{5}\right) \\ \sin\left(\theta - \frac{8\pi}{5}\right) \end{bmatrix} - n_p\Omega\phi_{f3} \begin{bmatrix} \sin(3\theta) \\ \sin\left(3\theta - \frac{6\pi}{5}\right) \\ \sin\left(3\theta - \frac{12\pi}{5}\right) \\ \sin\left(3\theta - \frac{18\pi}{5}\right) \\ \sin\left(3\theta - \frac{24\pi}{5}\right) \end{bmatrix} \tag{2.25}$$

The x_1y_1-frame, which contains the fundamental harmonic that produces the main torque and fundamental flux, is the principal plane and is denoted as $\alpha_p\beta_p$-frame. The x_2y_2-frame, which contains the third harmonic that enhances the torque, is the second plane and is denoted as $\alpha_s\beta_s$-frame. Additionally, the rotational frames d_1q_1-frame and d_3d_3-frame are denoted as the d_pq_p-frame and the d_sq_s-frame, respectively. Using (2.6) and (2.8) for a 5-phase PMSM, the transformation from the *abcde*-frame to the $\alpha\beta$-frames and the transformation from the $\alpha\beta$-frames to the dq-frames can be expressed as follows, respectively:

$$\begin{bmatrix} X_{\alpha p} \\ X_{\beta p} \\ X_{\alpha s} \\ X_{\beta s} \end{bmatrix} = \frac{2}{5} \begin{bmatrix} 1 & \cos\alpha & \cos 2\alpha & \cos 2\alpha & \cos\alpha \\ 0 & \sin\alpha & \sin 2\alpha & -\sin 2\alpha & -\sin\alpha \\ 1 & \cos 2\alpha & \cos 4\alpha & \cos 4\alpha & \cos 2\alpha \\ 0 & \sin 2\alpha & \sin 4\alpha & -\sin 4\alpha & \sin 2\alpha \end{bmatrix} \begin{bmatrix} X_a \\ X_b \\ X_c \\ X_d \\ X_e \end{bmatrix} \tag{2.26}$$

$$\begin{bmatrix} X_{dp} \\ X_{qp} \\ X_{ds} \\ X_{qs} \end{bmatrix} = \begin{bmatrix} \cos(\theta) & \sin(\theta) & 0 & 0 \\ -\sin(\theta) & \cos(\theta) & 0 & 0 \\ 0 & 0 & \cos(3\theta) & \sin(3\theta) \\ 0 & 0 & -\sin(3\theta) & \cos(3\theta) \end{bmatrix} \begin{bmatrix} X_{\alpha p} \\ X_{\beta p} \\ X_{\alpha s} \\ X_{\beta s} \end{bmatrix} \tag{2.27}$$

According to (2.9), (2.10), and (2.12), the model for a 5-phase PMSM in the dq-frames is given by:

$$\begin{cases} v_{dp} = R_s i_{dp} + \dfrac{d\phi_{dp}}{dt} - n_p \Omega \phi_{qp} \\ v_{qp} = R_s i_{qp} + \dfrac{d\phi_{qp}}{dt} + n_p \Omega \phi_{dp} \\ v_{ds} = R_s i_{ds} + \dfrac{d\phi_{ds}}{dt} - 3n_p \Omega \phi_{qs} \\ v_{qs} = R_s i_{qs} + \dfrac{d\phi_{qs}}{dt} + 3n_p \Omega \phi_{ds} \end{cases} \tag{2.28}$$

$$\begin{cases} \phi_{dp} = L_{dp} i_{dp} + \phi_{f1} \\ \phi_{qp} = L_{qp} i_{qp} \\ \phi_{ds} = L_{ds} i_{ds} + \phi_{f3} \\ \phi_{qs} = L_{qs} i_{qs} \end{cases} \tag{2.29}$$

$$\begin{aligned} T_{e1} &= \frac{5}{2} n_p \left[\phi_{f1} i_{qp} + \left(L_{dp} - L_{qp} \right) i_{dp} i_{qp} \right] \\ T_{e3} &= \frac{5}{2} n_p \left[3\phi_{f3} i_{qs} + 3 \left(L_{ds} - L_{qs} \right) i_{ds} i_{qs} \right] \\ T_e &= T_{e1} + T_{e3} \end{aligned} \tag{2.30}$$

2.3 General FOC for n-phase PMSM

The field-oriented control (FOC) strategy is developed and applied in the dq rotating frame. Figure 2.3 illustrates the general field-oriented control structure for an n-phase PMSM, showcasing the implementation of PI controllers for the speed and current loops. To simplify the design of PI controllers for current loops, the stator voltage on the output of the controllers for each h^{th} order harmonic is expressed as:

$$\begin{cases} v_{dh}^{reg} = R_s i_{dh} + L_{dh} \dfrac{di_{dh}}{dt} \\ v_{qh}^{reg} = R_s i_{qh} + L_{qh} \dfrac{di_{dh}}{dt} \end{cases} \tag{2.31}$$

By adding the decoupling voltages (e_{dh}, e_{qh}) to the output stator voltage (2.31), the stator voltage references are obtained as follows:

$$\begin{cases} v_{dh}^{*} = v_{dh}^{reg} - e_{dh} \\ v_{qh}^{*} = v_{qh}^{reg} + e_{qh} \end{cases} \tag{2.32}$$

where $e_{dh} = h n_p \Omega L_{qh} i_{qh}$ and $e_{qh} = h n_p \Omega (L_{dh} i_{dh} + \phi_{fh})$.

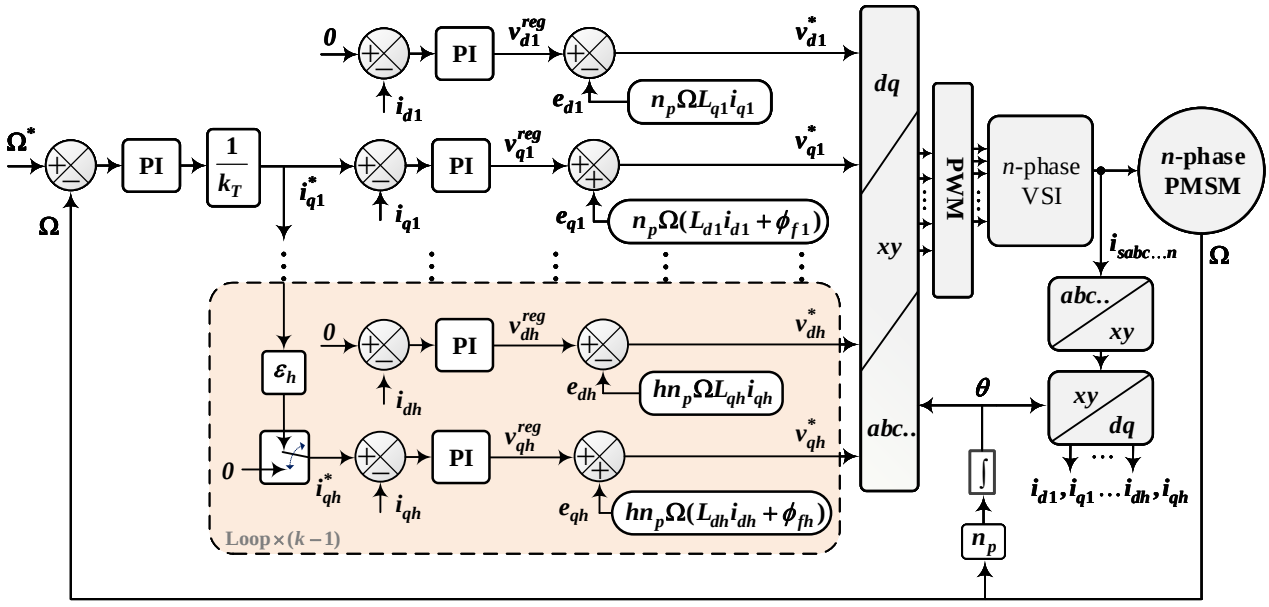

Figure 2.3: General FOC structure for n-phase PMSM using PI control.

To achieve optimal torque decoupling of the n-phase PMSM, the FOC strategy is utilized to regulate the currents in the d-axes (i_{dh}), driving them towards zero. As a result, the torque equation for the h^{th} harmonic can be succinctly formulated as follows:

$$T_{eh} = \frac{n}{2} n_p h \phi_{fh} i_{qh} \tag{2.33}$$

The ratio between the currents i_{q1} and i_{qh} depends on the characteristics of the back-EMF, as expressed by the following equation [67, 68, 69]:

$$\varepsilon_h = \frac{i_{qh}}{i_{q1}} = \frac{h\phi_{fh}}{\phi_{f1}} \tag{2.34}$$

where ε_h represents the magnetic ratio between the first-order and h^{th} order harmonic components of the back-EMF. This ratio is crucial for minimizing copper losses in the motor.

From (2.33) and (2.34), we obtain the i^*_{q1} current reference for the the fundamental harmonic as follows:

$$i^*_{q1} = \frac{T^*_e}{k_t} \tag{2.35}$$

where T^*_e represents the output of the PI controller for the speed loop, and k_t is defined as:

$$k_T = \frac{n}{2} n_p \phi_{f1} \left(\sum_{h=1,3,5,\ldots} \varepsilon_h^2 \right) \tag{2.36}$$

Based on (2.34), the i^*_{qh} current reference for the h^{th} harmonic is derived as follows:

$$i^*_{qh} = \varepsilon_h i^*_{q1} \tag{2.37}$$

It is essential to highlight that if an h^{th} order harmonic is not utilized to maximize the torque or enhance the motor efficiency, the current reference for that harmonic should be set to zero.

2.4 *n*-phase VSI PWM Strategies

The two-level voltage source inverters are commonly used for multiphase motors. Figure 2.4 shows the voltage source inverter (VSI) setup for supplying power to an n-phase PMSM. This setup is determined by the on/off states of each leg, as described in (2.38). When S_n equals 1, it means the upper switch is on, and when S_n is 0, it is the opposite. As the number of phases in the inverter increases, the available voltage space vectors follow the pattern of 2^n. For instance, a 3-phase voltage source inverter provides 8 voltage space vectors, while a 5-phase VSI offers 32 output voltage space vectors. This indicates that as the number of phases increases, designing an effective space vector PWM (SVPWM) scheme becomes more complex. However, carrier-based PWM (CPWM) for voltage source inverters is simple and can easily be adapted to inverters with more than 3 phases, making it a preferred choice for these systems.

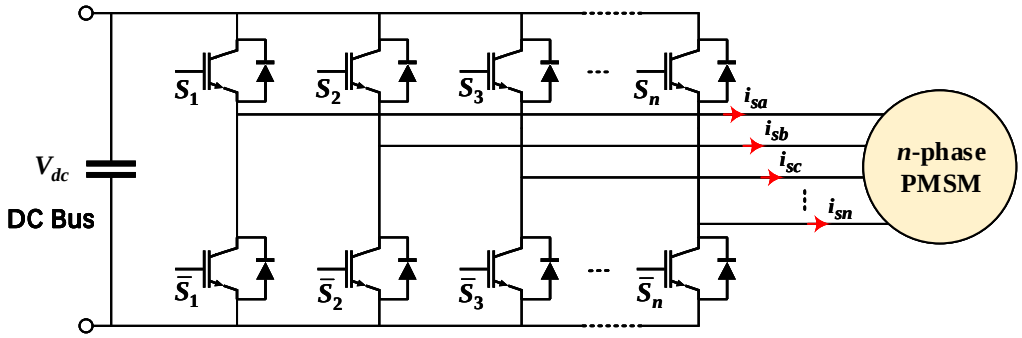

Figure 2.4: An n-phase VSI structure.

$$\begin{bmatrix} v_{sa} \\ v_{sb} \\ v_{sc} \\ \vdots \\ v_{sn} \end{bmatrix} = \frac{V_{dc}}{n} \begin{bmatrix} n-1 & -1 & -1 & \cdots & -1 \\ -1 & n-1 & -1 & \cdots & -1 \\ -1 & -1 & n-1 & \cdots & -1 \\ \vdots & \vdots & \vdots & \cdots & \vdots \\ -1 & -1 & -1 & \cdots & n-1 \end{bmatrix} \begin{bmatrix} S_1 \\ S_2 \\ S_3 \\ \vdots \\ S_n \end{bmatrix} \tag{2.38}$$

2.4.1 Carrier-based PWM

Carrier-based pulse width modulation (CPWM) stands out as the most prevalent PWM technique, owing to its straightforward implementation and effectiveness in controlling multiphase motors, even under fault conditions. The fundamental principle of CPWM is illustrated in Figure 2.5. By combining the stator voltage references in the original frame with an appropriate zero-sequence signal and comparing the resulting signal to a carrier waveform (triangular or sawtooth), CPWM generates the PWM signal. The carrier frequency is typically maintained significantly higher than the stator voltage references. A notable advantage of CPWM is its minimal computational burden compared to alternative techniques.

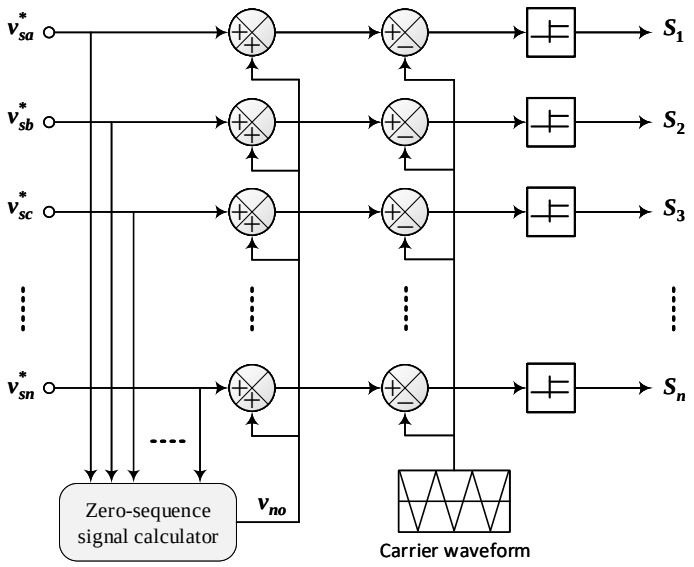

Figure 2.5: Principle of CPWM for an n-phase VSI.

To enhance the DC bus with n^{th} harmonic injection, CPWM employs the following zero-sequence signal equation [70]:

$$v_{no}(t) = -\frac{1}{2}(\max(v_a^*, v_b^*, v_c^*, \ldots, v_n^*) + \min(v_a^*, v_b^*, v_c^*, \ldots, v_n^*)) \tag{2.39}$$

2.4.2 Space Vector PWM

The analysis of Space Vector Pulse Width Modulation (SVPWM) for an n-phase VSI can be simplified by considering only two adjacent large vectors. Each plane has $2n$ sectors, and the reference voltage vector in each sector is composed of a combination of the neighboring two large vectors. The time durations of the operation and zero time for each switching period are given by (2.40) and are shown in Figure 2.6, which displays the position of the reference

vector and the neighboring available space vectors in sector N. Figure 2.7 shows a block diagram of the SVPWM to explain the concept further.

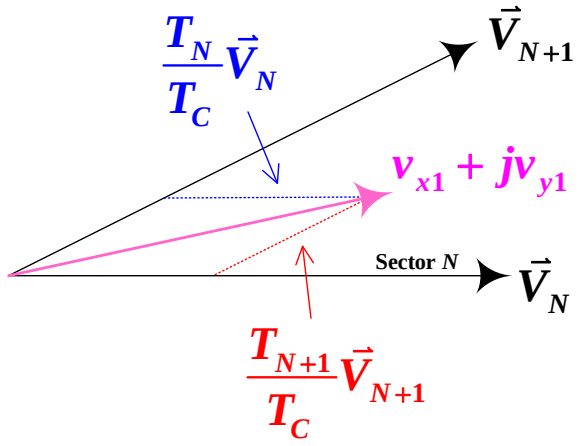

Figure 2.6: Synthesis of SVPWM voltage vectors.

$$\begin{cases} T_N = \dfrac{T_c v_{ref} \sin\left(N(180^\circ/n) - \lambda^\circ\right)}{\left|\vec{V}_N\right| \sin(180^\circ/n)} \\ T_{N+1} = \dfrac{T_c v_{ref} \sin\left(\lambda^\circ - (N-1)(180^\circ/n)\right)}{\left|\vec{V}_{N+1}\right| \sin(180^\circ/n)} \\ T_0 = T_c - T_N - T_{N+1} \end{cases} \tag{2.40}$$

where λ represents the position of the voltage reference vector, N denotes the sector number ranging from 1 to $2n$, T_c stands for the switching period, v_{ref} indicates the length of the voltage reference vector, and $\vec{V}_N$ and $\vec{V}_{N+1}$ represent two neighboring active voltage vectors. Additionally, T_N, T_{N+1}, and T_0 correspond to the application times for the two active voltage vectors and zero vectors, respectively.

2.5 Simulation Results

The structural diagram of an FOC strategy using PI control for a 5-phase PMSM is illustrated in Figure 2.8. The 5-phase PMSM model is represented by (2.28), (2.29), and (2.30), where the motor is injected with the third-harmonic component to enhance torque production. Details of the motor drive parameters are provided in Table 2. In order to generate the

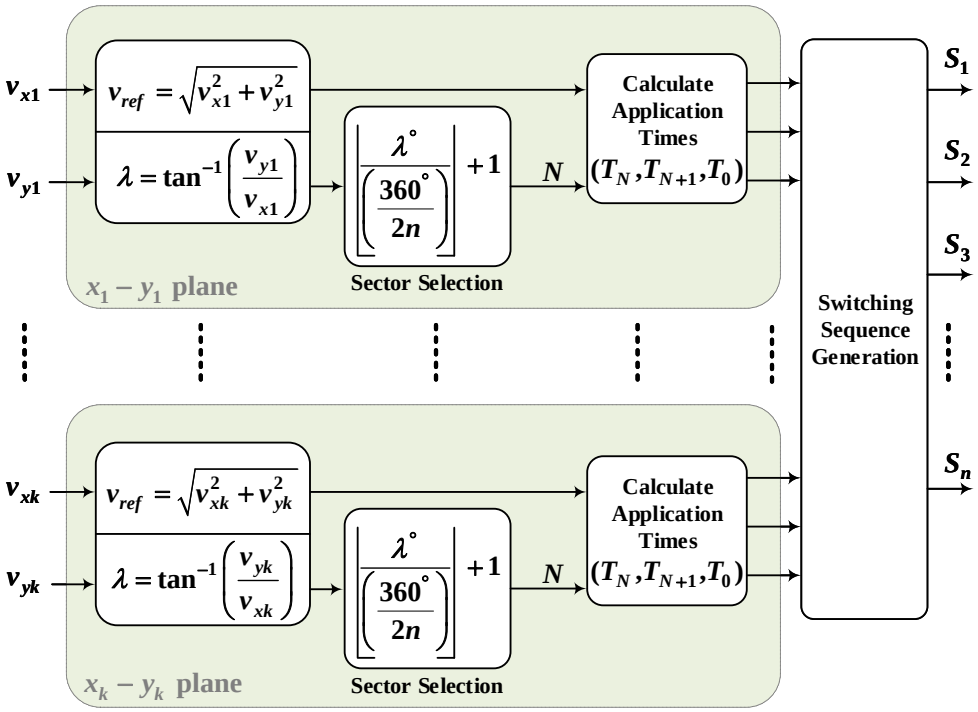

Figure 2.7: General principle of SVPWM for an n-phase VSI.

PWM signal, we compared two strategies outlined in sections 2.4.1 and 2.4.2: CPWM with 5^{th} harmonic injection and SVPWM based on the simplest strategy, which involves using only large vectors.

Figure 2.9 presents the spectrum of the stator current waveform of phase "a" obtained via fast fourier transform (FFT) in steady-state. The speed reference was set to 300 rpm and the load torque was set to 20 Nm. As observed, the CPWM exhibited a lower Total Harmonic Distortion (THD) compared to the SVPWM. The SVPWM demonstrated the presence of undesirable low-order harmonics such as the 7th and 9th harmonics, while the CPWM effectively suppressed these low-order harmonics. In conclusion, considering its simplicity of implementation and superior performance, CPWM with n^{th} harmonic injection is recommended for multi-phase PMSM applications.

In order to assess torque enhancement with 3rd harmonic current injection in a 5-phase PMSM, we compare the responses of speed, torque, and stator current both without ($i_{qs}^* = 0$) and with 3rd harmonic ($i_{qs}^* = \varepsilon_3 i_{qp}^*$) under maximum torque conditions, as depicted in Figure 2.10. The speed reference was held constant at 300 rpm, and the load torque was initially set to 20 Nm. At 1 second, the load torque was increased to 40 Nm and further

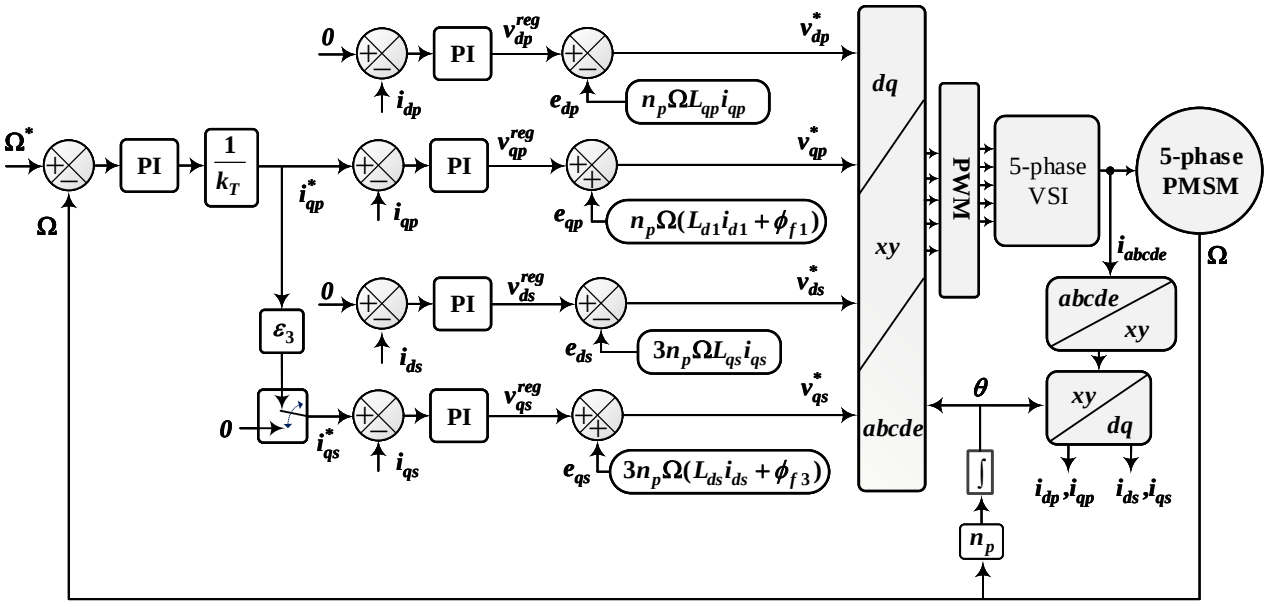

Figure 2.8: FOC structure for 5-phase PMSM using PI control.

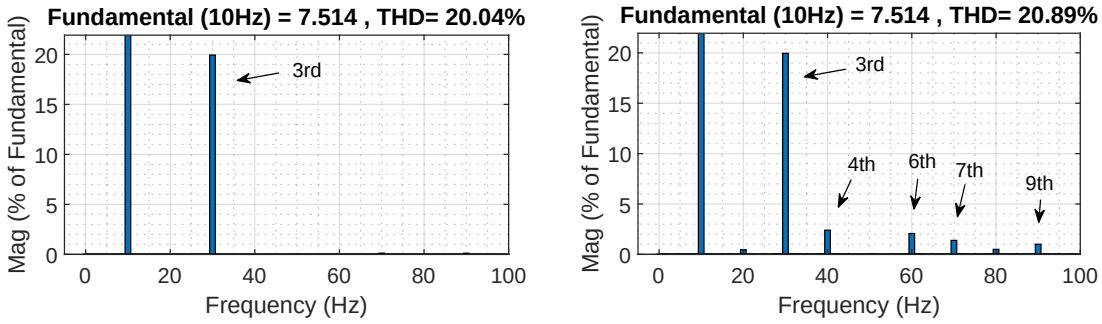

(a) CPWM.

(b) SVPWM.

Figure 2.9: Phase "a" stator current spectrum.

increased to the maximum load torque of 50 Nm at 2 seconds.

As observed, the motor's response with 3rd harmonic injection effectively returns to the speed reference under maximum load torque, demonstrating an improved torque response compared to the scenario without 3rd harmonic injection where the speed decreases under maximum load torque (50 Nm). This decrease in speed without harmonic injection is attributed to the maximum torque response being less than the applied load torque (50 Nm).

The presence of a 3rd harmonic in the phase "a' stator current of the 5-phase PMSM, as depicted in Figure 2.10c, indicates its potential for torque enhancement compared to the absence of injection shown in Figure 2.10d.

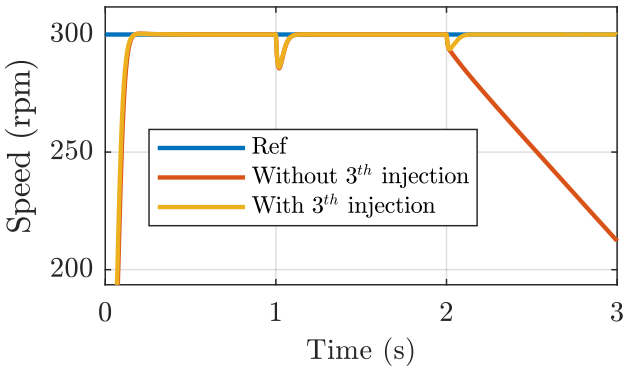

(a) Speed.

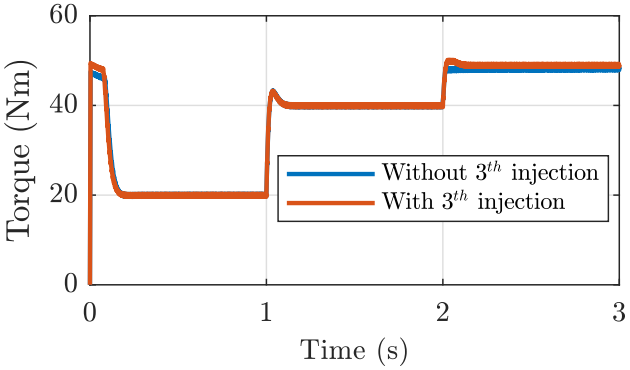

(b) Torque.

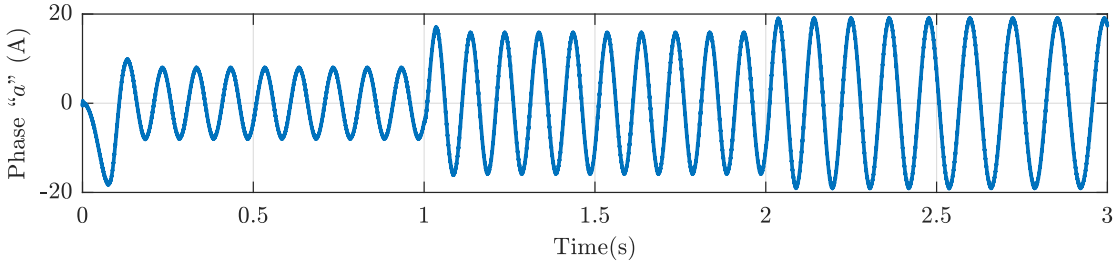

(c) Stator current of phase "a"' without 3rd harmonic injection.

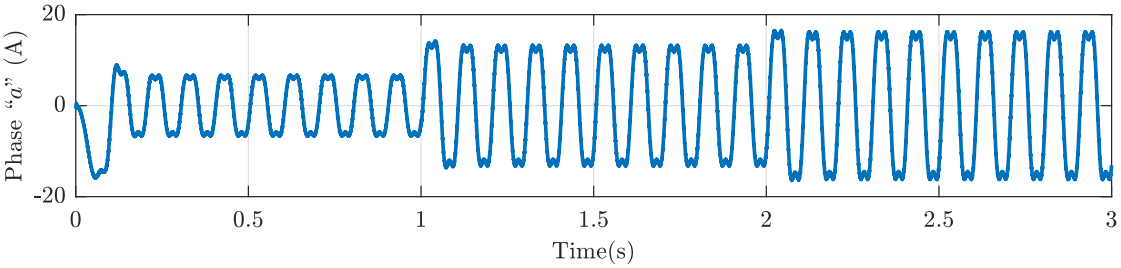

(d) Stator current of phase "a' with 3rd harmonic injection.

Figure 2.10: Comparison of FOC responses with and without harmonic injection.

2.6 Conclusion

This chapter provided a comprehensive overview of modeling and field-oriented control for n-phase PMSMs, covering models for both 3-phase and 5-phase PMSMs. Additionally, it introduced a general FOC strategy utilizing PI controllers, applicable to n-phase PMSMs. This strategy incorporated all odd harmonics of EMF components, alongside the fundamental harmonic, to achieve enhanced torque. The chapter delved into two PWM strategies for n-phase VSIs: CPWM and SVPWM. Each technique, CPWM and SVPWM, was scrutinized for its specific advantages and disadvantages, detailing their implementation and characteristics.

The simulation results presented in this chapter validated the effectiveness of FOC with 3rd harmonic current injection for 5-phase PMSMs. These results underscored the notable improvement in torque response achieved by the proposed FOC strategy under various load conditions. Furthermore, the outcomes highlighted CPWM with 5^{th} harmonic injection as a preferable PWM technique for n-phase PMSM applications, owing to its simplicity and superior performance.

In conclusion, this chapter significantly contributed to the comprehension of the modeling, control, and performance aspects of n-phase PMSMs.

Chapter 3

Anti-disturbance Sliding-mode Control of PMSMs

3.1 Introduction

The field-oriented control (FOC) method stands out as a widely embraced technique for governing Permanent Magnet Synchronous Motors (PMSMs), providing notable advantages such as seamless starting, smooth acceleration, and diminished torque ripples, thereby ensuring an efficient dynamic response [71]. However, the control of PMSMs presents challenges attributable to their model nonlinearity and susceptibility to temperature fluctuations, which impact their parameters [72, 73]. Furthermore, in numerous industrial applications, the unknown load torque necessitates the application of robust nonlinear control techniques like sliding mode control (SMC) to effectively address these challenges.

While traditional SMC exhibits insensitivity to disturbances and uncertainties, it grapples with chattering due to its inherent switching property. Various approaches have been proposed to mitigate chattering, encompassing reaching law SMC [74], super-twisting SMC [75], terminal SMC [76], adaptive SMC [77], and event-triggered SMC [78]. Super-twisting SMC, also referred to as second-order sliding mode control (SOSMC) [79], proves effective in suppressing chattering while retaining the merits of traditional SMC [80].

This chapter delves into the application of anti-disturbance sliding-mode control to PMSMs, with a particular emphasis on the utilization of SOSMC. The main objective is to enhance control performance by reducing chattering. The chapter will conduct a comparative analysis between the SOSMC strategy, PI control, and conventional SMC through simulation tests. To substantiate the effectiveness of SOSMC, experiments will be conducted on a sur-

face permanent magnet synchronous motor (SPMSM) under normal operating conditions, involving variations in speed reference and load torque. The simulation results will showcase the robustness and efficacy of the SOSMC approach.

3.2 Disturbances in the PMSM Model

In this chapter, we focus on discussing the 3-phase SPMSM as a benchmark PMSM system due to similarities in disturbances, such as unmodeled dynamics, parametric uncertainties, and external disturbances. In last chapter of this thesis, we will shift our focus to 5-phase PMSMs to address the interests of readers in related areas. According to (2.21), with SPMSM machine attributes ($L_d = L_q = L_s$), the simplified torque expression is as follows:

$$T_{em} = \frac{3}{2} n_p \Phi_f i_q \tag{3.1}$$

To facilitate the development of control laws for the SPMSM and enhance understanding of its dq-frame dynamic model, the expressions of the substitution of the stator flux equations (2.20) into the voltage equations (2.19) are as follows:

$$\begin{cases} \frac{di_d}{dt} = c_1 i_d + n_p \Omega i_q + \beta V_d \\ \frac{di_q}{dt} = c_1 i_q - n_p \Omega i_d + c_2 \Omega + \beta V_q \\ \frac{d\Omega}{dt} = c_3 i_q - \alpha_1 \Omega - \alpha_2 T_L \end{cases} \tag{3.2}$$

The components of the SPMSM model (3.2) express consistently with the machine parameters as follows: $c_1 = -\frac{R_s}{L_s}$; $c_2 = -\frac{n_p \Phi_f}{L_s}$; $c_3 = \frac{3 n_p \Phi_f}{2J}$; $\alpha_1 = \frac{f}{J}$; $\alpha_2 = \frac{1}{J}$; $\beta = \frac{1}{L_s}$.
where V_d, V_q, i_d, and i_q represent the stator voltages and currents of dq-frame, respectively; L_s is the inductance of dq-frame, respectively; R_s is the stator resistance; Φ_f is the rotor flux; Ω is the rotor speed; J is the moment of inertia; f denote friction coefficient and T_L represents the load torque; n_p is the pole pairs number of the motor.

Considering the load, perturbation parameters, and unmodeled dynamics as disturbances, the SPMSM model (3.2) can be expressed as follows:

$$\begin{cases} \frac{di_d}{dt} = c_1 i_d + n_p \Omega i_q + \beta V_d + d_{i_d} \\ \frac{di_q}{dt} = c_1 i_q - n_p \Omega i_d + c_2 \Omega + \beta V_q + d_{i_q} \\ \frac{d\Omega}{dt} = c_3 i_q - \alpha_1 \Omega + d_\Omega \end{cases} \tag{3.3}$$

where d_{i_d}, d_{i_q}, and d_Ω are the lumped disturbances given as follows:

$$\begin{pmatrix} d_{i_d} \\ d_{i_q} \\ d_\Omega \end{pmatrix} = \begin{pmatrix} \Delta c_1 i_d + \Delta \beta V_d + \delta_d \\ \Delta c_1 i_q + \Delta c_2 \Omega + \Delta \beta V_q + \delta_q \\ \Delta c_3 \Omega - \Delta \alpha_1 \Omega - \alpha_2 T_r - \Delta \alpha_2 \Delta T_L + \delta_\Omega \end{pmatrix} \tag{3.4}$$

The components in the lumped disturbances (d_{i_d}, d_{i_q}, d_Ω) represent as follows: $\Delta c_1 = -\frac{\Delta R_s}{\Delta L_s}$, $\Delta c_2 = -\frac{n_p \phi_f}{\Delta L_s}$, $\Delta c_3 = \frac{3 n_p \phi_f}{2 \Delta J}$, $\Delta \alpha_1 = \frac{\Delta f}{\Delta J}$, $\Delta \alpha_2 = \frac{1}{\Delta J}$, $\Delta \beta = \frac{1}{\Delta L_s}$.
where ΔR_s, ΔL_s, ΔJ, and Δf represent the variations in motor parameter values. δ_d, δ_q, and δ_Ω constitute the unmodeled dynamics.

3.2.1 Unmodeled Dynamics

3.2.1.1 Torque Variation Due to Motor Body Structure

The body structure of AC motors can cause different kinds of pulsating torques depending on the rotor materials used.

1) Cogging Torque: This phenomenon refers to a pulsating torque, arising from the interaction between the magnetic flux of the rotor and variations in the angular of the stator magnetic reluctance [81]. Notably, cogging torque persists even in the absence of a power source connection. The unmodeled dynamic effect due to cogging torque can be expressed as follows [81, 82]:

$$\delta_{\Omega_{cog}} = \frac{1}{J} \sum_{i=1}^{\infty} \delta_{cogi} \sin(n_p i \theta) \tag{3.5}$$

where δ_{cogi} represents the amplitude of the ith harmonic; J is the moment of inertia; θ is the electrical angle; n_p is the pole pairs of the motor. Unlike PMSM, induction motors have no cogging torque but skewed slot torque instead [83].

2) Flux Harmonics: The magnet material that is most commonly used in PMSM is Neodymium Iron Boron, which has a flux density that is sensitive to temperature changes. The demagnetization of permanent magnets due to temperature increase affects the maximum torque and the efficiency of PMSM. The unmodeled dynamic effect of flux harmonics on the electromagnetic torque can be represented as follows [81]:

$$\delta_{\Omega_{flux}} = \frac{3}{2} \frac{n_p i_q}{J} \sum_{i=1}^{\infty} \Phi_{fi} \cos(6 i \theta) \tag{3.6}$$

where Φ_{fi} represents the amplitude of the $6i$th harmonic.

3) Others: In permanent magnet motors, two primary sources of pulsating torque exist in addition to cogging torque. Commutation torque arises from the varying current rates during phase switching [84]. Another source is non-sinusoidal back electromotive force, influenced by factors such as the stator winding, rotor magnet direction, and machine imperfections [85].

3.2.1.2 Dead-Time Effects

The dead-time reduces the effective duty cycle and distorts the voltage and current waveforms [86]. This distortion becomes particularly evident when the current approaches zero, resulting in ripples in the electromagnetic torque. The unmodeled dynamics due to the impact of dead-time on stator voltages in the dq-frame can be characterized as follows [81, 87]:

$$\begin{cases} \delta_{d_{dead}} = \frac{1}{L_s} \sum\limits_{i=1}^{\infty} \delta_{di} \sin(6i\theta) \\ \delta_{q_{dead}} = \frac{1}{L_s} \sum\limits_{i=1}^{\infty} \delta_{qi} \cos(6i\theta) \end{cases} \tag{3.7}$$

where δ_{di} and δ_{qi} represent the amplitudes of 6th-order harmonic voltage signals corresponding to $\delta_{d_{dead}}$ and $\delta_{q_{dead}}$, respectively.

3.2.1.3 Measurement Error Effects

Measurement errors can impact AC motors, leading to torque ripples arising from inaccuracies in position or current measurements. To illustrate, consider the offset error in current measurements, which will contribute directly to the phase currents through the Clarke and Park transform, resulting in ripples on the dq-frame currents [88]. The representation of this error can be modeled as follows [81, 89]:

$$\begin{cases} \delta_{d_{off}} = \delta_{off} \sin(\theta + \alpha) \\ \delta_{q_{off}} = \delta_{off} \cos(\theta + \alpha) \end{cases} \tag{3.8}$$

where α represents the constant angle of displacement, and δ_{off} denotes the ripple amplitude.

3.2.2 Parametric Uncertainties

3.2.2.1 Mechanical Parameters

In permanent magnet synchronous motors systems, the inertia (J) of the rotor and load typically remain constant during short-term operations. In specific scenarios, such as electric winding machines, the system inertia may vary over time, increasing as time progresses [90]. When the inertia of the system becomes several times larger than its original value, the speed response exhibits a greater overshoot and a slower settling time [91].

3.2.2.2 Electrical Parameters

The design of the motor controller relies on the accuracy of the thermal model of AC machines in accounting for heat effects [92]. The thermal model plays a crucial role in effectively

estimating disturbances and uncertainties. Specifically, the stator resistance (Rs) is influenced primarily by the winding temperature, with negligible consideration for minor factors such as skin and stray losses [93]. The formula to calculate the resistance R_s at a given temperature T is expressed as follows [81]:

$$R_s = R_0(235 + T)/(235 + T_0) \tag{3.9}$$

where R_0 represents the resistance at temperature T_0. According to the PMSM model (3.3), variations in the stator resistance directly impact the current loop, thereby significantly affecting the performance of current-loop controllers.

The stator inductance, L_s, is difficult to determine accurately, as it depends on magnetic saturation [94]. To exemplify, cross-saturation can vary the stator inductances, affecting the motor's plant gain and open-loop electrical time constant.

3.2.3 External Disturbances

3.2.3.1 Friction Torque

Friction is the force that resists the relative motion of two surfaces in contact with each other. Friction can be described by different models, depending on whether they consider the time-varying effects of friction or not. Static models assume that friction is only a function of the relative velocity and the normal force between the surfaces. Some examples of static models are the coulomb model, the stribeck model, and the karnppp model. Dynamic models account for the history-dependent effects of friction, such as hysteresis, stick-slip, and pre-sliding. Some examples of dynamic models are the luGre model, the bristle model, the dahl model, and the reset integrator model. Friction is a common source of nonlinearity in servo systems, and it can cause errors such as tracking lags, steady-state errors, and limit cycles in position controllers [95]. For instance, using the stribeck model, the friction torque T_{fric} can be written as [81, 95]:

$$T_{fric} = (T_c + (T_s - T_c)e^{-(\frac{\Omega}{\Omega_s})^2})sign(\Omega) + f\Omega \tag{3.10}$$

where T_s represents the static friction torque, T_c denotes the coulomb friction torque, Ω_s stands for the mechanical stribeck velocity.

3.2.3.2 Load Torque

The load torque refers to the force applied to the load side of the motor, influencing the speed and stability of the motor system. An illustration of this impact is the potential vibration

and resonance in the transmission mechanism, which may occur due to its not being perfectly rigid [96]. Changes in load torque inevitably lead to alterations in motor speed.

3.2.3.3 Mechanical Factors

Another factor that affects the servo performance of motor drives is the mechanical properties of the system. These include the vibrations caused by twisting the shaft, the gaps between the gears, and the faults that occur when the shaft is not aligned properly. These faults can damage the shaft or break it completely. Most of the vibration problems in industrial motor drives are due to the shaft being misaligned, which accounts for more than 70% of the cases [97].

3.3 SMC Design and Analysis

Sliding mode control (SMC) is a powerful technique for designing controllers capable of handling uncertainties and disturbances in dynamic systems. It was originally developed in the 1977s by Utkin [98]. The main idea of SMC is to drive the system state to a sliding surface where the system behaves as desired, and then to maintain it on the surface by switching the control input between two or more values. SMC offers numerous advantages, including simplicity, robustness, and high performance, making it attractive for various applications, particularly in the field of motor systems.

The most commonly defined sliding surface, which ensures the convergence of the state to its reference as given by Slotine [99], is expressed as follows:

$$s(x) = \left(\frac{d}{dt} + \lambda\right)^{r-1} e(x) \tag{3.11}$$

where $e(x) = (x_{ref} - x)$, λ and r represent the error between the state and its reference, a positive constant, and the relative degree, respectively.

The traditional sliding mode control law, which drives the sliding variable to zero in finite time, was first proposed by [100]. It can be considered as:

$$\dot{s} = -k\,\mathrm{sign}(s) + \rho \tag{3.12}$$

where k is a positive constant, and ρ is the perturbation term.

The advantage of the second-order second-order sliding mode control (SOSMC) over the traditional SMC is that it more precisely accounts for nonlinearities and uncertainties, thanks

to integral action. Furthermore, integral action is well-recognized for boosting control efficiency when dealing with uncertainty. The phase plane diagram in Figure 3.1 illustrates the mechanism of the traditional SMC and SOSMC methods when exposed to a random sinusoidal perturbation term. The SOSMC law, which utilizes a super-twisting algorithm, is outlined by [101] as follows:

$$\begin{cases} \dot{s} = -k_1\sqrt{|s|}\,\mathrm{sign}(s) + U + \rho_1 \\ \dot{U} = -k_2\,\mathrm{sign}(s) + \rho_2 \end{cases} \tag{3.13}$$

where k_1 and k_2 are positive constants; ρ_1 and ρ_2 are perturbation terms.

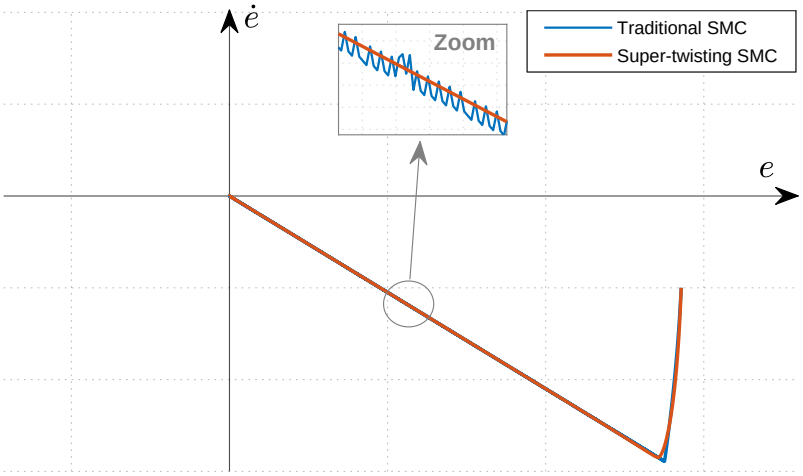

Figure 3.1: Sliding-mode mechanism in phase plane.

3.3.1 Application of SOSMC to 3-phase SPMSM

The sliding surfaces are defined as follows:

$$\begin{cases} s_1 = \Omega - \Omega_{ref} \\ s_2 = i_q - i_{q_{ref}} \\ s_3 = i_d - i_{d_{ref}} \end{cases} \tag{3.14}$$

The SOSMC laws for the speed and dq-frame currents controllers are presented below. The speed controller law is given by:

$$\begin{cases} i_{q_{ref}} = \dfrac{1}{c_3}\left(\alpha_1\Omega + \dot{\Omega}_{ref}\right) - k_{1\Omega}\sqrt{|s_1|}\,\mathrm{sign}\,(s_1) + U_\Omega \\ \dot{U}_\Omega = -k_{2\Omega}\,\mathrm{sign}\,(s_1) \end{cases} \tag{3.15}$$

The q-axis current controller law is given by:

$$\begin{cases} V_{q_{ref}} = \dfrac{1}{\beta}\left(-c_1 i_q + n_p \Omega i_d - c_2 \Omega + \dot{i}_{q_{ref}}\right) - k_{1q}\sqrt{|s_2|}\,\mathrm{sign}\,(s_2) + U_q \\ \dot{U}_q = -k_{2q}\,\mathrm{sign}\,(s_2) \end{cases} \tag{3.16}$$

The d-axis current controller law is given by:

$$\begin{cases} V_{d_{ref}} = \dfrac{1}{\beta}\left(-c_1 i_d - n_p \Omega i_q + \dot{i}_{d_{ref}}\right) - k_{1d}\sqrt{|s_3|}\,\mathrm{sign}\,(s_3) + U_d \\ \dot{U}_d = -k_{2d}\,\mathrm{sign}\,(s_3) \end{cases} \tag{3.17}$$

3.3.1.1 Stability Analysis

The proposed Lyapunov function for the control is shown in [101] as follows:

$$V = 2k_2|s| + \frac{1}{2}U^2 + \frac{1}{2}\Big(k_1|s|^{1/2}\,\mathrm{sign}(s) - U\Big)^2 \tag{3.18}$$

Additionally, the Lyapunov function can be represented in a quadratic form as follows:

$$V = \zeta^T P \zeta \tag{3.19}$$

where $\zeta^T = \begin{bmatrix} |s|^{1/2}\,\mathrm{sign}(s) & U \end{bmatrix}$, $P = \frac{1}{2}\begin{bmatrix} 4k_2 + k_1^2 & -k_1 \\ -k_1 & 2 \end{bmatrix}$.

Taking the time derivative of (3.19) yields:

$$\dot{V} = -\frac{1}{2}k_1|s|^{-1/2}\zeta^T q \zeta \tag{3.20}$$

where $q = \frac{k_1}{2}\begin{bmatrix} 2k_2 + k_1^2 & -k_1 \\ -k_1 & 1 \end{bmatrix}$.

The perturbation terms are as follows: $\rho_{1\Omega}$=d_Ω, ρ_{1q}= d_{i_q}, ρ_{1d}=d_{i_d}. It should be noted that the second terms, $\rho_{2\Omega}$, ρ_{2q}, and ρ_{2d}, do not exist and are equal to zero. The perturbation terms are globally bounded, as follows:

$$\begin{cases} |\rho_{1\Omega}| \le \delta_\Omega\sqrt{|s_1|} \\ |\rho_{1q}| \le \delta_q\sqrt{|s_2|} \\ |\rho_{1d}| \le \delta_d\sqrt{|s_3|} \end{cases} \tag{3.21}$$

where δ_Ω, δ_q, and δ_d are bounding known positive constants. To assure the stability of the

system ($\dot{V} < 0$), we must select control gains that satisfy the following conditions:

$$\begin{cases} k_{1\Omega} > 2\delta_{\Omega} \\ k_{2\Omega} > k_{1\Omega}\frac{5\delta_{\Omega}k_{1\Omega}+4\delta_{\Omega}^2}{2(k_{1\Omega}-2\delta_{\Omega})} \end{cases}$$
$$\begin{cases} k_{1q} > 2\delta_{q} \\ k_{2q} > k_{1q}\frac{5\delta_{q}k_{1q}+4\delta_{q}^2}{2(k_{1q}-2\delta_{q})} \end{cases} \tag{3.22}$$
$$\begin{cases} k_{1d} > 2\delta_{d} \\ k_{2d} > k_{1d}\frac{5\delta_{d}k_{1d}+4\delta_{d}^2}{2(k_{1d}-2\delta_{d})} \end{cases}$$

3.3.1.2 Chattering Attenuation

The main shortcoming of sliding mode control is the chattering phenomenon. This undesirable effect can be attributed to the utilization of the sign function within the control algorithm. To further smooth the control output and reduce noise, it is suggested to replace the sign function with the sigmoid function [101], represented as:

$$F = \frac{s}{|s| + m} \tag{3.23}$$

where m is a small positive parameter, such as: $|s| >> m$.

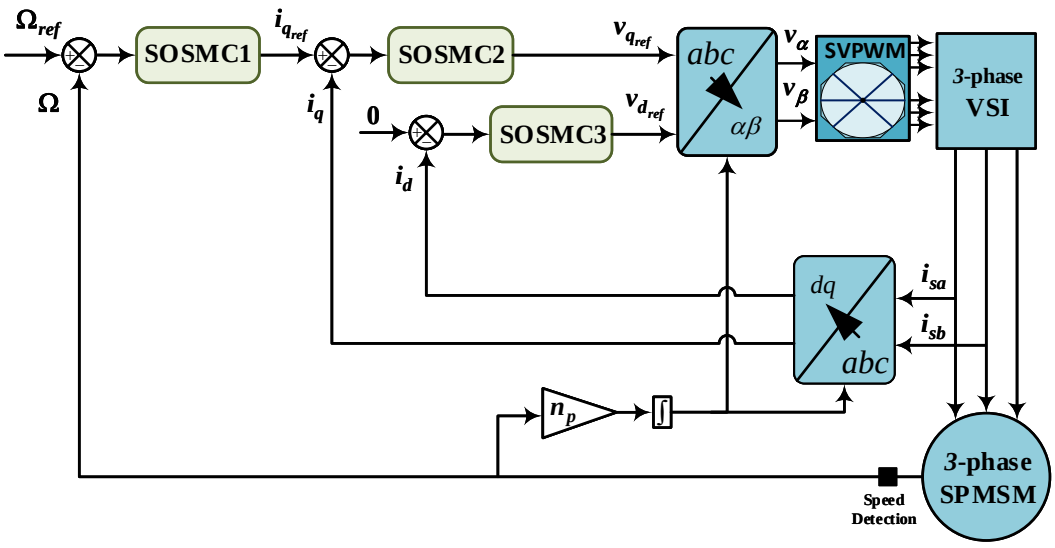

Figure 3.2: Diagram of FOC based on SOSMC.

3.4 Simulation Results

The simulation results sections presented in all chapters of this thesis were obtained through a processor-in-the-loop (PIL) experiment implemented in MATLAB/Simulink. PIL experimentation is a valuable tool for evaluating control systems on hardware, as it allows the control algorithm to be executed in real-time.

To verify the proposed control, a PIL experiment was conducted, with the setup shown in Figure 3.3. This procedure enabled the verification of the proposed control algorithm by generating code onto the embedded processor dual-core of the DSP card (TMS320F28069M) via serial communication. The code executed on the DSP card in a single cycle and then transmitted the results back to Simulink. This allowed for the PWM signals to be generated and fed into the inverter, which in turn supplied power to the motor. The output speed from the motor was continuously compared to the speed reference in the controller operating in real-time. The PMSM and inverter models were not physically present but were simulated in Simulink with a fixed step size of 1×10^{-6} s.

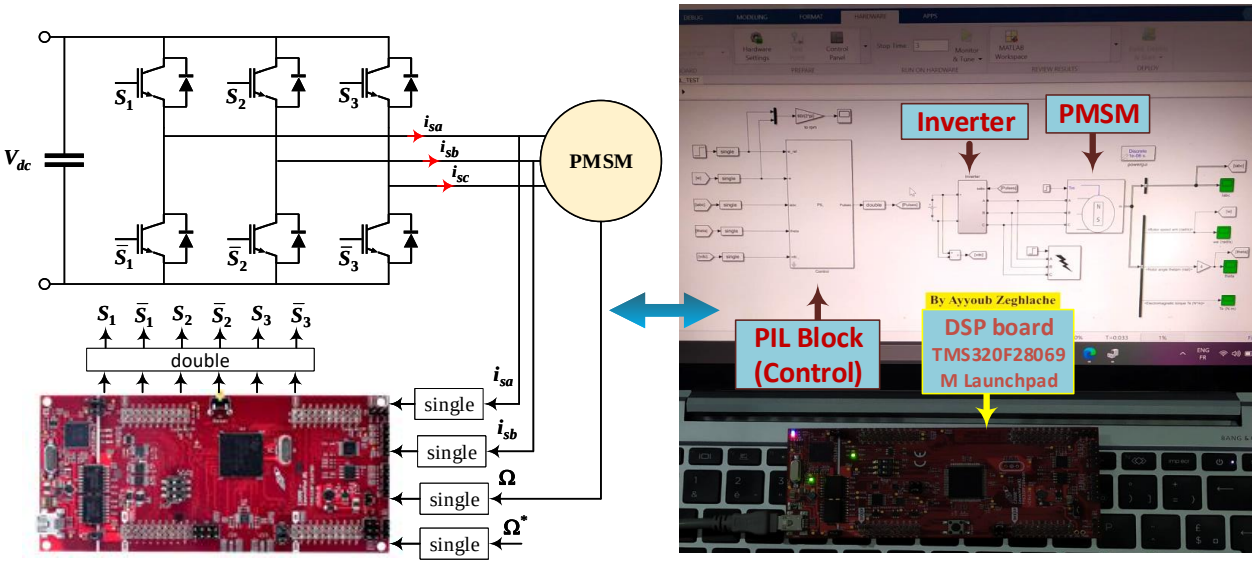

Figure 3.3: PIL experiment.

Using the structural diagram of the field-oriented control based on SOSMC (Figure 3.2) with $i_{d_{ref}} = 0$, the simulation results were derived. The SOSMC strategy for SPMSM was evaluated by a simulation test and compared with PI control and conventional SMC. Table A.1 shows the parameters for the SPMSM drive. The conventional SMC used the same sliding surfaces as the SOSMC design, but it also required estimating the load torque

by applying the following equation (3.24):

$$\dot{\hat{T}}_r = -\eta S_1 \ \eta > 0 \tag{3.24}$$

An experiment was conducted on a SPMSM under normal operating conditions, involving changes in speed reference and load torque to verify the effectiveness of the SOSMC. The variation in load torque is depicted in Figure 3.4a, starting with a speed reference of 1500 rpm and a rated load torque of 28.4 Nm. The motor experienced a sudden torque increase to 38.4 Nm at 0.4 s, returning to its initial value of 28.4 Nm at 0.8 s. The variation in speed reference is illustrated in Figure 3.4b, increasing from 750 rpm at time 0 s to its nominal value of 1500 rpm at 0.5 s.

Three control techniques: PI control, traditional SMC, and SOSMC, are compared in Figure 3.4 for their speed responses to sudden variations in load torque and speed reference. The comparison shows that the speed response of SOSMC had the least oscillation and fluctuation in the speed response among the three methods. Moreover, the response of PI control was slower in following the reference speed than SMC and SOSMC. On the other hand, SOSMC achieved a faster settling time to reach a steady state, less overshooting, and without needing load torque estimation.

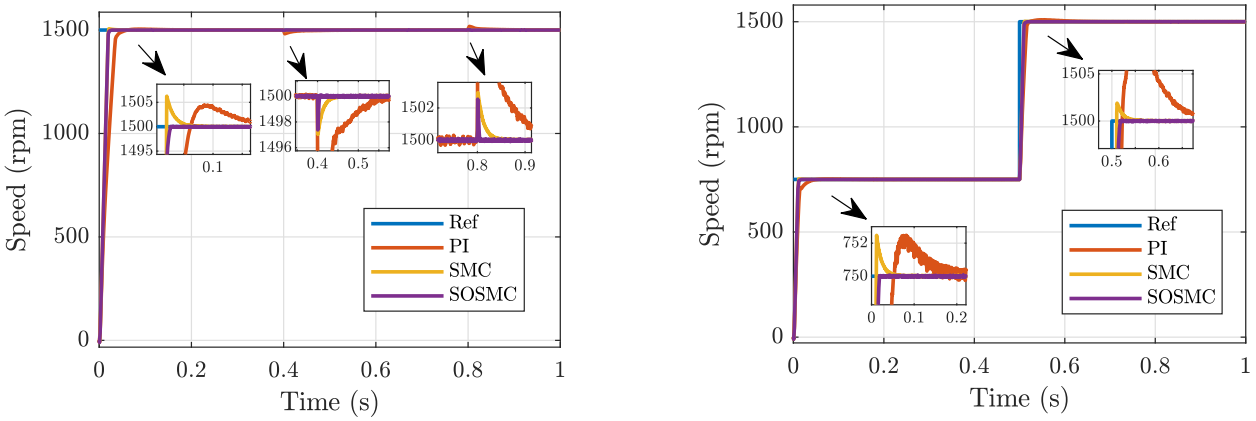

(a) Variation in load torque.

(b) Variation in speed reference.

Figure 3.4: Speed performance under healthy conditions.

To demonstrate the robustness of the SOSMC under healthy conditions, we will analyze the effects of parameter uncertainties and unmodeled dynamics. The speed reference and load torque are set to nominal values of 1500 rpm and 28.4 Nm, respectively (see Figure 3.5). At 0.5 s, the parameter uncertainties of the SPMSM in this scenario are set as follows: $\Delta R_s = +60\%R_s$, $\Delta L_s = -30\%L_s$, $\Delta J = +80\%J$, $\Delta f = +100\%f$. Regarding the dead-time effects, as shown in (3.7), the two remaining unmodeled dynamics (δ_d, δ_q) are assigned

as $\frac{50}{L_s}\sin(6\theta)$ and $\frac{80}{L_s}\cos(6\theta)$, respectively. The results show that the SOSMC demonstrates robust and effective control in dealing with the lumped disturbances.

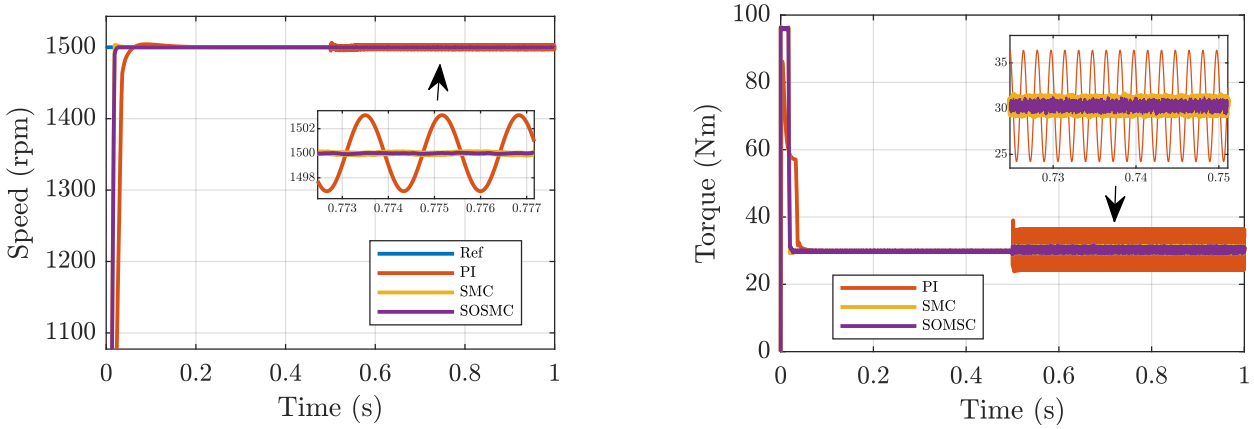

(a) Speed performance.

(b) Torque performance.

Figure 3.5: Performance in presence of lumped disturbances.

3.5 Conclusion

This chapter has demonstrated the effectiveness of the SMC strategy, especially the SOSMC, for controlling PMSMs under various disturbances and uncertainties. The SOSMC strategy was able to handle load torque variations, speed reference changes, parameter uncertainties, and unmodeled dynamics, thereby achieving robust and optimal control performance. The simulation results confirmed that the SOSMC strategy outperformed the PI control and conventional SMC in terms of speed tracking, torque ripple reduction, and chattering elimination. The next chapters will explore active fault tolerant control methods for PMSMs, and how the sliding mode control strategy can be modified to cope with different types of faults.

Chapter 4

FTC of 3-phase PMSM

4.1 Introduction

The extensive application of permanent magnet synchronous motors (PMSMs) is marred by persistent challenges associated with unanticipated shutdowns and malfunctions stemming from eccentricity, demagnetization, and stator faults [102]. Among these, short-circuit faults in the motor phases are particularly prevalent, given the substantial voltage and temperature stresses imposed on the stator coils [103]. Furthermore, PMSMs, comprised of permanent magnets, are susceptible to demagnetization faults, leading to a significant reduction in efficiency, which may arise from environmental factors and electromagnetic fields. As highlighted by [104], operating in an environment with a high temperature of 100 °C can result in a notable 20% reduction in permanent magnet flux. In light of these challenges, various strategies have been proposed to detect and mitigate the effects of these faults, with the aim of preventing sudden failures and extending the operational lifespan of PMSMs [74, 105, 106, 107, 108, 109].

This chapter aims to tackle these issues by introducing a novel fault-tolerant control (FTC) strategy that combines second-order sliding mode Control (SOSMC) with a fuzzy extended state observer (FESO). The primary objective is to ensure the robust operation of PMSMs, particularly in the face of demagnetization faults and short-circuit faults.

The succeeding sections of this chapter provide a comprehensive exploration of the proposed FTC strategy. It begins by delving into the PMSM model under the influence of modelled faults, representing sinusoidal components in the dq-frame currents. Additionally, the chapter introduces the PMSM model under demagnetization fault. Subsequent sections detail the proposed FTC, designed based on FESO and implemented through reconstruction

control. The chapter concludes with sections presenting simulation results and summarizing the overall findings.

4.2 Modelled Faults in the PMSM Model

A PMSM becomes asymmetric due to electrical faults. This produces harmonics in the spectrum of stator current [110]. As stated in [111], incorporating a sinusoidal component into the dq-frame currents can represent these faults.

$$\begin{cases} i_d \rightarrow i_d + \sum_{i}^{n_f} A_i \sin(\omega_i t + \theta_i) \\ i_q \rightarrow i_q + \sum_{i}^{n_f} A_i \cos(\omega_i t + \theta_i) \\ \omega_i = 2\pi.(F_{fault} + F_s) \\ i = 1, ..., n_f \end{cases} \tag{4.1}$$

where n_f represents the number of harmonics produced by the faults, A_i and θ_i are the unknown amplitude and phase parameters that describe the initial condition of the fault. F_s is the fundamental frequency, and F_{fault} is the characteristic frequency of the fault. The fault frequency can be easily detected and analyzed using MCSA [7].

The following exosystem is able to model the faults depicted below:

$$\dot{z} = S \cdot z \tag{4.2}$$

$$\text{where} \begin{cases} S = diag(S_i) \\ S_i = \begin{bmatrix} 0 & \omega_i \\ -\omega_i & 0 \end{bmatrix} \text{ with } \begin{cases} size(S) = 2n_f \times 2n_f \\ size(z) = 2n_f \times 1 \end{cases} . \\ i = 1, 2, \ldots, n_f \end{cases}$$

The dq-frame currents described in (4.1) with perturbing terms can be rewritten as follows:

$$\begin{cases} i_d \rightarrow i_d + Q_d Z \\ i_q \rightarrow i_q + Q_q Z \end{cases} \tag{4.3}$$

$$\text{where} \begin{cases} Q_d = \begin{bmatrix} 1 & 0 & 1 & \ldots & 1 & 0 \end{bmatrix} \\ Q_q = \begin{bmatrix} 0 & 1 & 0 & \ldots & 0 & 1 \end{bmatrix} \end{cases} .$$

Using the ecosystem (4.2), the derivatives of currents can be determined as follows:

$$\begin{cases} \dot{i}_d \rightarrow \dot{i}_d + Q_d \cdot S \cdot Z \\ \dot{i}_q \rightarrow \dot{i}_q + Q_q \cdot S \cdot Z \end{cases} \tag{4.4}$$

Substituting (4.3) and (4.4) into (3.2) yields the dq-frame currents of 3-phase SPMSM model in presence of modelled faults, which are:

$$\begin{cases} \frac{di_d}{dt} = c_1 i_d + n_p \Omega i_q + \beta V_d + f_d \\ \frac{di_q}{dt} = c_1 i_q - n_p \Omega i_d + c_2 \Omega + \beta V_q + f_q \end{cases} \tag{4.5}$$

where $\begin{pmatrix} f_d \\ f_q \end{pmatrix} = \begin{pmatrix} c_1 Q_d z + n_p Q_q \Omega z + Q_d S z \\ c_1 Q_q z - n_p Q_d \Omega z + Q_q S z \end{pmatrix} = \Gamma z$; with $\Gamma = \begin{pmatrix} c_1 Q_d + n_p Q_q \Omega + Q_d S \\ c_1 Q_q - n_p Q_d \Omega + Q_q S \end{pmatrix}$.

4.3 SPMSM Model Under Demagnetization Fault

Magnets can lose their magnetic properties permanently due to factors beyond their control, such as high temperatures. When this occurs, the permanent magnets will undergo changes in the amplitude and direction of their flux linkage. Figure 4.1 illustrates these variations, where the flux linkage amplitude transitions from Φ_f to Φ_r, and the flux linkage direction shifts by an angle of γ.

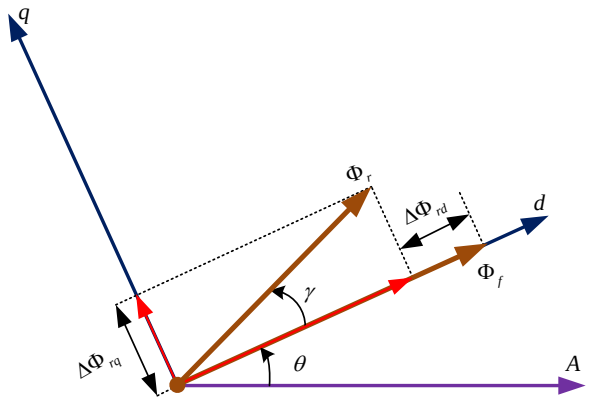

Figure 4.1: Variation of SPMSM flux-linkage.

When a demagnetization fault occurs in a SPMSM, the flux linkage of the rotor will be affected as follows:

$$\begin{cases} \Phi_d = L_d i_d + \Phi_f + \Delta\Phi_{rd} \\ \Phi_q = L_q i_q + \Delta\Phi_{rq} \end{cases} \tag{4.6}$$

where $\Delta\Phi_{rd} = \Phi_r \cos\gamma - \Phi_f$ and $\Delta\Phi_{rq} = \Phi_r \sin\gamma$ represent perturbation values for flux linkage components along the dq-frame.

The electromagnetic torque (3.1) will become as follows:

$$T_{em} = \frac{3}{2} n_p \Phi_f i_q + \frac{3}{2} n_p (\Delta\Phi_{rd} i_q - \Delta\Phi_{rq} i_d) \tag{4.7}$$

Substituting (4.6) into (2.19) yields the state equation of a SPMSM in the presence of demagnetization fault, as follows:

$$\begin{cases} \frac{di_d}{dt} = c_1 i_d + n_p \Omega i_q + \beta V_d + f_d \\ \frac{di_q}{dt} = c_1 i_q - n_p \Omega i_d + c_2 \Omega + \beta V_q + f_q \\ \frac{d\Omega}{dt} = c_3 i_q - \alpha_1 \Omega + f_\Omega \end{cases} \tag{4.8}$$

where $\begin{pmatrix} f_d \\ f_q \\ f_\Omega \end{pmatrix} = \begin{pmatrix} \frac{n_p}{L_s} \Delta\Phi_{rq} \Omega \\ -\frac{n_p}{L_s} \Delta\Phi_{rd} \Omega \\ \frac{3n_p}{2J} \left(\Delta\Phi_{rd} i_q - \Delta\Phi_{rq} i_d \right) - \alpha_2 T_r \end{pmatrix}$.

4.4 Design of Fuzzy Extended State Observer

In order to design an ESO for the PMSM, it is imperative to formulate a comprehensive model of the motor. This model can be precisely defined through the utilization of state equations, as delineated below:

$$\begin{cases} \dot{x} = Ax(t) + Bu(t) + D\dot{f}(t) \\ y = Cx(t) \end{cases} \tag{4.9}$$

In accordance with the state equation (4.9), the traditional design methodology for the ESO of the SPMSM is structured as follows:

$$\dot{\hat{x}}(t) = A\hat{x}(t) + Bu(t) + D\dot{\hat{f}}(t) + h(y(t) - \hat{y}(t)) \tag{4.10}$$

where $\hat{x}(t)$, $\hat{y}(t)$ and $\hat{f}(t)$ are the estimates of $x(t)$, $y(t)$ and $f(t)$, respectively; h is the observer gain matrix.

By integrating fault terms as additional states, the extended state-space model for stator currents in SPMSM is presented as follows:

$$\begin{aligned} \frac{d}{dt} \begin{bmatrix} i_d \\ i_q \\ f_d \\ f_q \end{bmatrix} &= \begin{bmatrix} c_1 & n_p\Omega & 1 & 0 \\ -n_p\Omega & c_1 & 0 & 1 \\ 0 & 0 & 0 & 0 \\ 0 & 0 & 0 & 0 \end{bmatrix} \begin{bmatrix} i_d \\ i_q \\ f_d \\ f_q \end{bmatrix} + \begin{bmatrix} 0 \\ c_2\Omega \\ 0 \\ 0 \end{bmatrix} \\ &+ \begin{bmatrix} \beta & 0 \\ 0 & \beta \\ 0 & 0 \\ 0 & 0 \end{bmatrix} \begin{bmatrix} V_d \\ V_q \end{bmatrix} + \begin{bmatrix} 0 & 0 \\ 0 & 0 \\ 1 & 0 \\ 0 & 1 \end{bmatrix} \begin{bmatrix} \dot{f}_d \\ \dot{f}_q \end{bmatrix} \end{aligned} \tag{4.11}$$

where $x(t) = \begin{bmatrix} i_d & i_q & f_d & f_q \end{bmatrix}^T$ is the state vector; $u(t) = \begin{bmatrix} V_d & V_q \end{bmatrix}^T$ is the control vector; $y(t) = \begin{bmatrix} i_d & i_q \end{bmatrix}^T$ is the output vector; $f(t) = \begin{bmatrix} f_d & f_q \end{bmatrix}^T$ represents the demagnetization fault affecting the SPMSM.

It is evident that the system described by (4.11) possesses full rank and is observable. The FESO equations for the currents can be obtained in the following manner:

$$\begin{cases} \dot{\hat{i}}_d = c_1 \hat{i}_d + n_p \Omega \hat{i}_q + \hat{f}_d + \beta V_d + h_{d1} FLC_d \\ \dot{\hat{f}}_d = h_{d2} FLC_d \end{cases} \quad \begin{cases} \dot{\hat{i}}_q = -n_p \Omega \hat{i}_d + c_1 \hat{i}_q + \hat{f}_q + \beta V_q + h_{q1} FLC_q \\ \dot{\hat{f}}_q = h_{q2} FLC_q \end{cases} \tag{4.12}$$

where h_{d1}, h_{d2}, h_{q1}, and h_{q2} are constants that are all positive; $\hat{f}_d$ and $\hat{f}_q$ are the estimates of f_d and f_q, respectively.

The extended state-space model describing the speed of SPMSM can be articulated as follows:

$$\frac{d}{dt} \begin{bmatrix} \Omega \\ f_\Omega \end{bmatrix} = \begin{bmatrix} -\alpha_1 & 1 \\ 0 & 0 \end{bmatrix} \begin{bmatrix} \Omega \\ f_\Omega \end{bmatrix} + \begin{bmatrix} c_3 \\ 0 \end{bmatrix} i_q + \begin{bmatrix} 0 \\ 1 \end{bmatrix} \dot{f}_\Omega \tag{4.13}$$

where $x(t) = \begin{bmatrix} \Omega & f_\Omega \end{bmatrix}^T$ is the state vector; $u(t) = i_q$ is the input; $y(t) = \Omega$ is the output; $f(t) = f_\Omega$ represents the total perturbation arising from demagnetization fault and load.

To estimate the state f_Ω in system (4.13), a FESO for the speed can be derived as follows:

$$\begin{cases} \dot{\hat{\Omega}} = -\alpha_1 \hat{\Omega} + \hat{f}_\Omega + c_3 i_q + h_{\Omega 1} FLC_\Omega \\ \dot{\hat{f}}_\Omega = h_{\Omega 2} FLC_\Omega \end{cases} \tag{4.14}$$

where $h_{\Omega 1}$ and $h_{\Omega 2}$ are both positive constants.

The IT2FLC functions by taking the error signal ($i_d - \hat{i_d}$, $i_q - \hat{i_q}$, $\Omega - \hat{\Omega}$) as input and employing proportional, integral, and derivative control actions to generate the output in the following manner:

$$\begin{cases} FLC_d = K_{pd} \varphi_{pd} + K_{id} \varphi_{id} + K_{dd} \varphi_{dd} \\ FLC_q = K_{pq} \varphi_{pq} + K_{iq} \varphi_{iq} + K_{dq} \varphi_{dq} \\ FLC_\Omega = K_{p\Omega} \varphi_{p\Omega} + K_{i\Omega} \varphi_{i\Omega} + K_{d\Omega} \varphi_{d\Omega} \end{cases} \tag{4.15}$$

where K_{pd}, K_{pq}, and $K_{p\Omega}$ are the gains of the proportional controller. K_{id}, K_{iq}, and $K_{i\Omega}$ are the gains of the integral controller. K_{dd}, K_{dq}, and $K_{d\Omega}$ are the gains of the derivative controller. φ_d, φ_q and φ_Ω are the outputs of the interval type 2 fuzzy logic control given by (4.18).

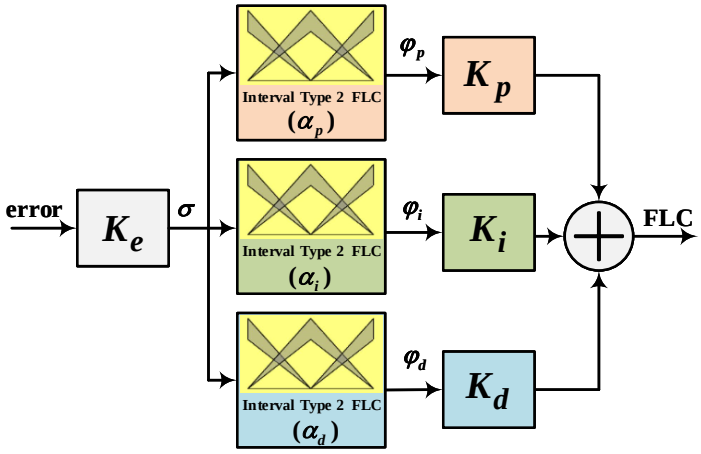

Figure 4.2: Structure of the IT2FLC.

To match the error signal input with the membership functions of the IT2FLC shown in Figure 4.3 [112], we normalize it to the interval of $[-1, 1]$ using the input scaling factor (K_e), as illustrated in Figure 4.2.

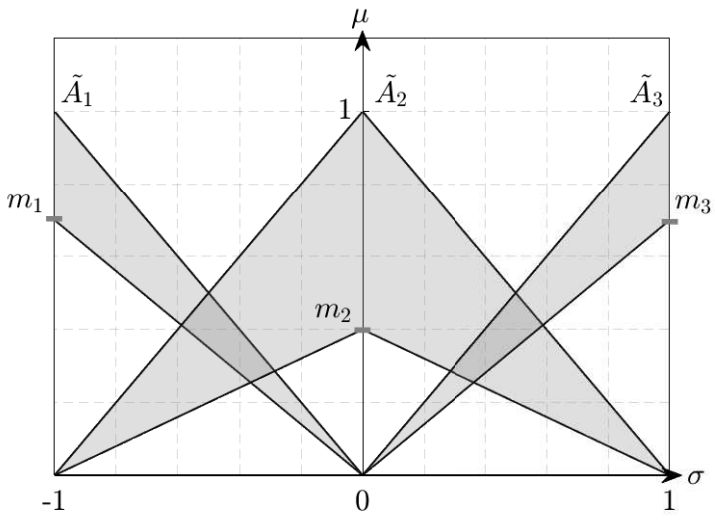

Figure 4.3: Membership functions.

The rule structure of the IT2FLC is defined as follows according to reference [8]:

$$R_i : \text{IF } \sigma \text{ is } \tilde{A}_i, \text{ THEN } \varphi \text{ is } B_i, \quad i = 1, 2, 3 \tag{4.16}$$

where B_i represents crisp outcomes with specific values assigned, such as $B_1 = -1$, $B_2 = 0$, and $B_3 = 1$. The heights of the lower membership functions, denoted as m_1, m_2, and m_3,

are delineated as:

$$\begin{cases} m_1 = m_3 = 1 - \alpha \\ m_2 = \alpha \end{cases} \tag{4.17}$$

Therefore, the sole parameter that requires tuning in the IT2FLC is α [8].

The expression detailing the fuzzy mapping of the single input IT2FLC, represented as $\varphi(\sigma)$, was introduced in reference [8]. It can be articulated as follows:

$$\varphi(\sigma) = \sigma k(|\sigma|) \tag{4.18}$$

where $k(\sigma)$ denotes the nonlinear gain, its definition is articulated as follows:

$$k(\sigma) = \frac{1}{2}\left(\frac{1}{\alpha + \sigma - \alpha\sigma} + \frac{\alpha - 1}{\alpha\sigma - 1}\right) \tag{4.19}$$

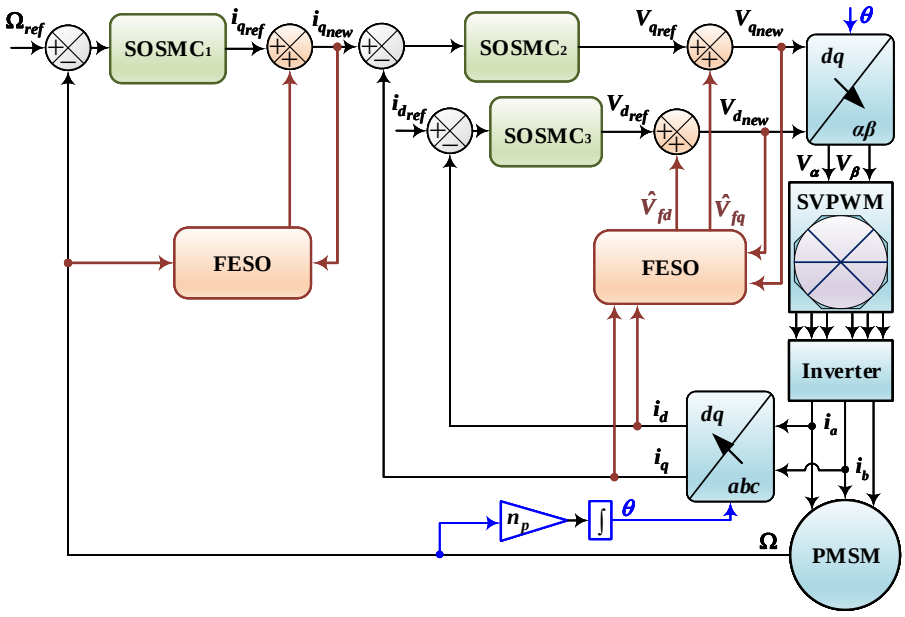

Figure 4.4: Structural diagram of the proposed FTC based on FESO.

4.5 Reconstruction Control

The active fault-tolerant control strategy is outlined in Figure 4.4, where new control laws from FESO are implemented to adjust the existing SOSMC laws. The reconstruction control

laws are depicted below:

$$\begin{cases} i_{q_{new}} = i_{q_{ref}} + \hat{i}_{fq} \\ V_{d_{new}} = V_{d_{ref}} + \hat{V}_{fd} \\ V_{q_{new}} = V_{q_{ref}} + \hat{V}_{fq} \end{cases} \tag{4.20}$$

where $i_{q_{ref}}$, $V_{q_{ref}}$, and $V_{d_{ref}}$ are the SOSMC laws given by (3.15), (3.16), and (3.17); respectively, the additional control laws $\hat{i}_{fq}$, $\hat{V}_{fd}$, and $\hat{V}_{fq}$ are determined by a FESO that estimates the impact of the fault and are defined as:

$$\begin{cases} \hat{i}_{fq} = -\dfrac{1}{c_3}\hat{f}_{\Omega} \\ \hat{V}_{fd} = -\dfrac{1}{\beta}\hat{f}_{d} \\ \hat{V}_{fq} = -\dfrac{1}{\beta}\hat{f}_{q} \end{cases} \tag{4.21}$$

where $\hat{f}_{\Omega}$, $\hat{f}_{q}$, and $\hat{f}_{d}$ are the fault estimates computed through (4.14) and (4.12).

4.6 Simulation Results

The structural diagram of SOSMC with FESO is depicted in Figure 4.4, and their parameters are detailed in Table A.2. The proposed control algorithm was implemented on a DSP board (TMS320F28069M), with the setup being identical to that depicted in Figure 3.3 of the previous chapter. The PI control and conventional SMC are consistent with those employed in the previous chapter. To assess the performance of SOSMC with FESO under faulty conditions, we examine three fault scenarios: Demagnetization Fault, Modeled Faults, and a Short-circuit Fault.

4.6.1 SPMSM Under Demagnetization Fault

The simulation of permanent-magnet demagnetization was carried out by altering the permanent-magnet amplitude (Φ_r) and the deviation angle (γ). As illustrated in Figure 4.5, the reference speed was 1500 rpm, while the load torque was 20 Nm. The amplitude of the permanent-magnet flux was 0.32 Wb at 0 s and 0.25 Wb at 0.5 s, while the deviation angle was 0 degrees at 0 s and 60 degrees at 0.3 s. The load torque changed from 20 Nm to 28.4 Nm at t = 1.5 s to evaluate the fault-tolerant control under demagnetization fault.

Figure 4.5 demonstrates that SOSMC remains powerful in both healthy and faulty conditions compared to PI control and traditional SMC. However, it still experiences fluctuations

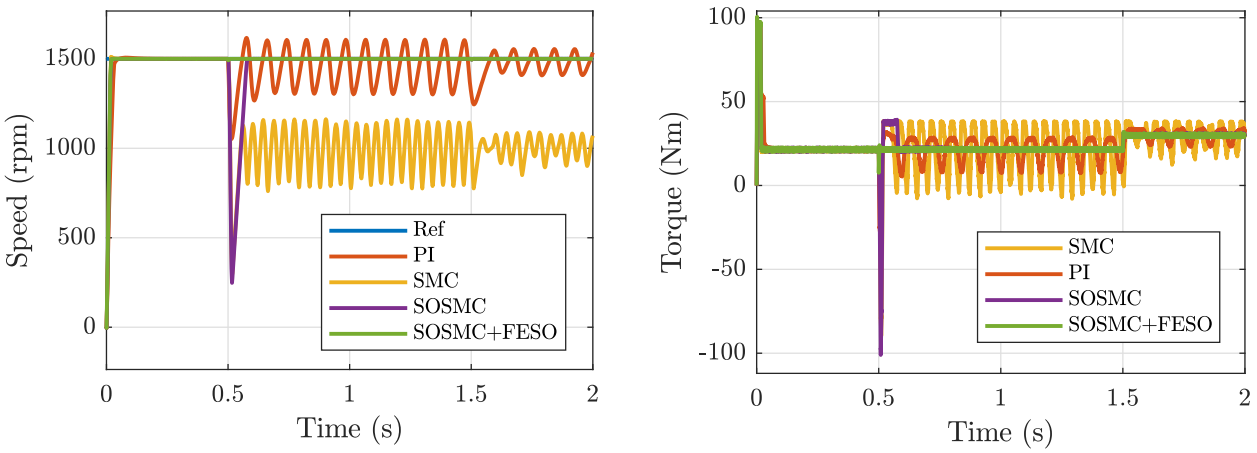

(a) Speed response.

(b) Torque response.

Figure 4.5: Speed and torque performance under demagnetization fault.

during transitions when a fault occurs. By boosting SOSMC with fuzzy extended state observer, the performance of SOSMC in handling permanent magnet demagnetization faults is improved. This enhancement provides strong robustness and compensates for uncertainties and faults.

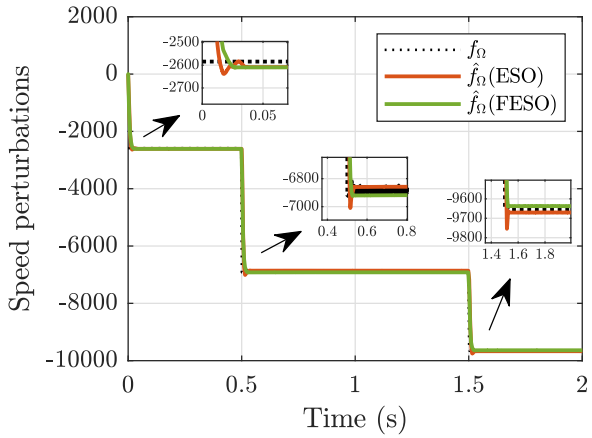

Figure 4.6: The estimated value of f_Ω.

Figure 4.6 and Figure 4.7 compare the simulation results of the traditional ESO and the FESO regarding their ability to estimate f_Ω, f_d, and f_q values. The traditional ESO exhibits oscillatory behavior in its estimate, while the FESO produces a smoother estimate. This indicates that the FESO can generate more stable and reliable estimates than its conventional counterpart when a demagnetization fault occurs. This finding highlights the robustness and effectiveness of the interval type 2 fuzzy logic-based approach in addressing the uncertainties

and nonlinearities inherent in the system. Mean square error values for the estimation data in Figure 4.6 and Figure 4.7 are presented in Table 4.1.

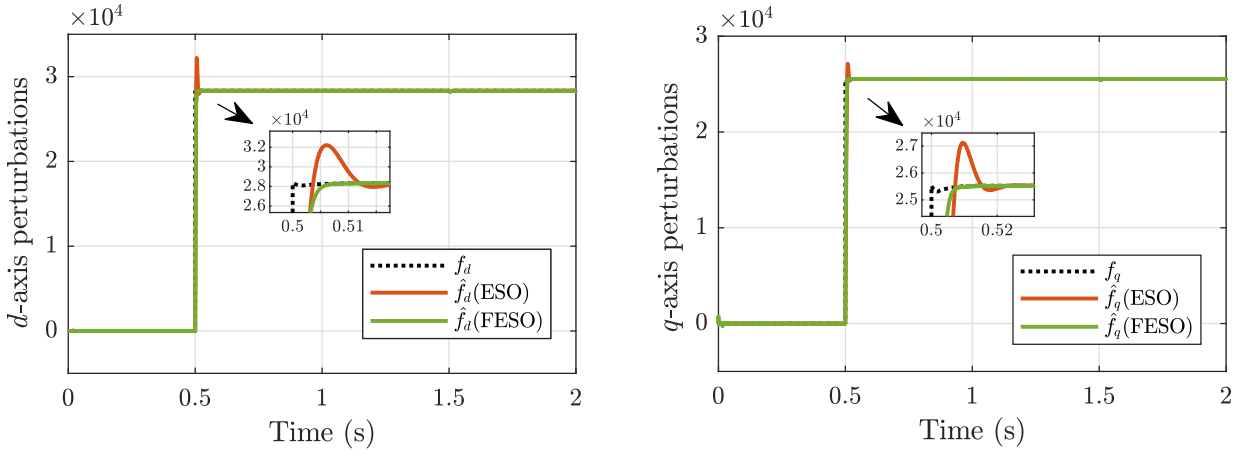

(a) Actual value and estimation in d-axis.

(b) Actual value and estimation in q-axis.

Figure 4.7: The estimated values of f_d and f_q.

Table 4.1: Comparison between traditional ESO and FESO

		ESO	FESO
Mean square error	$\hat{f}_\Omega$	300.8000	256.3508
	$\hat{f}_\mathrm{d}$	747.7654	655.8482
	$\hat{f}_\mathrm{q}$	771.2615	586.4111

4.6.2 SPMSM Under Modeled Faults

In the following modeled fault scenario, sinusoidal components are introduced into the currents, as shown in the dq-frame currents model (4.5). The speed and load torque are set to 1500 rpm and 28.4 Nm, respectively, as depicted in Figure 4.8.

- At time = 1 s, a single fault occurs and is modeled by a sinusoidal signal with the following characteristics: an amplitude (A_1) of 35, a frequency of 50 Hz, and a phase angle (θ_1) of $\pi/2$.
- At time = 1.5 s, two faults arise, each characterized by additional sinusoidal signals with amplitudes ($A_{2,3}$) of 5, frequencies of 80 Hz and 20 Hz, and phase angles ($\theta_{2,3}$) of $\pi/4$.

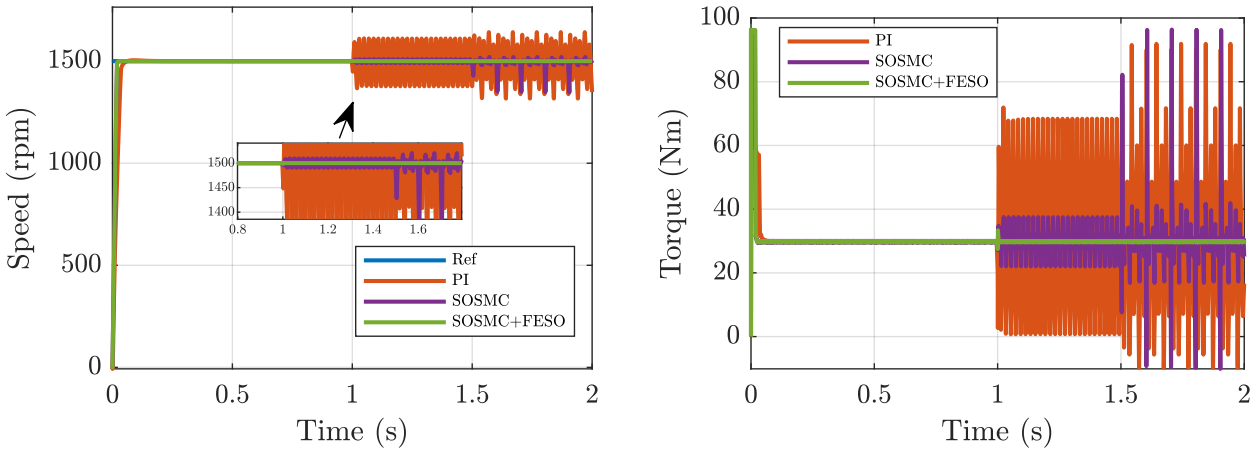

(a) Speed. (b) Torque.

Figure 4.8: Performance under modeled faults.

Figure 4.8 shows the speed and torque performance under modeled faults (one and two faults). At time = 1 s and time = 1.5 s, when the faults occur, both the PI and SOSMC controllers experience torque ripples and speed fluctuations. In contrast, the proposed fault-tolerant control based on SOSMC with FESO shows almost the same performance as in normal conditions.

4.6.3 SPMSM Under a Short-circuit Fault

The performance of the control under a short-circuit fault is shown in Figures 4.9 and 4.10. The speed and load torque are set at 1500 rpm and 28.4 Nm, respectively. At time = 1 s, a phase-to-phase short circuit between phase a and b suddenly occurs with a fault resistance of 0.0025 Ohm.

Figure 4.9 shows that PI and SOSMC controllers without FESO exhibit high ripples in speed and torque performances during the fault. In contrast, SOSMC with FESO maintains a stable and robust performance with minimal ripples.

Figure 4.10 illustrates that abc currents in PI and SOSMC controllers become unbalanced during short-circuit fault conditions. However, when FESO is used with SOSMC, the currents remain at the same level during fault conditions as they do under healthy conditions.

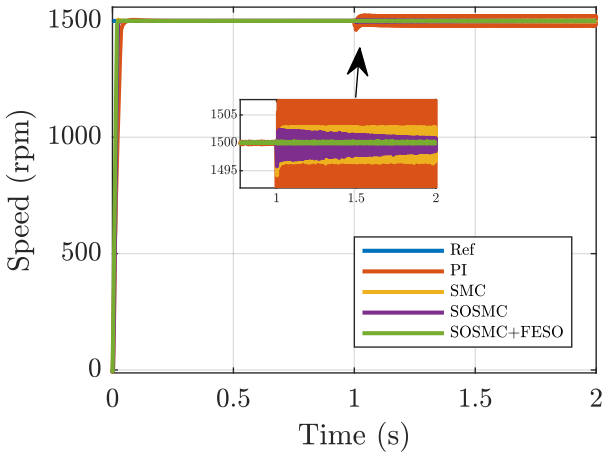

(a) Speed.

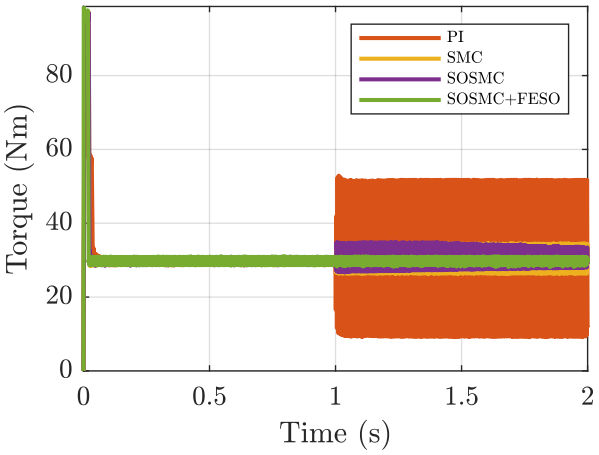

(b) Torque.

Figure 4.9: Performance under short-circuit fault.

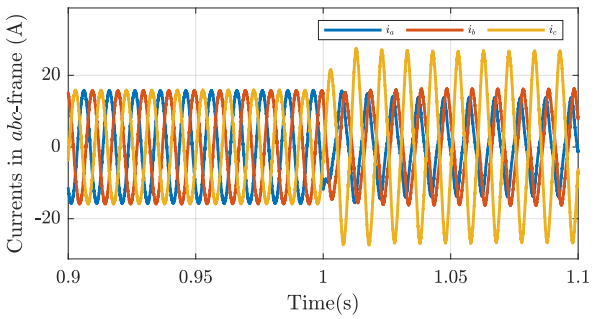

(a) PI control.

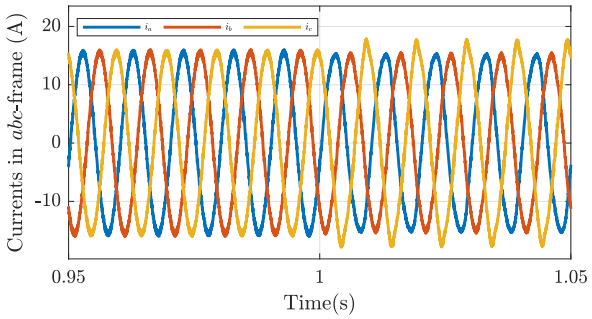

(b) SOSMC.

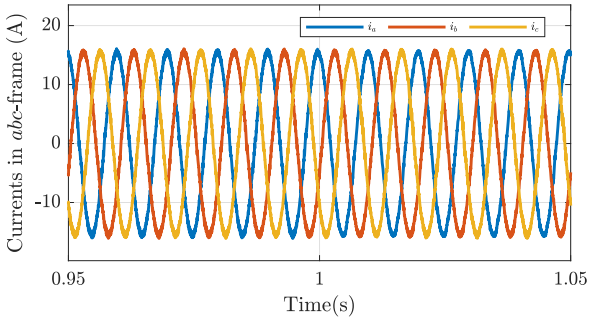

(c) SOSMC with FESO.

Figure 4.10: Performance of the currents in *abc*-frame under short-circuit fault.

4.7 Conclusion

In conclusion, this chapter has demonstrated that the combination of second-order sliding mode control (SOSMC) with a fuzzy extended state observer (FESO) yields efficient and robust dynamic performance for both speed and current controllers for a 3-phase PMSM. Through this combined approach, it exhibits adept handling of demagnetization and short-circuit faults, thereby ensuring the overall stability and control performance of a 3-phase PMSM. The incorporation of an interval type-2 fuzzy logic controller (IT2FLC) within the observer further amplifies the system's robustness, fortifying its resilience against both faults and external disturbances. The findings presented in this chapter underscore the efficacy of the proposed approach in addressing critical challenges within the PMSM system, thereby contributing to the advancement of fault-tolerant control strategies in the realm of electric motor applications.

Chapter 5

FTC of 5-phase PMSM

5.1 Introduction

Robustness is a vital feature of 5-phase permanent magnet synchronous motors (PMSMs), but they are still vulnerable to open-circuit faults (OCFs) that can affect their performance. OCFs are usually caused by faults or breaks in the motor windings [6], and they require quick detection and response to prevent further damage. Therefore, fault-tolerant control (FTC) strategies are essential to reduce the negative impacts of OCFs.

Many FTC strategies have been developed to deal with the unbalanced currents that result from OCFs in 5-phase PMSMs [113, 114, 115]. However, most of them are based on linear controllers, such as the PI controller, which is commonly used in field-oriented control. These linear controllers may not be able to handle the complexity and nonlinearity of 5-phase PMSMs during OCFs, which causes asymmetry in the motor and torque ripples. There is a need for more research on nonlinear control methods and compensations for multiphase machines under OCFs.

One of the nonlinear control methods that has attracted attention is sliding mode control (SMC), which has been shown to have advantages over linear methods [116]. SMC can cope with system uncertainties and disturbances, and it is less sensitive to model imperfections. This makes SMC a promising solution for PMSMs during fault conditions [117, 118]. SMC, despite its simplicity and tunability, has some challenges, such as the chattering effect, which need to be addressed by using mitigation methods, such as the reaching law approach. This approach includes techniques like constant rate reaching and power rate reaching, which can help reduce chattering effects in SMC [100]. However, there are also external disturbances that affect PMSMs, called mismatched disturbances, which pose additional challenges [119].

Traditional SMC techniques may not be able to fully compensate for these disturbances [120], which leads to the exploration of combining controllers with observers. The integration of a NESO with HTF and SMC is suggested as an effective strategy to handle mismatched disturbances.

The following sections of this chapter will explain the details of the proposed control strategy. Section 5.2 will describe the 5-phase PMSM model in healthy and faulty conditions, while Section 5.3 will discuss optimal control references for both models. Section 5.4 will present the design of an SMC with NESO, and Section 5.5 will analyze the results of the proposed approach. Finally, Section 5.6 will conclude the chapter, summarizing the contributions and implications of the research.

5.2 Dynamic Model of 5-phase PMSM Under an OCF

To facilitate the advancement of control laws for the 5-phase PMSM and enhance the understanding of its dynamic model, we can represent the motor model under healthy conditions by using (2.28) and (2.29) in the following manner:

$$\begin{cases} \dot{i}_{dp} = c_1 i_{dp} + c_2 \Omega i_{qp} + b_1 v_{dp} \\ \dot{i}_{qp} = c_3 i_{qp} - c_4 \Omega i_{dp} - c_5 \Omega + b_2 v_{qp} \\ \dot{i}_{ds} = c_6 i_{ds} + c_7 \Omega i_{qs} + b_3 v_{ds} \\ \dot{i}_{qs} = c_8 i_{qs} - c_9 \Omega i_{ds} - c_{10} \Omega + b_4 v_{qs} \\ \dot{\Omega} = a_1 T_e - a_1 T_L - a_2 \Omega \end{cases} \tag{5.1}$$

Wherein the machine parameters delineate the constituent components of the 5-phase PMSM model as follows:
$c_1 = -\frac{R_s}{L_{dp}}$, $c_2 = \frac{L_{qp}}{L_{dp}} n_p$, $c_3 = -\frac{R_s}{L_{qp}}$, $c_4 = \frac{L_{dp}}{L_{qp}} n_p$, $c_5 = \frac{\phi_{f1}}{L_{qp}} n_p$, $c_6 = -\frac{R_s}{L_{ds}}$, $c_7 = \frac{3L_{qs}}{L_{ds}} n_p$, $c_8 = -\frac{R_s}{L_{qs}}$, $c_9 = \frac{3L_{ds}}{L_{qs}} n_p$, $c_{10} = \frac{3\phi_{f3}}{L_{qs}} n_p$, $b_1 = \frac{1}{L_{dp}}$, $b_2 = \frac{1}{L_{qp}}$, $b_3 = \frac{1}{L_{ds}}$, $b_4 = \frac{1}{L_{qs}}$, $a_1 = \frac{1}{J}$, $a_2 = \frac{F}{J}$.

To enhance clarity, this chapter simplifies the fault model of 5-phase PMSM by focusing solely on the OCF during phase "a". In the event of an OCF, we can establish the new Clarke and Park transformation ((5.2), (5.3)). These transformations are designed to uphold the circular rotation of the fundamental magnetomotive force (MMF) and back-EMF, ensuring

their consistency with a healthy model [117].

$$T_{cf} = \frac{2}{5}\begin{bmatrix} \cos\frac{2\pi}{5}-1 & \cos\frac{4\pi}{5}-1 & \cos\frac{6\pi}{5}-1 & \cos\frac{8\pi}{5}-1 \\ \sin\frac{2\pi}{5} & \sin\frac{4\pi}{5} & \sin\frac{6\pi}{5} & \sin\frac{8\pi}{5} \\ \sin\frac{6\pi}{5} & \sin\frac{12\pi}{5} & \sin\frac{18\pi}{5} & \sin\frac{24\pi}{5} \\ 1 & 1 & 1 & 1 \end{bmatrix} \tag{5.2}$$

$$T_{pf} = \begin{bmatrix} \cos\theta & \sin\theta & 0 & 0 \\ -\sin\theta & \cos\theta & 0 & 0 \\ 0 & 0 & 1 & 0 \\ 0 & 0 & 0 & 1 \end{bmatrix} \tag{5.3}$$

Using ((5.2), (5.3)) and substituting the vector representing the flux linkage of a permanent magnet under an open circuit into the derivative of magnetic co-energy concerning the electrical angle, the expression for electromagnetic torque can be derived as described as follows [121]:

$$T_{ef} = T_{ef1} + T_{ef3} \tag{5.4}$$

$$T_{ef1} = \frac{5}{2}n_p\phi_{f1}i_{qp} + \frac{5}{2}n_p i_{dp}i_{qp}\left(L_{dp} - L_{qp}\right) \tag{5.5}$$

$$\begin{aligned} T_{ef3} = \frac{15}{4}n_p\phi_{f3}\,[&(-i_{qp}(\cos(2\theta) - \cos(4\theta)) \\ &+i_{dp}(\sin(2\theta) + \sin(4\theta)) + 2i_{\beta s}\cos(3\theta)] \end{aligned} \tag{5.6}$$

where T_{ef} denotes the total electromagnetic torque under faulty conditions, it is the sum of two components: T_{ef1} and T_{ef3}. T_{ef1} is the electromagnetic torque affected by the fundamental harmonic, which is equivalent to the healthy model. T_{ef3} is the electromagnetic torque that causes torque ripples due to the fault. The dynamic model of the 5-phase PMSM under the open circuit fault in phase "a" can be obtained as follows [121]:

$$\begin{cases} \dot{i}_{dp} = c_1 i_{dp} + c_2\Omega i_{qp} + b_1 v_{dp} \\ \dot{i}_{qp} = c_3 i_{qp} - c_4\Omega i_{dp} - c_5\Omega + b_2 v_{qp} \\ \dot{i}_{\beta s} = c_{11} i_{\beta s} - c_{12}\Omega\cos(3\theta) + b_{\beta s} v_{\beta s} \\ \dot{\Omega} = a_1 T_{ef} - a_1 T_L - a_2\Omega \end{cases} \tag{5.7}$$

where $c_{11} = -\frac{R_s}{L_{ls}}$, $c_{12} = \frac{3\phi_{f3}}{L_{ls}}n_p$, $b_{\beta s} = \frac{1}{L_{ls}}$, with θ representing the electrical angle and L_{ls} denoting the leakage inductance. The voltage ($v_{\beta s}$) and current ($i_{\beta s}$) in the β_s-axis are specified in the stationary frame $\alpha\beta_s$-frame, influenced by the third-order harmonic. It is noteworthy that the α_s-axis was eliminated during a single-phase open circuit in (5.2).

5.3 Optimal Control References

5.3.1 Current References in Healthy Model

To ensure optimal torque decoupling of the 5-phase PMSM during normal operating conditions, as outlined in Section 2.3, the current references for healthy conditions are:

$$\begin{cases} i_{dp}^{*} = 0 \\ i_{qp}^{*} = \dfrac{T_e^{*}}{k_T} \\ i_{ds}^{*} = 0 \\ i_{qs}^{*} = \varepsilon_3 i_{qp}^{*} \end{cases} \tag{5.8}$$

where $\varepsilon_3 = \frac{3\phi_{f3}}{\phi_{f1}}$ and $k_T = \frac{5}{2} n_p \phi_{f1}(1 + \varepsilon_3^2)$.

5.3.2 Current References in Faulty Model

To mitigate reluctance torque, it is essential to maintain the dp-axis current at zero, as this minimizes torque ripple resulting from the difference between the dp- and qp-axis inductances, as outlined in (5.4). Additionally, attention should be given to the current $i_{\beta s}$, which contributes to torque ripples associated with third-order torque pulsation. Determining the optimal $i_{\beta s}^{*}$ current reference is contingent upon specific control criteria, necessitating a choice between minimizing copper loss (MCL) and maximizing torque output (MTO).

5.3.2.1 MCL Control Criteria

To mitigate copper losses effectively, an optimal control strategy involves minimizing currents by driving as many of them to zero as feasible. Simultaneously, it aims to ensure the generation of the required output torque with the fewest possible currents, all while maintaining optimal performance.

When $i_{dp}^{*} = 0$, and $i_{\beta s}^{*} = 0$, the torque reference becomes simplified as:

$$T_{ef}^{*} = k_f i_{qp}^{*}(1 - 0.5\varepsilon_3 \cos(2\theta) + 0.5\varepsilon_3 \cos(4\theta)) \tag{5.9}$$

where $k_f = \frac{5}{2} n_p \phi_{f1}$. The torque reference in (5.9) assures MCL by raising the "c" and "d" phases by 26.31% and the "b" and "e" phases by 46.78% [118]. In accordance with the MCL

criteria, the currents references under faulty conditions are outlined as follows:

$$\begin{cases} i_{dp}^{*} = 0 \\ i_{qp}^{*} = \dfrac{T_{ef}^{*}}{k_f(1 - 0.5\varepsilon_3 \cos(2\theta) + 0.5\varepsilon_3 \cos(4\theta))} \\ i_{\beta s}^{*} = 0 \end{cases} \tag{5.10}$$

5.3.2.2 MTO Control Criteria

To optimize the inverter's output torque, it is essential to ensure the same amplitudes in the phase currents. Assuming a constant stator magnetomotive force, the authors proposed a strategy in [113]: once phase "a" is open-circuited, align the currents of the remaining phases by setting $i_b = -i_d$ and $i_c = -i_e$. Furthermore, from (5.2) and (5.3), we obtain:

$$\begin{aligned} i_{\beta p} &= \frac{2}{5}\left[(\sin\frac{2\pi}{5} - \sin\frac{6\pi}{5})i_b + (\sin\frac{4\pi}{5} - \sin\frac{8\pi}{5})i_c\right] \\ &= \frac{2}{5}(\sin\frac{2\pi}{5} - \sin\frac{6\pi}{5})(i_b + i_c) \end{aligned} \tag{5.11}$$

$$\begin{aligned} i_{\beta s} &= \frac{2}{5}\left[(\sin\frac{6\pi}{5} - \sin\frac{18\pi}{5})i_b + (\sin\frac{12\pi}{5} - \sin\frac{24\pi}{5})i_c\right] \\ &= \frac{2}{5}(\sin\frac{6\pi}{5} - \sin\frac{18\pi}{5})(i_b + i_c) \end{aligned} \tag{5.12}$$

Dividing (5.12) by (5.11) yields:

$$\begin{aligned} i_{\beta s} &= \frac{\sin\frac{6\pi}{5} - \sin\frac{18\pi}{5}}{\sin\frac{6\pi}{5} - \sin\frac{18\pi}{5}} i_{\beta p} = 0.236 i_{\beta p} \\ &= 0.236(-i_{dp}\sin\theta + i_{qp}\cos\theta) \end{aligned} \tag{5.13}$$

When $i_{dp}^{*} = 0$, the current reference in the β_s-axis is determined as follows:

$$i_{\beta s}^{*} = 0.236 i_{qp}^{*}\cos\theta \tag{5.14}$$

Therefore, substituting (5.14) into (5.4) yields:

$$T_{ef}^{*} = k_f i_{qp}^{*}(1 - 0.382\varepsilon_3\cos(2\theta) + 0.618\varepsilon_3\cos(4\theta)) \tag{5.15}$$

After applying the torque reference derived from MTO control criteria (5.15), the amplitudes of all phases should be equal and increased by 38.2%. To select the appropriate MTO control criteria, the current references under faulty conditions should be chosen as follows:

$$\begin{cases} i_{dp}^{*} = 0 \\ i_{qp}^{*} = \dfrac{T_{ef}^{*}}{k_f(1 - 0.382\varepsilon_3\cos(2\theta) + 0.618\varepsilon_3\cos(4\theta))} \\ i_{\beta s}^{*} = 0.236 i_{qp}^{*}\cos\theta \end{cases} \tag{5.16}$$

It is important to highlight that the torque references involve ε_3 multiplied by nonlinear terms, which cannot be eliminated due to the non-zero dependency of $\phi_{f3} \neq 0$ on the motor design. Consequently, we employ nonlinear controllers to effectively handle unmodeled motor dynamics, aiming to mitigate ripples in both torque and speed.

5.4 Design of SMC with NESO

5.4.1 Design of NESO

By considering the load and perturbation parameters as disturbance terms, we can rewrite the 5-phase PMSM model (5.1) as follows:

$$\begin{cases} \dot{i}_{dp} = f_{dp} + b_1 v_{dp} + d_1(t) \\ \dot{i}_{qp} = f_{qp} + b_2 v_{qp} + d_2(t) \\ \dot{i}_{ds} = f_{ds} + b_3 v_{ds} + d_3(t) \\ \dot{i}_{qs} = f_{qs} + b_4 v_{qs} + d_4(t) \\ \dot{\Omega} = a_1 T_e + d_5(t) \end{cases} \tag{5.17}$$

The faulty model (5.7) has the same current equations as the healthy model (5.1) for the dp-axis and the qp-axis, but the β_s-axis current equation is different and is given by:

$$\dot{i}_{\beta s} = f_{\beta s} + b_{\beta s} v_{\beta s} + d_6(t) \tag{5.18}$$

with:

$$\begin{aligned} f_{dp} &= c_1 i_{dp} + c_2 \Omega i_{qp}, \quad f_{qp} = c_3 i_{qp} - c_4 \Omega i_{dp} - c_5 \Omega \\ f_{ds} &= c_6 i_{ds} + c_7 \Omega i_{qs}, \quad f_{qs} = c_8 i_{qs} - c_9 \Omega i_{ds} - c_{10} \Omega \\ f_{\beta s} &= c_{11} i_{\beta s} - c_{12} \Omega \cos(3\theta) \end{aligned}$$

where $d_1(t)$, $d_2(t)$, $d_3(t)$ and $d_4(t)$ represent the mismatched disturbances of the stator currents in the d_p, q_p, d_s and q_s axes, respectively. Additionally, $d_5(t)$ signifies the mismatched disturbance for the speed, encompassing the load and viscous friction term. Furthermore, $d_6(t)$ characterizes the mismatched disturbance in the β_s-axis of the stator current during an OCF. It is assumed that $d_i(t)$ (where i ranges from 1 to 6) and their derivatives are bounded by:

$$\delta_i > \max(|d_i(t)|) \ , \ \rho_i > \max(|\dot{d}_i(t)|) \tag{5.19}$$

Consider the state equation of a nonlinear system, which can be expressed as follows:

$$\dot{x} = f(x,t) + bu + d(t) \tag{5.20}$$

where $f(x,t)$ denotes a nonlinear function of x, b is a positive constant, u represents the control input, and $d(t)$ signifies the bounded disturbance of the state.

To estimate the unknown disturbance $d(t)$ that affects the system (5.20), we propose a NESO that uses the Hyperbolic Tangent Function (HTF). The NESO has the following form:

$$\begin{cases} \dot{z}_1 = z_2 - h(z_1 - x) + f(x,t) + bu \\ \dot{z}_2 = -h^2 \tanh(z_1 - x) \end{cases} \tag{5.21}$$

where z_1 represents the estimate of x, z_2 represents the estimate of $d(t)$, and h is a positive design parameter.

The estimation errors, represented as $e_1 = z_1 - x$ and $e_2 = z_2 - d(t)$, arise from the asymptotically stable dynamics of errors centered around the equilibrium point. These errors are then converted into $\zeta_1 = e_1$ and $\zeta_2 = e_2 - he_1$. The evolution of this transformation can be elucidated by examining the dynamics of the system (5.20) and the ESO (5.21), as outlined below:

$$\begin{cases} \dot{\zeta}_1 = \zeta_2 \\ \dot{\zeta}_2 = \dot{e}_2 - h\zeta_2 = -h^2 \tanh(\zeta_1) - \eta - h\zeta_2 \end{cases} \tag{5.22}$$

where $\eta = \dot{d}(t)$.

The proposed Lyapunov function is outlined as follows:

$$V_\zeta = h^2 \int_0^{\zeta_1} \tanh(\zeta_1) d\zeta_1 + \frac{1}{2}\zeta_2^2 \tag{5.23}$$

Using (5.22), we can obtain the following expression for the derivative of the Lyapunov function:

$$\begin{aligned} \dot{V}_\zeta &= \frac{\partial V_\zeta}{\partial \zeta_1}\dot{\zeta}_1 + \frac{\partial V_\zeta}{\partial \zeta_2}\dot{\zeta}_2 \\ &= h^2 \tanh(\zeta_1)\zeta_2 + \zeta_2(-h^2 \tanh(\zeta_1) - \eta - h\zeta_2) \\ &= -\zeta_2(\eta + h\zeta_2) \end{aligned} \tag{5.24}$$

If η equals zero ($\eta = 0$), then $\dot{V}_\zeta = -h\zeta_2^2 \leq 0$. Despite the derivative being zero, the stability of the Lyapunov function is preserved, thanks to its construction based on the system (5.22). In cases where η is non-zero ($\eta \neq 0$), and assuming that the norm of η ($||\eta||$) is less than or equal to ρ, the steady state of system (5.22) can be expressed as follows:

$$\begin{cases} \dot{\zeta}_1 = \zeta_2 = 0 \\ \dot{\zeta}_2 = -h^2 \tanh(\zeta_1) - \eta - h\zeta_2 = 0 \end{cases} \tag{5.25}$$

Given the monotonically increasing nature of the HTF, we can infer from (5.25) that taking the absolute value of $\tanh(z_1 - x_1)$ with its bound, specifically $|\tanh(z_1 - x_1)| \leq \frac{\rho}{h^2}$.

This bound plays a crucial role in guaranteeing that the estimation errors of the ESO adhere to the following conditions:

$$|z_1 - x_1| \leq \tanh^{-1}(\frac{\rho}{h^2}), \qquad |z_2 - d(t)| \leq h\tanh^{-1}(\frac{\rho}{h^2}) \tag{5.26}$$

By carefully choosing a suitable parameter $h > 0$, the estimation errors, denoted as e_1 (where $e_1 = z_1 - x$) and e_2 (where $e_2 = z_2 - d(t)$), will gradually converge to a close proximity of zero.

We define x, u, z_1, and z_2 as the corresponding states of the 5-phase PMSM model according to (5.21). Then, we can derive the equations of the NESO to estimate the mismatched disturbance as follows:

- The estimation of $d_1(t)$ can be determined through:

$$\begin{cases} \dot{\hat{i}}_{dp} = \hat{d}_1(t) - h_1(\hat{i}_{dp} - i_{dp}) + f_{dp} + b_1 v_{dp} \\ \dot{\hat{d}}_1(t) = -h_1^2 \tanh(\hat{i}_{dp} - i_{dp}) \end{cases} \tag{5.27}$$

- The estimation of $d_2(t)$ can be determined through:

$$\begin{cases} \dot{\hat{i}}_{qp} = \hat{d}_2(t) - h_2(\hat{i}_{qp} - i_{qp}) + f_{qp} + b_2 v_{qp} \\ \dot{\hat{d}}_2(t) = -h_2^2 \tanh(\hat{i}_{qp} - i_{qp}) \end{cases} \tag{5.28}$$

- The estimation of $d_3(t)$ can be determined through:

$$\begin{cases} \dot{\hat{i}}_{ds} = \hat{d}_3(t) - h_3(\hat{i}_{ds} - i_{ds}) + f_{ds} + b_3 v_{ds} \\ \dot{\hat{d}}_3(t) = -h_3^2 \tanh(\hat{i}_{ds} - i_{ds}) \end{cases} \tag{5.29}$$

- The estimation of $d_4(t)$ can be determined through:

$$\begin{cases} \dot{\hat{i}}_{qs} = \hat{d}_4(t) - h_4(\hat{i}_{qs} - i_{qs}) + f_{qs} + b_4 v_4 \\ \dot{\hat{d}}_4(t) = -h_4^2 \tanh(\hat{i}_{qs} - i_{qs}) \end{cases} \tag{5.30}$$

- The estimation of $d_5(t)$ can be determined through:

$$\begin{cases} \dot{\hat{\Omega}} = \hat{d}_5(t) - h_5(\hat{\Omega} - \Omega) + a_1 T_e \\ \dot{\hat{d}}_5(t) = -h_5^2 \tanh(\hat{\Omega} - \Omega) \end{cases} \tag{5.31}$$

- The estimation of $d_6(t)$ can be determined through:

$$\begin{cases} \dot{\hat{i}}_{\beta s} = \hat{d}_6(t) - h_6(\hat{i}_{\beta s} - i_{\beta s}) + f_{\beta s} + b_{\beta s} v_{\beta s} \\ \dot{\hat{d}}_6(t) = -h_6^2 \tanh(\hat{i}_{\beta s} - i_{\beta s}) \end{cases} \tag{5.32}$$

where h_i denotes a positive constant gain of the observer for each i from 1 to 6.

5.4.2 Design of SMC

In this chapter, we explore an approach that integrates proportional rate reaching and power rate reaching to enhance the speed of reaching the sliding surface, as discussed in [100]. This combined approach aims to demonstrate improved efficacy in accelerating the reaching process and is articulated as follows:

$$\begin{cases} \dot{s} = -k|s|^{\alpha}\text{sign}(s) - ms \\ 0 < \alpha < 1, k > 0, m > 0 \end{cases} \tag{5.33}$$

where s represents the sliding surface, the design parameters α, k, and m adhere to the conditions outlined in the preceding equation.

We designate the sliding surfaces for the six controllers as follows:

$$\begin{cases} s_1 = \hat{i}_{dp} - i^*_{dp} \\ s_2 = \hat{i}_{qp} - i^*_{qp} \\ s_3 = \hat{i}_{ds} - i^*_{ds} \\ s_4 = \hat{i}_{qs} - i^*_{qs} \\ s_5 = \hat{\Omega} - \Omega^* \\ s_6 = \hat{i}_{\beta s} - i^*_{\beta s} \end{cases} \tag{5.34}$$

where the reference state is represented by the symbol "*" and the estimated state of the NESO is denoted by the symbol "$\hat{}$".

In accordance with (5.33) and (5.34), the discontinuous control law for controllers is expressed as follows:

$$\begin{cases} u_i = -k_i|s_i|^{\alpha_i}\text{sign}(s_i) - m_i s_i \\ i = 1, \ldots, 6 \end{cases} \tag{5.35}$$

where each of the parameters α_i, k_i, and m_i (for $i = 1$ to 6) represents a positive design constant.

The following control laws are obtained by combining the discontinuous control laws (5.35) with the equivalent control laws, which are derived by setting the sliding surfaces derivative

to zero:

$$\begin{cases} v_{dp}^{*} = \dfrac{1}{b_1}(-\hat{f}_{dp} - \hat{d}_1(t) + \dot{i}_{dp}^{*}) + u_1 \\ v_{qp}^{*} = \dfrac{1}{b_2}(-\hat{f}_{qp} - \hat{d}_2(t) + \dot{i}_{qp}^{*}) + u_2 \\ v_{ds}^{*} = \dfrac{1}{b_3}(-\hat{f}_{ds} - \hat{d}_3(t) + \dot{i}_{ds}^{*}) + u_3 \\ v_{qs}^{*} = \dfrac{1}{b_4}(-\hat{f}_{qs} - \hat{d}_4(t) + \dot{i}_{qs}^{*}) + u_4 \\ T_e^{*} = \dfrac{1}{a_1}(-\hat{d}_5(t) + \dot{\Omega}^{*}) + u_5 \\ v_{\beta s}^{*} = \dfrac{1}{b_{\beta s}}(-\hat{f}_{\beta s} - \hat{d}_6(t) + \dot{i}_{\beta s}^{*}) + u_6 \end{cases} \tag{5.36}$$

with:

$$\begin{aligned} &\hat{f}_{dp} = c_1\hat{\dot{i}}_{dp} + c_2\hat{\Omega}\hat{i}_{qp}, \quad \hat{f}_{qp} = c_3\hat{\dot{i}}_{qp} - c_4\hat{\Omega}\hat{i}_{dp} - c_5\hat{\Omega} \\ &\hat{f}_{ds} = c_6\hat{\dot{i}}_{ds} + c_7\hat{\Omega}\hat{i}_{qs}, \quad \hat{f}_{qs} = c_8\hat{\dot{i}}_{qs} - c_9\hat{\Omega}\hat{i}_{ds} - c_{10}\hat{\Omega} \\ &\hat{f}_{\beta s} = c_{11}\hat{\dot{i}}_{\beta s} - c_{12}\hat{\Omega}\cos(3\theta) \end{aligned}$$

where $\hat{d}_i(t)$ (for $i = 1$ to 6) denotes the estimated disturbances of the nonlinear extended state observer (NESO).

A Lyapunov function can be defined in the following manner:

$$V = \frac{1}{2}(\sum_{i=1}^{6} s_i^2) \tag{5.37}$$

The derivative of the Lyapunov function yields:

$$\begin{aligned} \dot{V} &= \sum_{i=1}^{6}(-\frac{k_i}{b_i}|s_i|^{\alpha_i}\text{sign}(s_i) - \frac{m_i}{b_i}s_i)s_i \\ &= \left(\sum_{i=1}^{6}(-A_i|s_i|^{\alpha_i}|s_i| - B_i s_i^2)\right) \leq 0 \end{aligned} \tag{5.38}$$

where A_i is defined as $\frac{k_i}{b_i}$ and B_i is defined as $\frac{m_i}{b_i}$, achieving stability with $\dot{V} \leq 0$ necessitates meeting the conditions of $A_i > 0$, $B_i > 0$, and $0 < a_i < 1$.

5.5 Simulation Results

To validate the proposed control strategy for the 5-phase PMSM under both healthy and faulty conditions, we conducted comprehensive experiments utilizing MATLAB/Simulink. The structural diagrams illustrating the control strategy for each scenario are presented in Figures 5.1 and 5.2. Detailed motor drive parameters can be found in A.3.

For the experimental implementation, we executed the proposed control algorithm on a DSP board (TMS320F28069M), which generated PWM signals. These PWM signals were employed to control a 5-phase Voltage Source Inverter (VSI) responsible for supplying power to 5-phase PMSM. The VSI and 5-phase PMSM models were meticulously constructed using Simulink, and simulations were conducted with a fixed step size of $1 \times 10^{-6} s$. To facilitate the control of the five-phase motor, particularly under OCF conditions, we adopted the CPWM technique due to its simplicity, ease of implementation, and its ability to inject zero-sequence signals into the modulation signals.

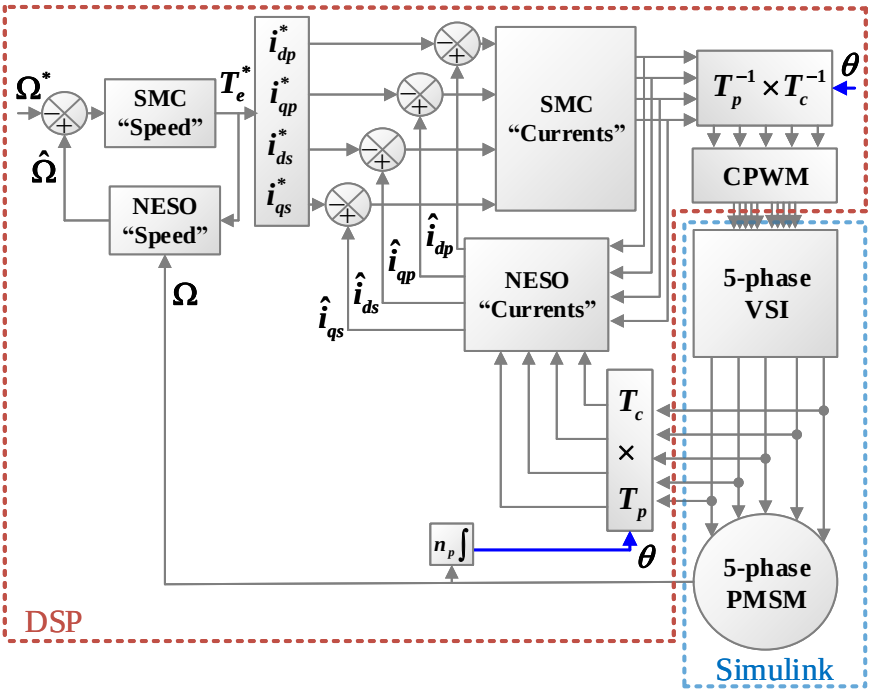

Figure 5.1: Control structure in healthy conditions.

The motor we studied has a trapezoidal back-EMF, which means that it has a significant third harmonic component. We can see the back-EMF of each of the five phases in Figure 5.3. We used a fast Fourier transform (FFT) analysis to quantify the third harmonic component, and we found that it accounted for 19.92% of the total back-EMF spectrum. To test the performance of the proposed SMC with NESO for 5-phase PMSMs, we conducted experiments under both healthy and faulty conditions and compared the results.

To compare the performance of the proposed control method for 5-phase PMSMs, we used two benchmark methods: PI control and traditional sliding mode control (TSMC). These methods are widely used in the literature for 5-phase PMSMs. Our implementation of TSMC was a hybrid strategy amalgamating techniques outlined in [117] and [118]. The first

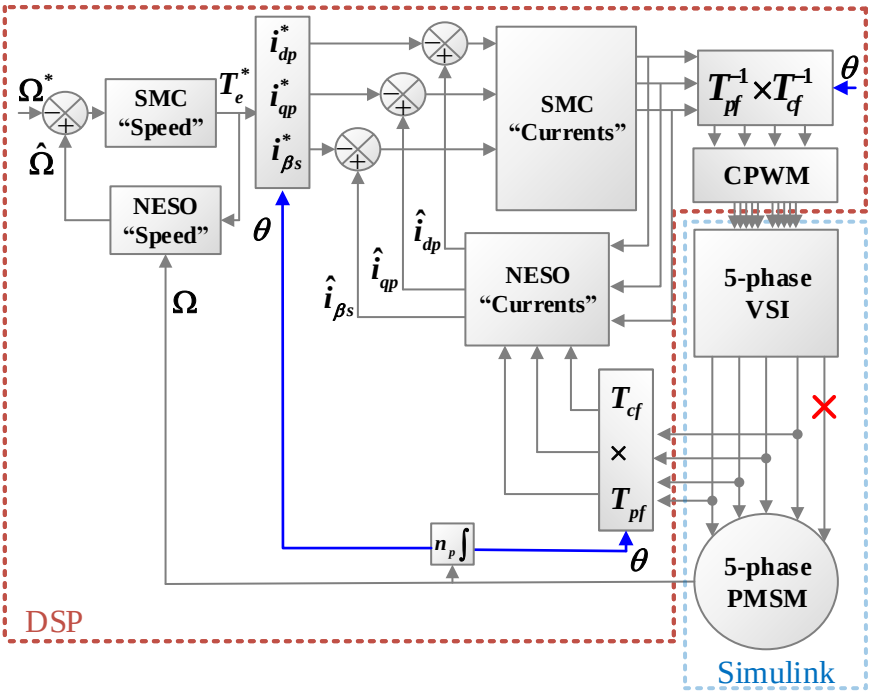

Figure 5.2: Control structure in faulty conditions.

technique [117] incorporated TSMC with a PI controller and a chattering term within the speed loop, while the second technique [118] applied TSMC specifically in the current control loops. To assess the torque and speed performance under different conditions, we used two indicators of torque ripples and speed fluctuations, as defined in (5.39).

$$\begin{cases} T_{e_{ripple}}\% = \dfrac{(\max(T_e) - \min(T_e))}{\text{mean}(T_e)} \times 100 \\ \Omega_{fluc}\% = \dfrac{(\max(\Omega) - \min(\Omega))}{\text{mean}(\Omega)} \times 100 \end{cases} \tag{5.39}$$

5.5.1 Healthy Conditions

To demonstrate the robustness of the proposed SMC with NESO under healthy conditions, we planned to examine the influence of uncertainties in the stator resistance parameters and sinusoidal variations in unmodeled dynamics. The mismatched disturbances, as described in (5.17), will be applied in the following manner:

$$\begin{cases} d_1(t) = -\frac{\Delta R_s}{L_{dp}} + \delta_{dp} \\ d_2(t) = -\frac{\Delta R_s}{L_{qp}} + \delta_{qp} \\ d_3(t) = -\frac{\Delta R_s}{L_{ds}} + \delta_{ds} \\ d_4(t) = -\frac{\Delta R_s}{L_{qs}} + \delta_{qs} \end{cases} \tag{5.40}$$

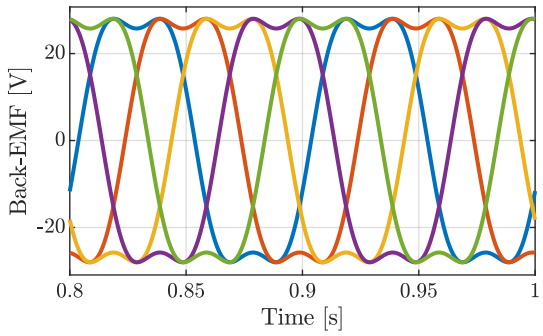

Figure 5.3: Five-phase back-EMF in healthy.

where ΔR_s is defined as the absolute difference between R_s and R_{sn}, with R_{sn} representing the nominal value of the stator resistance. The terms δ_{dp}, δ_{qp}, δ_{ds}, and δ_{qs} are employed to denote unmodeled dynamics, and their characterization involves sinusoidal forms to accommodate dead-time effects, as outlined in [81].

To evaluate the proposed control, we performed a comparative analysis with TSMC and PI control under different conditions of load torque and speed reference. We tested the controllers in two situations: one with fixed speed reference and varying load torque, and another with fixed load torque and varying speed reference. Moreover, we examined the effects of parameter uncertainties and sinusoidal variations in unmodeled dynamics in both situations.

Figures 5.4a and 5.4b depict the outcomes of the first situation, wherein the speed reference is established at 300 rpm, and the load torque undergoes a shift from 20 Nm to 40 Nm at 1 second. Additional unmodeled dynamics are introduced at 2 seconds, denoted as $\delta_{dp} = 10\sin(6\theta)$ and $\delta_{qp} = 10\cos(6\theta)$. Concurrently, the stator resistance experiences a $+60\%R_s$ adjustment, equivalent to $1.6R_{sn}$. The findings reveal that all three methodologies successfully follow the speed reference despite variations in load torque and the presence of mismatched disturbances. Nonetheless, it is observed that the PI control exhibits the slowest settling time, characterized by overshoot and heightened speed fluctuations. The TSMC demonstrates a faster settling time compared to PI control, yet both methods display discernible ripples in the speed and torque responses at 2 seconds, indicating limited robustness and control performance in the face of disturbances. In contrast, the proposed SMC with NESO effectively mitigates the impact of parameter uncertainties and unmodeled dynamics. This ensures smooth tracking of the speed reference with the quickest settling time and minimal ripples or fluctuations in speed and torque, even under sudden load torque changes.

In the second situation, illustrated in Figures 5.4c and 5.4d, where the load torque is set at

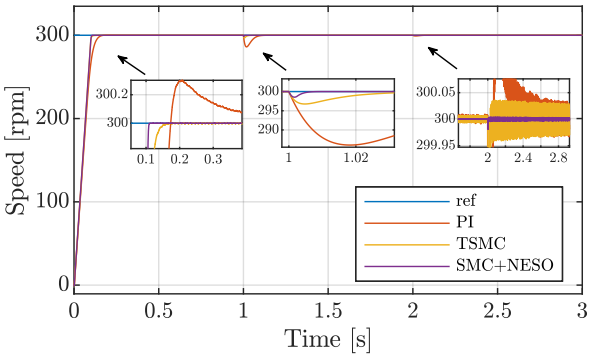

(a) Speed response to load changes.

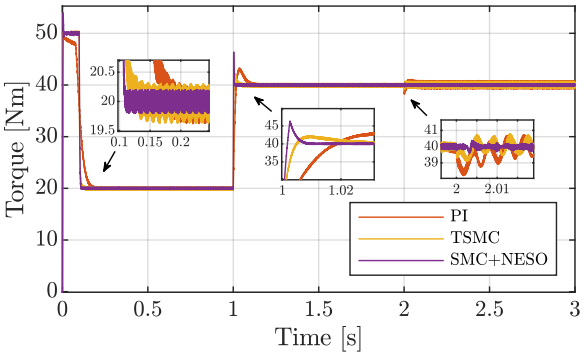

(b) Torque response to load changes.

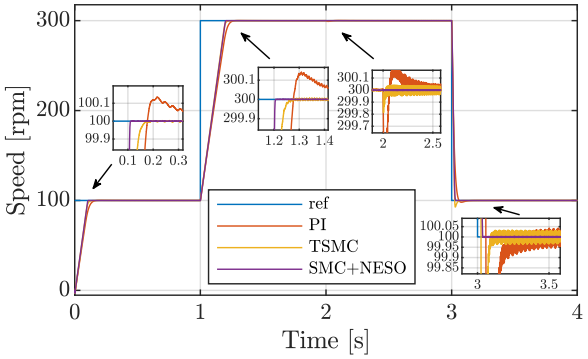

(c) Speed response to speed changes.

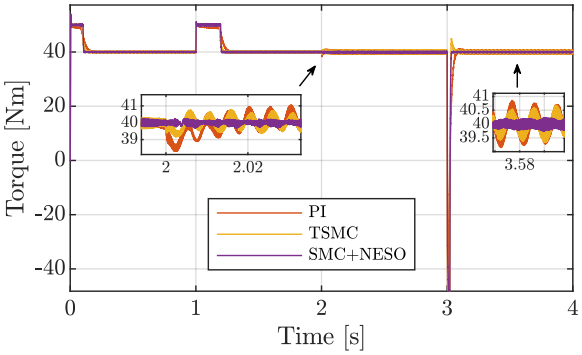

(d) Torque response to speed changes.

Figure 5.4: Healthy conditions response to load and speed changes.

40 Nm, and the speed reference undergoes an abrupt step change from 100 rpm to 300 rpm, reverting to 100 rpm at 3 seconds. Unmodeled dynamics and parameter uncertainty, akin to the first situation, are introduced at 2 seconds. In this context, the proposed control outperforms both PI control and TSMC, exhibiting more accurate tracking of the reference speed, a shorter settling time, absence of overshoot, and reduced torque ripples. This underscores the superior performance of the proposed SMC with NESO in effectively managing mismatched disturbances during abrupt changes in speed reference, ensuring robust and efficient control.

5.5.2 Faulty Conditions

We examined how the proposed SMC with NESO, PI control, and TSMC performed under faulty conditions by studying the effect of an OCF in phase "a" on a 5-phase PMSM that used an MCL control strategy. Figure 5.1 illustrates the healthy structure, while Figure 5.2 shows the fault-tolerant mode when the OCF was detected. We analyzed how this fault in phase "a" affected the speed, torque, and current responses (see Fig. 5.5). The fault happened at 1 second when the motor was running at a speed reference of 200 rpm and a load torque

of 20 Nm. The fault detection happened at 1.5 seconds, which caused a quick switch to the fault-tolerant mode. A noticeable irregularity in the current response was observed between 1 and 1.5 seconds before the fault detection (see Fig. 5.5c). After the fault detection, the current response showed differences in amplitudes of phases, with a rise of 26.31% for phases "c" and "d" and 46.78% for phases "b" and "e", as shown in Figure 5.5d. The proposed SMC with NESO made a smooth transition between the healthy and faulty conditions. On the other hand, both PI control and TSMC displayed significant oscillations and ripples in speed and torque, persisting even after fault detection (see Figs. 5.5a and 5.5b).

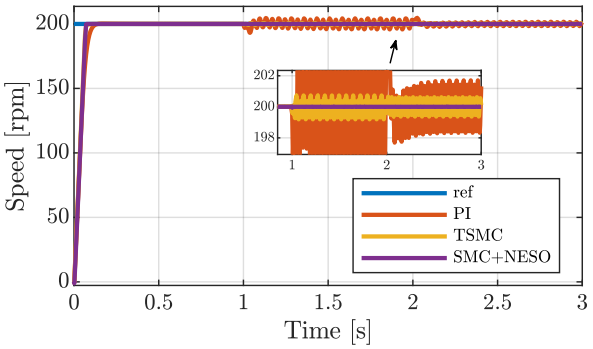

(a) Speed response.

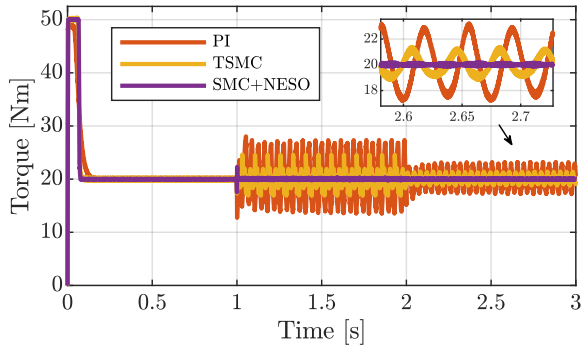

(b) Torque response.

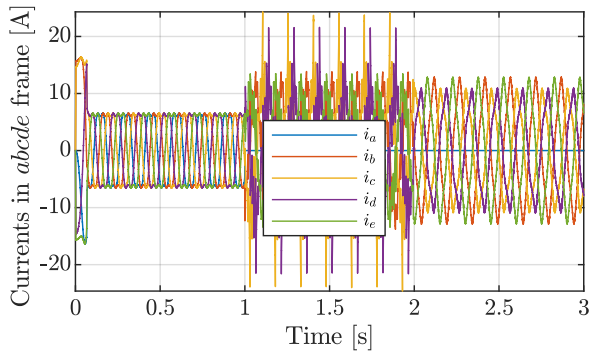

(c) Currents response in *abcde* frame.

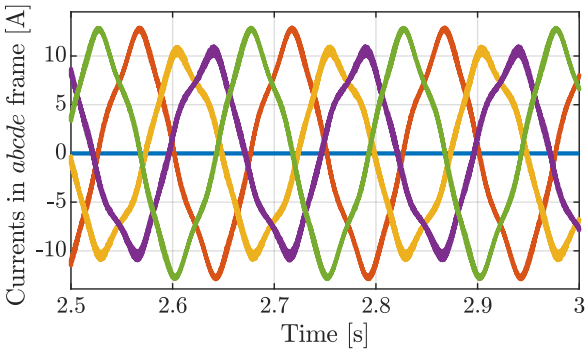

(d) Currents Response Zoom.

Figure 5.5: Response by using MCL under OCF.

To assess the optimal control references for the proposed SMC with NESO, PI control, and TSMC under an OCF in phase "a", we established a speed reference of 300 rpm and a load torque of 40 Nm. When applying the MCL criterion, the torque ripples of the PI control and TSMC are less at the wave peak than those of the MTO criterion, as depicted in Figures 5.6a and 5.6b. However, the suggested SMC with NESO showed nearly identical, minor torque ripples for both criteria (see Fig. 5.6c). On the other hand, the MCL criteria control results in unequal amplitude currents, while the MTO criteria control ensures that all

phase currents are equal. Nevertheless, they increased by 38.2% from the healthy conditions due to the application of MTO control criteria, as shown in Figure 5.6d. A comparative analysis between PI control, TSMC, and the proposed SMC with NESO using the MTO and MCL criteria in the steady state is provided in Table A.4. The findings reveal that SMC with NESO has the smallest torque ripple difference between the MTO and MCL criteria (around 0.593%), followed by TSMC (3.4042%), and PI control (6.4322%).

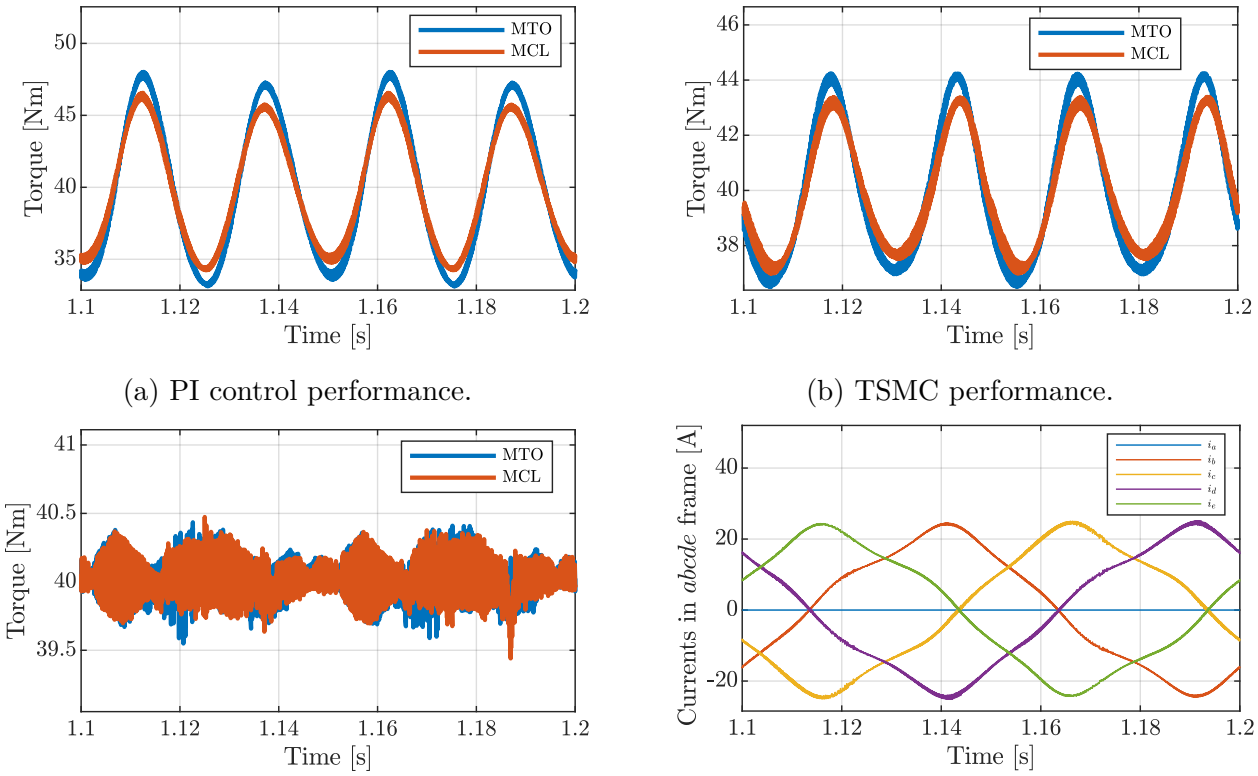

(a) PI control performance.

(b) TSMC performance.

(c) SMC+NESO performance.

(d) SMC+NESO performance (MTO).

Figure 5.6: Response by using MCL and MTO under OCF.

To evaluate the robustness of the proposed SMC with NESO in the presence of faulty conditions, we conducted an examination of the consequences arising from uncertainties in parameters by changing the stator resistance. The mismatched disturbances outlined in equations (5.17) and (5.18) will be characterized in the following manner:

$$\begin{cases} d_1(t) = -\frac{\Delta R_s}{L_{dp}} \\ d_2(t) = -\frac{\Delta R_s}{L_{qp}} \\ d_6(t) = -\frac{\Delta R_s}{L_{ls}} \end{cases} \tag{5.41}$$

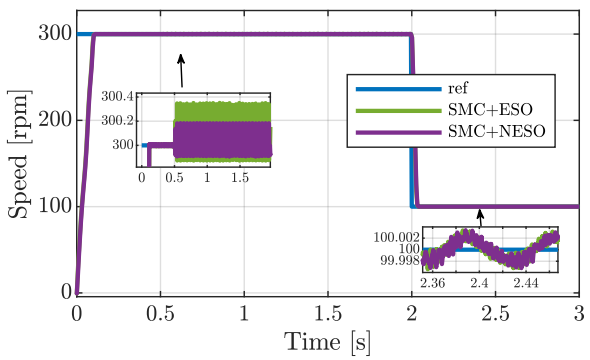

(a) Speed response.

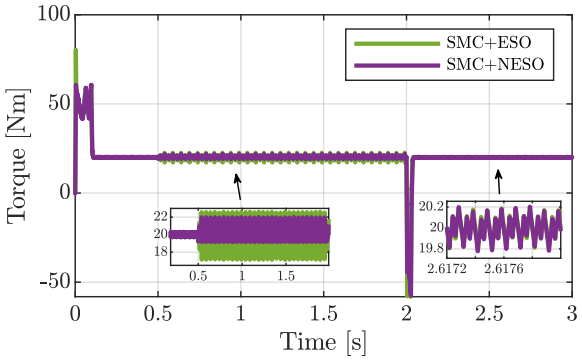

(b) Torque response.

Figure 5.7: Response to parameter uncertainty under OCF.

The results compared two different control scenarios: one that used the proposed SMC with a NESO that included the HTF, and another that applied an ESO without the HTF. The speed reference was 300 rpm, the load torque was 20 Nm, and the stator resistance was changed to 1.6 times R_{sn} (+60% of Rs) at 0.5 seconds. In Figure 5.8, the stator current waveform of phase "d" and its corresponding Fast Fourier Transform (FFT) spectra in steady state are presented. The findings reveal that the control scheme without HTF exhibits a higher Total Harmonic Distortion (THD) of 35.75% compared to the utilization of HTF, which resulted in a THD of 24.08%. Specifically, for the 3rd harmonic, the reduction was from 17.7% to 12.15%; for the 5th harmonic it decreased from 10.44% to 9.092%; for the 7th harmonic, it reduced from 17.48% to 11.17%; and for the 9th harmonic, it decreased from 11.8% to 7.176%. The speed and torque response are shown in Figure 5.7. The figure reveals that the stator resistance variation at 0.5 seconds caused more noticeable ripples in speed and torque for the control without HTF than for the control with HTF. However, when the speed reference changed to 100 rpm at 2 seconds, the speed and torque oscillations were almost the same for both cases. Thus, the incorporation of HTF in the proposed control strategy effectively alleviates harmonics in the current signal and reduces ripples in the speed and torque performance.

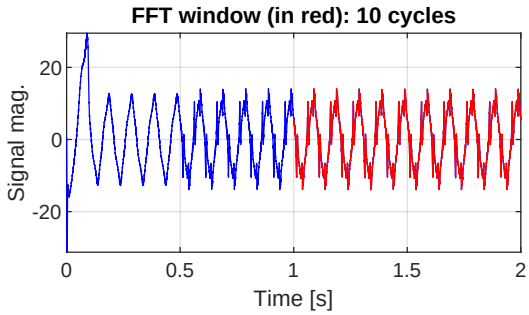

(a) Current response (SMC+ESO).

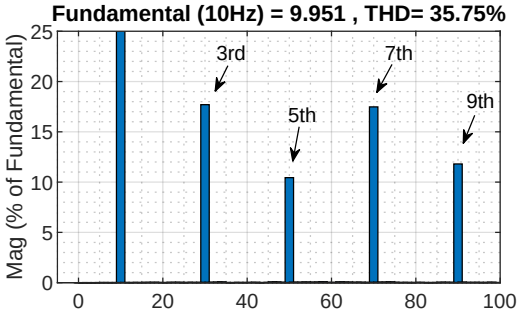

(b) Current THD (SMC+ESO).

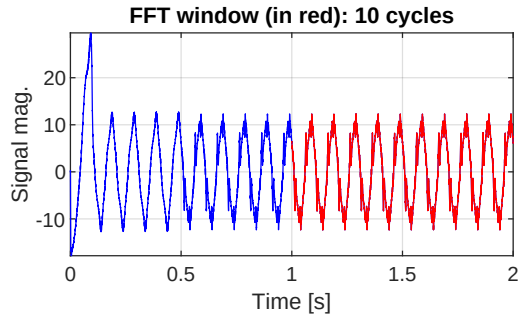

(c) Current response (SMC+NESO).

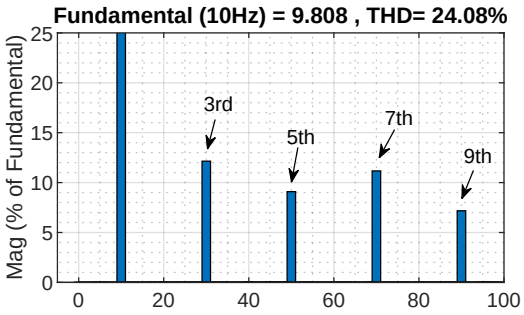

(d) Current THD (SMC+NESO).

Figure 5.8: Response to parameter uncertainty under OCF.

5.6 Conclusion

In conclusion, this chapter introduced a FTC strategy tailored for a trapezoidal back-EMF 5-phase PMSM operating under an open-circuit fault. The proposed strategy harnessed SMC with NESO based on the hyperbolic tangent function, and its stability was validated through the application of the Lyapunov theory. Furthermore, optimal current references were presented using FOC to achieve torque decoupling and minimize copper losses in healthy operating conditions. In the event of faults, two distinct criteria for optimal current references were introduced: MCL and MTO. The comparative analysis demonstrated that the proposed control exhibited minimal torque ripples for both criteria, distinguishing it from conventional PI control and TSMC methods. Additionally, the efficacy of the proposed control was verified in terms of enhanced tracking accuracy and robustness to disturbances, showcasing notable reductions in torque ripples and speed fluctuations under faulty conditions. This research contributes valuable insights into the development of fault-tolerant control strategies for PMSMs, emphasizing the significance of the proposed approach in mitigating the impact of faults and improving overall motor system performance.

General Conclusion

In this thesis, a comprehensive exploration of fault-tolerant control (FTC) strategies for electrical motor systems has been presented. The initial chapter laid the foundation by introducing the concepts of FTC and the analysis of faults in electrical motors, emphasizing the importance of early detection and appropriate control strategies to mitigate the impact of faults on motor performance and reliability.

Chapter 2 presented a comprehensive overview of modeling and FOC for n-phase PMSMs, encompassing models for both 3-phase and 5-phase PMSMs. It also introduced a general FOC strategy employing PI controllers, applicable to n-phase PMSMs. This strategy incorporated all odd harmonics of EMF components, along with the fundamental harmonic, to achieve enhanced torque. The chapter explored two PWM strategies for n-phase VSIs: CPWM and SVPWM. Each technique, CPWM and SVPWM, was examined for its specific advantages and disadvantages, detailing their implementation and characteristics. The simulation results presented in this chapter validated the effectiveness of FOC with 3-th harmonic current injection for 5-phase PMSMs. These results emphasized the significant improvement in torque response achieved by the proposed FOC strategy under maximum load torque conditions. Moreover, the outcomes highlighted CPWM with 5^{th} harmonic injection as a preferable PWM technique for n-phase PMSM applications, owing to its simplicity and superior performance. In conclusion, this chapter made a significant contribution to the understanding of the modeling, control, and performance aspects of PMSM system.

Chapter 3 focused on anti-disturbance sliding-mode control applied to PMSMs. The use of SOSMC was demonstrated as an effective strategy for reducing chattering and improving control performance under various disturbances. The results highlighted the superiority of SOSMC over conventional PI control and traditional sliding-mode control, setting the stage for further exploration in fault-tolerant control.

Chapter 4 extended the investigation to 3-phase PMSMs, addressing challenges associated with demagnetization and short-circuit faults. The combination of SOSMC with a FESO was proposed as a novel FTC strategy. The results demonstrated the efficiency and robust

dynamic performance of the combined approach in handling faults and external disturbances. The incorporation of an IT2FLC within the observer further enhanced the system's resilience.

Chapter 5 explored the FTC of 5-phase PMSMs in the presence of open-circuit faults. The introduced strategy, employing SMC with a NESO based on the hyperbolic tangent function, demonstrated its efficacy in mitigating the consequences of faults. A comparative analysis between the proposed control and traditional control methods underscored the superiority of the proposed approach, showcasing reduced torque ripples and improved robustness.

Collectively, the research presented in this thesis contributes valuable insights into the development and application of fault-tolerant control strategies for various types of electrical motor systems. The demonstrated approaches, ranging from anti-disturbance sliding-mode control to the integration of fuzzy logic and nonlinear observers, offer promising solutions for maintaining motor system performance in the presence of faults and disturbances. This work contributes to the advancement of control strategies in the realm of electric motor applications, addressing critical challenges and paving the way for more robust and reliable motor systems in practical industrial applications.

Bibliography

[1] Yongqing Wei, Mingzhong Qiao, and Peng Zhu. Fault-tolerant operation of five-phase permanent magnet synchronous motor with independent phase driving control. *CES Transactions on Electrical Machines and Systems*, 6(1):105–110, 2022.

[2] Defeng Wu, Yuxiang Liao, Chaodong Hu, Shuanghe Yu, and Qingyuan Tian. An enhanced fuzzy control strategy for low-level thrusters in marine dynamic positioning systems based on chaotic random distribution harmony search. *International Journal of Fuzzy Systems*, 23:1823–1839, 2021.

[3] Yang Yang, Qiang He, Chunyun Fu, Shuiping Liao, and Peng Tan. Efficiency improvement of permanent magnet synchronous motor for electric vehicles. *Energy*, 213:118859, 2020.

[4] Qi Huang, Qiuhong Huang, Hangcheng Guo, and Jichao Cao. Design and research of permanent magnet synchronous motor controller for electric vehicle. *Energy Science & Engineering*, 11(1):112–126, 2023.

[5] Zaiping Zheng, Qiqi Li, Xuyang Li, Ping Zheng, Kaichun Wang, and Peijuan Cui. Analysis and fault-tolerant control of inter-turn short-circuit fault for five-phase permanent-magnet synchronous machine. *Energy Reports*, 8:7360–7373, 2022.

[6] Xueqing Wang, Shaowei Ren, Dianxun Xiao, Xin Meng, Gaoliang Fang, and Zheng Wang. Fault-tolerant control of open-circuit faults in standard pmsm drives considering torque ripple and copper loss. *IEEE Transactions on Transportation Electrification*, pages 1–1, 2023.

[7] A. Khlaief, M. Boussak, and M. Gossa. Open phase faults detection in pmsm drives based on current signature analysis. In *The XIX International Conference on Electrical Machines - ICEM 2010*, pages 1–6, 2010.

[8] Andriy Sarabakha, Changhong Fu, Erdal Kayacan, and Tufan Kumbasar. Type-2 fuzzy logic controllers made even simpler: From design to deployment for uavs. *IEEE Transactions on Industrial Electronics*, 65(6):5069–5077, 2018.

[9] Behrooz Safarinejadian and Elham Kowsari. Fault detection in non-linear systems based on gp-ekf and gp-ukf algorithms. *Systems Science & Control Engineering*, 2(1):610–620, 2014.

[10] Claudio Bonivento, Alberto Isidori, Lorenzo Marconi, and Andrea Paoli. Implicit fault-tolerant control: application to induction motors. *Automatica*, 40(3):355–371, 2004.

[11] Mohamed El Hachemi Benbouzid, Demba Diallo, and Mounir Zeraoulia. Advanced fault-tolerant control of induction-motor drives for ev/hev traction applications: From conventional to modern and intelligent control techniques. *IEEE Transactions on Vehicular Technology*, 56(2):519–528, 2007.

[12] Mogens Blanke, Michel Kinnaert, Jan Lunze, Marcel Staroswiecki, and Jochen Schröder. *Diagnosis and fault-tolerant control*, volume 2. Springer, 2006.

[13] Youmin Zhang and Jin Jiang. Bibliographical review on reconfigurable fault-tolerant control systems. *Annual Reviews in Control*, 32(2):229–252, 2008.

[14] Halim Alwi, Christopher Edwards, and Chee Pin Tan. *Fault detection and fault-tolerant control using sliding modes*. Springer, 2011.

[15] Jin Jiang and Xiang Yu. Fault-tolerant control systems: A comparative study between active and passive approaches. *Annual Reviews in Control*, 36(1):60–72, 2012.

[16] Prashant Mhaskar, Jinfeng Liu, and Panagiotis D Christofides. *Fault-tolerant process control: methods and applications*. Springer Science & Business Media, 2012.

[17] Gouichiche Abdelmadjid, Boucherit Seghir Mohamed, Tadjine Mohamed, Safa Ahmed, and Messlem Youcef. An improved stator winding fault tolerance architecture for vector control of induction motor: Theory and experiment. *Electric Power Systems Research*, 104:129–137, 2013.

[18] Nadia Djeghali, Malek Ghanes, Said Djennoune, and Jean-Pierre Barbot. Sensorless fault tolerant control for induction motors. *International Journal of Control, Automation and Systems*, 11:563–576, 2013.

[19] Aziz Raisemche, Moussa Boukhnifer, Chérif Larouci, and Demba Diallo. Two active fault-tolerant control schemes of induction-motor drive in ev or hev. *IEEE Transactions on Vehicular Technology*, 63(1):19–29, 2013.

[20] Hemza Mekki, Omar Benzineb, Djamel Boukhetala, Mohamed Tadjine, and Mohamed Benbouzid. Sliding mode based fault detection, reconstruction and fault tolerant control scheme for motor systems. *ISA transactions*, 57:340–351, 2015.

[21] Huaming Qian, Yu Peng, and Guangyi Yang. Reduced-order observer-based fault estimation and fault-tolerant control for a class of discrete lipschitz nonlinear systems. *Optimal Control Applications and Methods*, 37(6):1236–1262, 2016.

[22] Jianglin Lan and Ron J Patton. A new strategy for integration of fault estimation within fault-tolerant control. *Automatica*, 69:48–59, 2016.

[23] Ron J. Patton. Fault-tolerant control: The 1997 situation. *IFAC Proceedings Volumes*, 30(18):1029–1051, 1997. IFAC Symposium on Fault Detection, Supervision and Safety for Technical Processes (SAFEPROCESS 97), Kingston upon Hull, UK, 26-28 August 1997.

[24] Afef Fekih. Fault tolerant control design for complex systems: Current advances and open research problems. In *2015 IEEE International Conference on Industrial Technology (ICIT)*, pages 1007–1012, 2015.

[25] Alireza Abbaspour, Sohrab Mokhtari, Arman Sargolzaei, and Kang K. Yen. A survey on active fault-tolerant control systems. *Electronics*, 9(9), 2020.

[26] Halim Alwi, Christopher Edwards, and Chee Pin Tan. *Fault Tolerant Control and Fault Detection and Isolation*, pages 7–27. Springer London, London, 2011.

[27] Thomas Moor. A discussion of fault-tolerant supervisory control in terms of formal languages. *Annual Reviews in Control*, 41:159–169, 2016.

[28] Xiang Yu and Jin Jiang. A survey of fault-tolerant controllers based on safety-related issues. *Annual Reviews in Control*, 39:46–57, 2015.

[29] Zhiwei Gao, Carlo Cecati, and Steven X. Ding. A survey of fault diagnosis and fault-tolerant techniques—part i: Fault diagnosis with model-based and signal-based approaches. *IEEE Transactions on Industrial Electronics*, 62(6):3757–3767, 2015.

[30] H. Alwi, C. Edwards, O. Stroosma, and J. A. Mulder. Fault tolerant sliding mode control design with piloted simulator evaluation. *Journal of Guidance, Control, and Dynamics*, 31(5):1186–1201, 2008.

[31] Qinglei HU, Youmin ZHANG, Xing HUO, and Bing XIAO. Adaptive integral-type sliding mode control for spacecraft attitude maneuvering under actuator stuck failures. *Chinese Journal of Aeronautics*, 24(1):32–45, 2011.

[32] Rongrong Wang and Junmin Wang. Passive actuator fault-tolerant control for a class of overactuated nonlinear systems and applications to electric vehicles. *IEEE Transactions on Vehicular Technology*, 62(3):972–985, 2013.

[33] Zhenyu Yang, Mogens Blanke, and Michel Verhaegen. Robust control mixer method for reconfigurable control design using model matching. *IET Control Theory & Applications*, 1(1):349–357, 2007.

[34] Hao Shen, Ju H Park, and Zheng-Guang Wu. Finite-time reliable l_2-l_∞/h_∞ control for takagi–sugeno fuzzy systems with actuator faults. *IET Control Theory & Applications*, 8(9):688–696, 2014.

[35] Hao Shen, Lei Su, and Ju H Park. Reliable mixed h_∞/passive control for t–s fuzzy delayed systems based on a semi-markov jump model approach. *Fuzzy Sets and Systems*, 314:79–98, 2017.

[36] M. Benosman and K.-Y. Lum. Passive actuators' fault-tolerant control for affine nonlinear systems. *IEEE Transactions on Control Systems Technology*, 18(1):152–163, 2010.

[37] Huai-Ning Wu. Reliable lq fuzzy control for continuous-time nonlinear systems with actuator faults. *IEEE Transactions on Systems, Man, and Cybernetics, Part B (Cybernetics)*, 34(4):1743–1752, 2004.

[38] Samir Zeghlache, Kamel Kara, and Djamel Saigaa. Fault tolerant control based on interval type-2 fuzzy sliding mode controller for coaxial trirotor aircraft. *ISA Transactions*, 59:215–231, 2015.

[39] Yu Luo, Andrea Serrani, Stephen Yurkovich, Michael W. Oppenheimer, and David B. Doman. Model-predictive dynamic control allocation scheme for reentry vehicles. *Journal of Guidance, Control, and Dynamics*, 30(1):100–113, 2007.

[40] Tor A. Johansen and Thor I. Fossen. Control allocation—a survey. *Automatica*, 49(5):1087–1103, 2013.

[41] Minh-Duc Hua, Guillaume Ducard, Tarek Hamel, Robert Mahony, and Konrad Rudin. Implementation of a nonlinear attitude estimator for aerial robotic vehicles. *IEEE Transactions on Control Systems Technology*, 22(1):201–213, 2014.

[42] Afef Fekih. Fault diagnosis and fault tolerant control design for aerospace systems: A bibliographical review. In *2014 American Control Conference*, pages 1286–1291, 2014.

[43] Tushar Jain, Joseph J Yamé, and Dominique Sauter. Active fault-tolerant control systems. *Cham, Switzerland: Springer*, 2018.

[44] Hongxu Zhang, Jun Hu, and Xiaoyang Yu. Adaptive sliding mode fault-tolerant control for a class of uncertain systems with probabilistic random delays. *IEEE Access*, 7:64234–64246, 2019.

[45] Bo-Chao Zheng, Xinghuo Yu, and Yanmei Xue. Quantized feedback sliding-mode control: An event-triggered approach. *Automatica*, 91:126–135, 2018.

[46] Biao Lu, Yongchun Fang, and Ning Sun. Continuous sliding mode control strategy for a class of nonlinear underactuated systems. *IEEE Transactions on Automatic Control*, 63(10):3471–3478, 2018.

[47] Durmuş Kaya, Fatma Çanka Kılıç, and Hasan Hüseyin Öztürk. Energy efficiency in pumps. In *Energy Management and Energy Efficiency in Industry*, pages 329–374. Springer, 2021.

[48] Olav Vaag Thorsen and Magnus Dalva. A survey of faults on induction motors in offshore oil industry, petrochemical industry, gas terminals, and oil refineries. *IEEE transactions on industry applications*, 31(5):1186–1196, 1995.

[49] Failure analysis of the deep groove ball bearings of an electric motor. *Engineering Failure Analysis*, 12(5):772–783, 2005. ICEFAI Part I.

[50] Pinjia Zhang, Bin Lu, and Thomas G. Habetler. Active stator winding thermal protection for ac motors. In *Conference Record of 2009 Annual Pulp and Paper Industry Technical Conference*, pages 11–19, 2009.

[51] Pan-Pan Wang, Xiao-Xiao Chen, Yong Zhang, Yong-Jun Hu, and Chang-Xin Miao. Ibpso-based music algorithm for broken rotor bars fault detection of induction motors. *Chinese Journal of Mechanical Engineering*, 31(1):1–10, 2018.

[52] J. Milimonfared, H.M. Kelk, S. Nandi, A.D. Minassians, and H.A. Toliyat. A novel approach for broken-rotor-bar detection in cage induction motors. *IEEE Transactions on Industry Applications*, 35(5):1000–1006, 1999.

[53] Castelli Marcelo, Juan Pablo Fossatti, and Jose Ignacio Terra. Fault diagnosis of induction motors based on fft. In Salih Mohammed Salih, editor, *Fourier Transform*, chapter 7. IntechOpen, Rijeka, 2012.

[54] M. Haji and H.A. Toliyat. Pattern recognition-a technique for induction machines rotor broken bar detection. *IEEE Transactions on Energy Conversion*, 16(4):312–317, 2001.

[55] Pinjia Zhang, Yi Du, Thomas G. Habetler, and Bin Lu. A survey of condition monitoring and protection methods for medium-voltage induction motors. *IEEE Transactions on Industry Applications*, 47(1):34–46, 2011.

[56] Randy R Schoen, Thomas G Habetler, Farrukh Kamran, and RG Bartfield. Motor bearing damage detection using stator current monitoring. *IEEE transactions on industry applications*, 31(6):1274–1279, 1995.

[57] Taner Goktas, Mohsen Zafarani, and Bilal Akin. Discernment of broken magnet and static eccentricity faults in permanent magnet synchronous motors. *IEEE Transactions on Energy Conversion*, 31(2):578–587, 2016.

[58] Marko Slunjski, Ornella Stiscia, Martin Jones, and Emil Levi. General torque enhancement approach for a nine-phase surface pmsm with built-in fault tolerance. *IEEE Transactions on Industrial Electronics*, 68(8):6412–6423, 2021.

[59] Emil Levi, Radu Bojoi, Francesco Profumo, HA Toliyat, and S Williamson. Multiphase induction motor drives–a technology status review. *IET Electric Power Applications*, 1(4):489–516, 2007.

[60] Sathishkumar Karupusamy, Mohammed Ahmed Mustafa, Bos Mathew Jos, Priyanka Dahiya, Ramakant Bhardwaj, Pratik Kanani, and Anil Kumar. Torque control-based induction motor speed control using anticipating power impulse technique. *The International Journal of Advanced Manufacturing Technology*, pages 1–9, 2023.

[61] L. Parsa and H.A. Toliyat. Five-phase permanent-magnet motor drives. *IEEE Transactions on Industry Applications*, 41(1):30–37, 2005.

[62] Yi Sui, Ping Zheng, Yuhui Fan, and Jie Zhao. Research on the vector control strategy of five-phase permanent-magnet synchronous machine based on third-harmonic current injection. In *2017 IEEE International Electric Machines and Drives Conference (IEMDC)*, pages 1–8, 2017.

[63] L. F. Zhang, K. Wang, H. Y. Sun, and S.S. Zhu. Multiphase pm machines with halbach array considering third harmonic flux density. *IEEE Transactions on Industrial Electronics*, 66(12):9184–9193, 2019.

[64] Z. Y. Gu, K. Wang, Z. Q. Zhu, Z. Z. Wu, C. Liu, and R. W. Cao. Torque improvement in five-phase unequal tooth spm machine by injecting third harmonic current. *IEEE Transactions on Vehicular Technology*, 67(1):206–215, 2018.

[65] K. Wang, Z. Y. Gu, C. Liu, and Z. Q. Zhu. Design and analysis of a five-phase spm machine considering third harmonic current injection. *IEEE Transactions on Energy Conversion*, 33(3):1108–1117, 2018.

[66] Zipan Nie, Matthias Preindl, and Nigel Schofield. Svm strategies for multiphase voltage source inverters. 2016.

[67] Xavier Kestelyn and Eric Semail. A vectorial approach for generation of optimal current references for multiphase permanent-magnet synchronous machines in real time. *IEEE Transactions on Industrial Electronics*, 58(11):5057–5065, 2011.

[68] M. Slunjski, M. Jones, and E. Levi. Control of a symmetrical nine-phase pmsm with highly non-sinusoidal back-electromotive force using third harmonic current injection. In *IECON 2019 - 45th Annual Conference of the IEEE Industrial Electronics Society*, volume 1, pages 969–974, 2019.

[69] Zhuo Liu, Azeddine Houari, Mohamed Machmoum, Mohamed-Fouad Benkhoris, and Tianhao Tang. An active ftc strategy using generalized proportional integral observers applied to five-phase pmsg based tidal current energy conversion systems. *Energies*, 13(24), 2020.

[70] Drazen Dujic, Martin Jones, and Emil Levi. Continuous carrier-based vs. space vector pwm for five-phase vsi. In *EUROCON 2007 - The International Conference on "Computer as a Tool"*, pages 1772–1779, 2007.

[71] Wei Xu, Abdul Khalique Junejo, Yi Liu, and Md. Rabiul Islam. Improved continuous fast terminal sliding mode control with extended state observer for speed regulation of pmsm drive system. *IEEE Transactions on Vehicular Technology*, 68(11):10465–10476, 2019.

[72] Huiming Wang, Shihua Li, Qixun Lan, Zhenhua Zhao, and Xingpeng Zhou. Continuous terminal sliding mode control with extended state observer for pmsm speed regulation system. *Transactions of the Institute of Measurement and Control*, 39(8):1195–1204, 2017.

[73] A finite control set model predictive direct speed controller for pmsm application with improved parameter robustness. *International Journal of Electrical Power & Energy Systems*, 143:108509, 2022.

[74] Ayyoub Zeghlache, Hemza Mekki, Ali Djerioui, Mohamed Fouad Benkhoris, and Khaled Benzaoui. Fault tolerant control of pmsm based on improved exponential eso. In *2022 International Conference of Advanced Technology in Electronic and Electrical Engineering (ICATEEE)*, pages 1–6, 2022.

[75] Ayyoub Zeghlache, Hemza Mekki, Ali Djerioui, and Mohamed Fouad Benkhoris. Active fault-tolerant control for surface permanent magnet synchronous motor under demagnetization fault. *Periodica Polytechnica Electrical Engineering and Computer Science*, 2023.

[76] Bo Xu, Lei Zhang, and Wei Ji. Improved non-singular fast terminal sliding mode control with disturbance observer for pmsm drives. *IEEE Transactions on Transportation Electrification*, 7(4):2753–2762, 2021.

[77] Yang Ge, Lihui Yang, and Xikui Ma. Adaptive sliding mode control based on a combined state/disturbance observer for the disturbance rejection control of pmsm. *Electrical engineering*, 102:1863–1879, 2020.

[78] Huan Zhang, Qunying Liu, Jiashu Zhang, Shuheng Chen, and Changhua Zhang. Speed regulation of permanent magnet synchronous motor using event triggered sliding mode control. *Mathematical Problems in Engineering*, 2018.

[79] Arie Levant. Sliding order and sliding accuracy in sliding mode control. *International journal of control*, 58(6):1247–1263, 1993.

[80] Muhammad Rafiq, Saeed ur Rehman, Fazal ur Rehman, Qarab Raza Butt, and Irfan Awan. A second order sliding mode control design of a switched reluctance motor using super twisting algorithm. *Simulation Modelling Practice and Theory*, 25:106–117, 2012.

[81] Jun Yang, Wen-Hua Chen, Shihua Li, Lei Guo, and Yunda Yan. Disturbance/uncertainty estimation and attenuation techniques in pmsm drives—a survey. *IEEE Transactions on Industrial Electronics*, 64(4):3273–3285, 2017.

[82] Z.Q. Zhu, S. Ruangsinchaiwanich, and D. Howe. Synthesis of cogging-torque waveform from analysis of a single stator slot. *IEEE Transactions on Industry Applications*, 42(3):650–657, 2006.

[83] P. Dziwniel, B. Boualem, F. Piriou, J.-P. Ducreux, and P. Thomas. Comparison between two approaches to model induction machines with skewed slots. *IEEE Transactions on Magnetics*, 36(4):1453–1457, 2000.

[84] Ching-Lon Huang, Feng-Chi Lee, Chia-Jung Liu, Jyun-You Chen, Yi-Jen Lin, and Shih-Chin Yang. Torque ripple reduction for bldc permanent magnet motor drive using dc-link voltage and current modulation. *IEEE Access*, 10:51272–51284, 2022.

[85] Fatih Adıgüzel and Türker Türker. A periodic adaptive controller for the torque loop of variable speed brushless dc motor drives with non-ideal back-electromotive force. *Automatika*, 63(4):732–744, 2022.

[86] Doo-Il Son, Jun-Seo Han, Je-Suk Park, Hee-Sun Lim, and Geun-Ho Lee. Performance improvement of dtc-svm of pmsm with compensation for the dead time effect and power switch loss based on extended kalman filter. *Electronics*, 12(4), 2023.

[87] Jie Shi and Shihua Li. Analysis and compensation control of dead-time effect on space vector pwm. *Journal of Power Electronics*, 15(2):431–442, 2015.

[88] Sang-Il Kim, Jeong-Yeon Kim, and Kwang-Woon Lee. Current measurement offset error compensation scheme considering saturation of current controller in spmsm drives. *IEEE Access*, 11:17233–17240, 2023.

[89] Weizhe Qian, S.K. Panda, and Jian-Xin Xu. Torque ripple minimization in pm synchronous motors using iterative learning control. *IEEE Transactions on Power Electronics*, 19(2):272–279, 2004.

[90] Shihua Li and Zhigang Liu. Adaptive speed control for permanent-magnet synchronous motor system with variations of load inertia. *IEEE Transactions on Industrial Electronics*, 56(8):3050–3059, 2009.

[91] Shihua Li and Hao Gu. Fuzzy adaptive internal model control schemes for pmsm speed-regulation system. *IEEE Transactions on Industrial Informatics*, 8(4):767–779, 2012.

[92] Andrej Kačenka, Adrian-Cornel Pop, Ioana Vintiloiu, and Daniel Fodorean. Lumped parameter thermal modeling of permanent magnet synchronous motor. In *2019 Electric Vehicles International Conference (EV)*, pages 1–6, 2019.

[93] Cong Bai, Zhonggang Yin, Yanqing Zhang, and Jing Liu. Robust predictive control for linear permanent magnet synchronous motor drives based on an augmented internal model disturbance observer. *IEEE Transactions on Industrial Electronics*, 69(10):9771–9782, 2022.

[94] Ziyang Liu, Guodong Feng, and Yu Han. Extended-kalman-filter-based magnet flux linkage and inductance estimation for pmsm considering magnetic saturation. In *2021 36th Youth Academic Annual Conference of Chinese Association of Automation (YAC)*, pages 430–435, 2021.

[95] Henrik Olsson, Karl Johan Åström, Carlos Canudas De Wit, Magnus Gäfvert, and Pablo Lischinsky. Friction models and friction compensation. *Eur. J. Control*, 4(3):176–195, 1998.

[96] Wenli Li, Yongkang Liu, Shuaishuai Ge, and Daming Liao. Research of mechanical resonance analysis and suppression control method of the servo drive system. *Shock and Vibration*, 2021:1–15, 2021.

[97] Anthony Simm, Qing Wang, Songling Huang, and Wei Zhao. Laser based measurement for the monitoring of shaft misalignment. *Measurement*, 87:104–116, 2016.

[98] V. Utkin. Variable structure systems with sliding modes. *IEEE Transactions on Automatic Control*, 22(2):212–222, 1977.

[99] JEAN-JACQUES E. SLOTINE. Sliding controller design for non-linear systems. *International Journal of Control*, 40(2):421–434, 1984.

[100] Weibing Gao and J.C. Hung. Variable structure control of nonlinear systems: a new approach. *IEEE Transactions on Industrial Electronics*, 40(1):45–55, 1993.

[101] Jaime A. Moreno and Marisol Osorio. A lyapunov approach to second-order sliding mode controllers and observers. In *2008 47th IEEE Conference on Decision and Control*, pages 2856–2861, 2008.

[102] Yong Chen, Siyuan Liang, Wanfu Li, Hong Liang, and Chengdong Wang. Faults and diagnosis methods of permanent magnet synchronous motors: A review. *Applied Sciences*, 9(10):2116, 2019.

[103] Jing Zhao, Xiaoqing Guan, Chenghai Li, Quansong Mou, and Zhen Chen. Comprehensive evaluation of inter-turn short circuit faults in pmsm used for electric vehicles. *IEEE Transactions on Intelligent Transportation Systems*, 22(1):611–621, 2021.

[104] Hyung-Jin Ahn and Dong-Myung Lee. A new bumpless rotor-flux position estimation scheme for vector-controlled washing machine. *IEEE Transactions on Industrial Informatics*, 12(2):466–473, 2016.

[105] Kaihui Zhao, Ruirui Zhou, Jinhua She, Changfan Zhang, Jing He, Gang Huang, and Xiangfei Li. Demagnetization-fault reconstruction and tolerant-control for pmsm using improved smo-based equivalent-input-disturbance approach. *IEEE/ASME Transactions on Mechatronics*, 27(2):701–712, 2022.

[106] Ayyoub Zeghlache, Hemza Mekki, Ali Djerioui, Mohamed Fouad Benkhoris, and Nassereddine Dahmane. Fault-tolerant control of pmsm based on second-order sliding mode. In *2022 IEEE International Conference on Electrical Sciences and Technologies in Maghreb (CISTEM)*, volume 4, pages 1–6, 2022.

[107] Hemza Mekki, Omar Benzineb, Djamel Boukhetala, Mohamed Tadjine, and Larbi Chrifi-Alaoui. Internal model based fault tolerant control strategy for pms motors. In *2014 Second World Conference on Complex Systems (WCCS)*, pages 311–316, 2014.

[108] H. Mekki, O. Benzineb, D. Boukhetala, M. Tadjine, and L. Chrifi-Alaoui. Fault tolerant control of pmsm drive using sliding mode strategy. In *2015 Intl Aegean Conference on Electrical Machines & Power Electronics (ACEMP), 2015 Intl Conference on Optimization of Electrical & Electronic Equipment (OPTIM) & 2015 Intl Symposium on Advanced Electromechanical Motion Systems (ELECTROMOTION)*, pages 576–581, 2015.

[109] H. Mekki, O. Benzineb, D. Boukhetala, L. Chrifi-Alaoui, and M. Tadjine. Fault tolerant design for permanent magnet synchronous motor using fuzzy speed controller. *IFAC-PapersOnLine*, 49(5):315–320, 2016. 4th IFAC Conference on Intelligent Control and Automation SciencesICONS 2016.

[110] J.A. Rosero, L. Romeral, J. Cusido, A. Garcia, and J.A. Ortega. On the short-circuiting fault detection in a pmsm by means of stator current transformations. In *2007 IEEE Power Electronics Specialists Conference*, pages 1936–1941, 2007.

[111] Claudio Bonivento, Alberto Isidori, Lorenzo Marconi, and Andrea Paoli. Implicit fault-tolerant control: application to induction motors. *Automatica*, 40(3):355–371, 2004.

[112] Big bang–big crunch optimization based interval type-2 fuzzy pid cascade controller design strategy. *Information Sciences*, 282:277–295, 2014.

[113] Leila Parsa and Hamid A. Toliyat. Fault-tolerant interior-permanent-magnet machines for hybrid electric vehicle applications. *IEEE Transactions on Vehicular Technology*, 56(4):1546–1552, 2007.

[114] Huang Qiu-Liang, Chen Yong, and Xu Li. Fault-tolerant control strategy for five-phase pmsm with third-harmonic current injection. *IEEE Access*, 6:58501–58509, 2018.

[115] Cong Xiong, Haiping Xu, Tao Guan, and Peng Zhou. Fault-tolerant foc for five-phase spmsm with non-sinusoidal back emf. *IET Electric Power Applications*, 13(11):1734–1742, 2019.

[116] Mahmoud F. Elmorshedy, Sivakumar Selvam, Sagar Bhaskar Mahajan, and Dhafer Almakhles. Investigation of high-gain two-tier converter with pi and super-twisting sliding mode control. *ISA Transactions*, 138:628–638, 2023.

[117] Bing Tian, Qun-Tao An, Jian-Dong Duan, Dong-Yang Sun, Li Sun, and Dmitry Semenov. Decoupled modeling and nonlinear speed control for five-phase pm motor under single-phase open fault. *IEEE Transactions on Power Electronics*, 32(7):5473–5486, 2017.

[118] Bing Tian, Galina Mirzaeva, Qun-Tao An, Li Sun, and Dmitry Semenov. Fault-tolerant control of a five-phase permanent magnet synchronous motor for industry applications. *IEEE Transactions on Industry Applications*, 54(4):3943–3952, 2018.

[119] Aimeng Wang and Shengjun Wei. Sliding mode control for permanent magnet synchronous motor drive based on an improved exponential reaching law. *IEEE Access*, 7:146866–146875, 2019.

[120] Sheng-Li Shi, Jian-Xiong Li, and Yi-Ming Fang. Extended-state-observer-based chattering free sliding mode control for nonlinear systems with mismatched disturbance. *IEEE Access*, 6:22952–22957, 2018.

[121] Bing Tian, Li Sun, Marta Molinas, and Qun-Tao An. Repetitive control based phase voltage modulation amendment for foc-based five-phase pmsms under single-phase open fault. *IEEE Transactions on Industrial Electronics*, 68(3):1949–1960, 2021.

Appendix A

PARAMETERS

Table A.1: Parameters of the SPMSM drive.

Parameter	**Value**
Rated output power (P_{rated})	4.4 kW
Rated speed (n_{rated})	1500 rpm
Rated torque (T_{rated})	28.4 Nm
Rated current (I_{rated})	16.5 A
Rated voltage (V_{rated})	400 V
Pole pairs (n_p)	4
Stator resistance (R_s)	0.25 Ohm
Stator inductance (L_s)	4.8 mH
PM flux-linkage (ϕ_f)	0.32 Wb
Inertia constant (J)	0.00774 Kg $\times$ m^2
Viscous friction (f)	0.0089 Kg $\times$ m^2/s
Switching frequency	10 kHz

Table A.2: Parameters of the controllers and observers.

Speed	q-axis current	d-axis current
$k_{1\Omega} = 80$	$k_{1q} = 100$	$k_{1d} = 100$
$k_{2\Omega} = 600$	$k_{2q} = 600$	$k_{2d} = 600$
$h_{\Omega 1} = 500$	$h_{q1} = 800$	$h_{d1} = 1000$
$h_{\Omega 2} = 90000$	$h_{q2} = 640000$	$h_{d2} = 500000$
$K_e = 1/11$	$K_e = 1/95$	$K_e = 1/13$
$K_{p\Omega} = 11$	$K_{pq} = 95$	$K_{pd} = 13$
$K_{i\Omega} = 9$	$K_{iq} = 85$	$K_{id} = 8$
$K_{d\Omega} = 6$	$K_{dq} = 70$	$K_{dd} = 9$
$\alpha_p = 0.62$	$\alpha_p = 0.5$	$\alpha_p = 0.25$
$\alpha_i = 0.075$	$\alpha_i = 0.9$	$\alpha_i = 0.5$
$\alpha_d = 0.62$	$\alpha_d = 0.5$	$\alpha_d = 0.5$

Table A.3: FPPMSM drive parameters.

Parameter	**Value**
n_p	2
R_s	1.1Ω
L_{dp}	$6.54mH$
L_{qp}	$8.32mH$
L_{ds}	$1.78mH$
L_{qs}	$1.68mH$
L_{ls}	$1.35mH$
ϕ_{f1}	$0.512Wb$
ϕ_{f3}	$0.034Wb$
J	$0.095Kg.m^2$
DC-link voltage	$150v$
Switching frequency	$10kHz$

Table A.4: MTO and MCL Comparison.

Control Type	**Control Criteria**	**Torque Ripples %**	**Speed Fluctuation %**
PI	MTO	37.3153	1.9202
	MCL	30.8831	1.5769
TSMC	MTO	19.4586	0.9958
	MCL	16.0544	0.814
SMC+NESO	MTO	1.9396	0.0118
	MCL	1.8087	0.0094